

https://dspace.org/

Characterization of a TW R260-60E1 Pearlite Rail Steel with a Weld Gap Size of 40 mm and 50 mm

Meyiwa, Lindani

2024
University of the Witwatersrand, Johannesburg
https://hdl.handle.net/10539/45386
Meyiwa, Lindani . (2024). Characterization of a TW R260-60E1 Pearlite Rail Steel with a Weld Gap Size of 40 mm and 50 mm [Masters dissertation, University of the Witwatersrand, Johannesburg]. WIReDSpace. https://hdl.handle.net/10539/45386

Downloaded from a DSpace repository. https://dspace.org/



UNIVERSITY OF THE
WITWATERSRAND,
JOHANNESBURG

Characterization of a TW R260-60E1 Pearlite Rail Steel with a Weld Gap Size of 40 mm and 50 mm.

MSc RESEARCH DISSERTATION

Prepared by

Lindani Meyiwa

Student number: 668760

Submitted to

School of Chemical and Metallurgical Engineering, Faculty of Engineering and the Built Environment, University of the Witwatersrand, Johannesburg, South Africa

OCTOBER 2024

DECLARATION

I declare that this dissertation is my own work. It is being submitted for the Degree of Master of Science in engineering to the University of the Witwatersrand, Johannesburg. It has not been submitted before for any degree or examination to any other University.



Signature

Date: 24 October 2024

ABSTRACT

The continuous weld rails (CWR) tracks that are joined by thermite welding (TW) method are known to experience weld failures during their service life. In avoiding or mitigating these failures, a weld gap in joining two rail ends was introduced. The purpose of the weld gap was to accommodate rail expansion during elevated temperatures. Traditionally, a weld gap of 24 mm was created between two rail ends. However, these weld joints were observed to be experiencing challenges of not being able to withstand high contact loads during service life, leading to plastic deformation and eventual failures. This study was investigating the effect on microstructural characteristics, heat-affected zone (HAZ) dimensions, mechanical properties attributes, and wear resistance behaviour of TW R260-60E1 pearlitic rail steel when the weld gap was set to 40 mm and 50 mm. The results revealed that the TW R260-60E1 pearlitic rail microstructure had no martensitic, bainitic and intergranular Widmanstätten ferritic structures. Pearlitic grain sizes and interlamellar spacing on the weld zone of the web region were measured to be 3.6 % wider on the sample with 40 mm weld gap compared to those on the sample with 50 mm weld gap. Big surface area to volume ratio and fast cooling rate had an influence on the production of finer pearlite grain sizes and interlamellar spacing within the web region for both samples. The results further showed that the HAZ width was one of the attributors to the improvement on the mechanical and wear resistance properties. HAZ width varied from 29 mm – 35 mm for sample with 40 mm weld gap, and 27 mm – 33 mm for sample with 50 mm weld gap. The HAZ width on the sample with 50 mm weld gap was narrow than the HAZ width on the sample with 40 mm weld gap. Narrow HAZ width improves microstructural characteristics, mechanical properties and wear resistance behaviour compared to the wider HAZ width. The improvement on the microstructure characterisation, mechanical properties and wear resistance behaviour are expected to extend the service life of the rail and facilitate superior rail expansion capabilities. This, in turn, is projected to diminish the probabilitiy of rail-related incidents and mitigate the risks of human fatilies associated with rail transportation.

Key words: weld gap, thermite welding, pearlitic rail steel, cooling rate, surface area to volume ratio, HAZ width, pearlite grain size.

COPYRIGHT

The copyright of this thesis vest in the University of the Witwatersrand, Johannesburg, South Africa, in accordance with the University`s Intellectual Property Policy.

No portion of the text may be reproduced, stored in a retrieval system, or transmitted in any form or by any means, including analogue and digital media, without prior in written permission from the University. Extracts of or quotations from this thesis may, however, be made in terms of sections 12 and 13 of the South African Copyright Act No.98 of 1978 (as amended), for non-commercial or educational purposes. Full acknowledgement must be made to the author and the University.

An electronic version of this thesis is available in the library webpage (www.wits.ac.za/library) under “Research Resources”.

For permission requests, please contact University Legal Office or the University Research Office (www.wits.ac.za)

ACKNOWLEDGEMENTS

I owe a debt of gratitude to my supervisor, Professor Nthabiseng Maledi for her guidance and support throughout my research studies. I am extremely appreciative for her assistance and for creating a productive and enjoyable environment for my research.

I am grateful to Transnet SOC LTD, freight rail division, for giving me an opportunity to work on this project and for providing welded rail samples, and performing NDT test (X-rays). Thanks to Petra Dinham for SEM characterisation work, and for constantly motivating me to pursue my research work.

Many thanks to the workshop team at the University of the Witwatersrand School of Chemical and Metallurgical Engineering for assisting with sample preparations, and to Mr Donald Mahole for helping me with wear tests.

I am eternally grateful to my co-workers for always being there for me and providing constant motivation when I was ready to give up. Many thanks to Sibusiso Moloi, Reggie Mfono, Tshepho Thage, William Mlambo, Thendo Mphaphathi, and Tebogo Molokwane for sharing your insights and the contributions that enabled me to complete this project.

Most importantly, I would like to express my gratitude to my family for always believing in me, to my girlfriend for her unwavering support, to my sister Thabile Bhengu for supporting me, and finally, to my good friend S'Bongiseni Zulu who was always there to motivate me, and to all my friends who made sure that I finished what I started.

TABLE OF CONTENTS

DECLARATION i
ABSTRACT ii
COPYRIGHT iii
ACKNOWLEDGEMENTS iv
TABLE OF CONTENTS v
LIST OF TABLES viii
LIST OF FIGURES ix
LIST OF EQUATIONS xii
LIST OF ABBREVIATIONS xiii
1. CHAPTER 1 1
1.1 Introduction 1
1.2 Research Questions 3
1.3 Research Problem Statement 3
1.4 Hypothesis 4
1.5 Research Aims and Objectives 4
1.6 Significance of the Research 4
1.7 Description of the Dissertation 5
2. CHAPTER 2 6
2.1 Background and literature review 6
2.1.1 Railway rail in South Africa 6
2.1.2 Rails profiles and grades 6
2.1.3 Rail steel materials 9
2.1.4 Pearlitic microstructure formation 13
2.1.4.1 Microstructure and mechanical properties of the pearlitic steel 15
2.1.5 Joining of rail ends into tracks 18
2.1.5.1 Bolted tracks. 18
2.1.5.2 Continuous welded rail tracks 20
2.1.6 Thermite welding 21
2.1.6.1 Thermite welding process 21
2.1.6.1.1 The effect of TW on the microstructure characterisation and mechanical properties. 25

2.1.6.1.2 Effects of weld gap on the microstructure characterisation and mechanical properties 32
2.1.7 Rail steels and rail welds failures....34
2.2 Chapter summary....36
3. CHAPTER 3....38
3.1 Experimental work....38
3.1.1 Introduction....38
3.1.2 Materials....38
3.1.3 Thermite welding of rail steel....39
3.1.4 Non-Destructive Testing....40
3.1.5 Sectioning of the thermite welded rails....41
3.1.6 Metallographic examination....41
3.1.6.1 Microstructure characterisation....41
3.1.6.1.1 Microstructural analysis....42
3.1.6.1.2 Phase identification....42
3.1.7 Measuring of Heat Affected Zone Width....43
3.1.8 Hardness testing....43
3.1.9 Mechanical testing....44
3.1.9.1 Tensile test....44
3.1.9.2 Charpy Impact testing....44
3.1.10 Wear testing....45
3.11 Chapter Summary....46
4. CHAPTER 4....47
4.1 Results and discussion....47
4.1.1 Introduction....47
4.1.2 Non-destructive testing....47
4.1.2.1 Visual examination....48
4.1.2.2 X-ray technique (Radiography)....49
4.1.3 HAZ width measurements....50
4.1.4 Microstructure characterisation....54
4.1.4.1 Optical microscope and scanning electron microscope.....54

4.1.4.2 X-Ray diffraction 65
4.1.5 Hardness distribution 66
4.1.6 Mechanical properties 70
4.1.6.1 Tensile testing 71
4.1.6.2 Charpy Impact testing 77
4.1.7 Wear testing 80
4.2 Chapter Summary 85
5. CHAPTER 5 87
5.1 Conclusion and Recommendations 87
5.1.1 Conclusion 87
5.1.2 Recommendations for further work 88
6. REFERENCES 89

LIST OF TABLES

Table 2-1: Dimensions o-f R260 – 60E1 rail according to EN 13674 - 1 standard. 8

Table 2-2: Dimensions of R260 – 60E1 rail regions according to EN 13674 - 1 standard. 8

Table 2-3: Surface area – Volume ratio (SA: V) of the 60E1 - R260 regions (Liberty OneSteel, 2017). 8

Table 2-4: The required tensile properties for standard and high strength rails (Meade 1999). 9

Table 2-5: Three grades of rails introduced by Corus Rail products (2008) (UIC860: 2008). 11

Table 2-6: Three grades of rail steels introduced by institute of Rail Welding (EN13674-1:2018). 11

Table 2-7: Changes in yield and tensile strength with the variations of interlamellar spacings and cooling rates of a pearlitic rail steel (Gomes et al. 1997). 13

Table 2-8: Composition and tensile properties of a rail and two standard thermite welds (Myers et al.,1982). 24

Table 2-9: Preheating process and aluminothermic welding features (Garcia et al. 2017). 33

Table 2-10: Preheating process and times (Garcia et al. 2017). 33

Table 3-1: Chemical composition (%) for pearlitic rail steels and thermite weld. 39

Table 3-2: Oxy propane preheating conditions used for the thermite welded rail samples. 40

Table 3-3: Rail samples dimensions for tensile testing. 44

Table 3-4: Abrasive wear testing parameters. 45

Table 4-1: Measured grain sizes of pearlite structure for samples with weld gap of 40 mm and 50 mm. 63

Table 4-2: Summary of hardness distribution values for the TW R260-60E1 rail weld on the 40 and 50 mm weld gap samples. 67

Table 4-3: Tensile test results of a TW R260-60E1 rail steels. 73

Table 4-4: Impact test results of a TW R260-60E1 rail steel samples with a 50mm weld gap. 77

Table 4-5: Specific wear rate on a sliding speed of 0.025m/s. 81

LIST OF FIGURES

Figure 2-1: Flat bottom rail profiles (EN 13674-1: 2017). 7

Figure 2-2: Phase diagram of iron-carbon (SubsTech 2012). 13

Figure 2-3: Schematic illustration of the formation of pearlite from γ: (a) Nucleation of an Fe_3C crystal at the interface of two γ grains, γ1 and γ2, establishing a semi-coherent interface with γ1 and an incoherent interface with γ2. (b) Growth of the Fe_3C grain into γ2. (c) Nucleation of α at the γ1/ γ2 interface in the C depleted γ matrix of γ2 adjacent to the Fe_3C grain. (d) Branching of Fe_3C lamella (Mittemeijer 2010). 14

Figure 2-4: Schematic of the rail thermite welding process (Altintas 2013). 23

Figure 2-5: Cooling curve for different points in rail cross section and CCT diagram for R260 steel (constructed by JMatPro)..... 25

Figure 2-6: Microstructures of standard thermite welds show (a) intragranular Widmanstätten ferrite with small, isolated grains of pearlite, and (b) pearlite and pro-eutectoid ferrite (Myers et al. 1982). 26

Figure 2-7: Microstructure of a standard thermite weld metal shows pearlite and pro-eutectoid ferrite at prior austenite grain boundaries at higher magnification (SEM) (Ilic et al. 1999). ..26

Figure 2-8: Schematic microstructure of the weldmented zone showing the correlation between changes in grain size within welded zone and the iron – carbon binary diagram along the rail after the changes TW process with their corresponding phases (SubsTech, 2012). 27

Figure 2-9: Etched and photographed macrostructure of a standard thermite weld rail with 24 mm weld gap, showing columnar grains (weld and HAZ widths are 40-50 and 15-25 mm respectively) (Webster et al. 1997). 30

Figure 3-1: Flow chart illustrating the experimental methodology that was followed to achieve the research objective..... 38

Figure 3-2: Schematic illustration of Vickers hardness test (Struers Ensuring Certainty, 2015). 43

Figure 4-1: Thermite welded rail with a 40mm weld gap. 48

Figure 4-2: Thermite welded rail with a 50mm weld gap. 48

Figure 4-3: X-ray images showing head-foot region of a thermite welded rail with a weld gap of (a) 40mm and (b) 50 mm. 49

Figure 4-4: X-ray images showing the web region of a thermite welded rail with a weld gap: (a) 40 mm and (b) 50 mm. 49

Figure 4-5: Macrograph of the ground, mechanically polished and 5% nital etched sample, extracted from the longitudinal section of the thermite welded rail. This sampling represents both the 40mm and 50mm weld gap samples. 50

Figure 4-6: Macrograph of the ground, mechanically polished and etched with 5% nital. The sample is extracted from the longitudinal section of the thermite welded rail with a 40 mm weld gap. 51

Figure 4-7: HAZ width measurements for the head, web, and foot region along the rail height of the thermite welded rail for the 40- and 50-mm weld gaps. 52

Figure 4-8: Microstructure of the R260-60E1 parent rail steel showing the pearlitic structure [Etched in 5% nital, 500x magnification]. 54

Figure 4-9: SEM image of a R260-60E1 parent rail steel showing pearlite structures at higher 5000x magnification. 55

Figure 4-10: Microstructure of a TW R260-60E1 pearlitic rail steel taken on the weld centre. [Etched in 5% nital, 500x magnification]. 56

Figure 4-11: SEM image of a TW R260-60E1 pearlitic rail steel taken at the weld centre of a sample with a 50 mm weld gap using high magnification [5000x magnification]. Similar SEM image was obtained on the sample with a 40 mm weld gap. 57

Figure 4-12: Microstructure of the TW R260-60E1 taken on the regions of the weld zone for weld gap of 40mm and 50mm: (a) 40mm-head region, (b) 40mm-web region, (c) 40mm-foot region, (d) 50mm-head region, (e) 50mm-web region, and (f) 50mm-foot region. [Etched in 5%, 500x magnification]. 59

Figure 4-13: SEM image of a TW R260-60E1 pearlitic rail steel taken at the weld zone of a sample with a 50 mm weld gap using high magnification [5000x magnification]. Similar SEM image was obtained on the sample with a 40 mm weld gap. 60

Figure 4-14: Microstructure variation across the TW R260-60E1 rail at the head and web region for weld gap of 40mm; (1) Head region: (a) CGHAZ, (b) FGHAZ, (c) ICHAZ (2) Web region: (d) CGHA (e) FGHAZ, (d) ICHAZ [Etched in 5% nital, 500x magnification]. 61

Figure 4-15: Microstructure variation across the TW R260-60E1 rail at the head and web region for weld gap of 50mm; (1) Head region: (a) CGHAZ, (b) FGHAZ, (c) ICHAZ (2) Web region: (d) CGHAZ, (e) FGHAZ, (d) ICHAZ [Etched in 5% nital, 500x magnification]. 62

Figure 4-16: SEM image of a TW R260-60E1 rail steel showing pearlite structures at higher magnification for the (a) CGHAZ, (b) FGHAZ [5000x magnification]. 62

Figure 4-17: Measured grain sizes of pearlite structure for sample with weld gap of 40 mm and 50 mm. 63

Figure 4-18: SEM image of a TW R260-60E1 rail steel showing pearlite structures at higher magnification for the ICHAZ [5000x magnification]. 64

Figure 4-19: X - -Ray diffraction patterns for TW R260-60E1 rail sample with a weld gap of 50 mm. 65

Figure 4-20: Hardness distribution across the TW R260-60E1 grade rail steel of 40mm weld gap sample indented from the weld centreline to the parent rail of the head, web, and foot region. 66

Figure 4-21: Hardness distribution across the TW R260-60E1 grade rail steel of 50mm weld gap sample indented from the weld centreline to the parent rail of the head, web, and foot region. 67

Figure 4-22: Mechanical tensile stress vs tensile stain curve typical of high strength and high ductile material of a head - parent rail sample with a weld gap of 50 mm. 71

Figure 4-23: Mechanical tensile stress vs tensile stain curve typical of high strength and high ductile material of a head - HAZ sample with a weld gap of 50 mm. 72

Figure 4-24: Mechanical tensile stress vs tensile stain curve typical of high strength and high ductile material of a web - HAZ sample with a weld gap of 50 mm. 72

Figure 4-25: UTS results for TW R260-60E1 rails at room temperature. 73

Figure 4-26: Photo showing the sample that was tensile tested on the HAZ of the web region. 74

Figure 4-27: Photo showing the sample that was tensile tested on the weld of the web region. 74

Figure 4-28: Photo showing the sample that was tensile tested on the parent of the head region. 75

Figure 4-29: Photo showing the sample that was tensile tested on the weld of the head region. 75

Figure 4-30: Fracture surface stereo image of the sample that was tensile tested on the HAZ of the web region. The fracture surface showed partial brittle with a flat appearance. Similar images were observed on the other samples. 76

Figure 4-31: Impact Energy for TW R260-60E1 rails at room temperature. 78

Figure 4-32: Fracture surface stereo image of the impact toughness testing samples showing a flat and shiny appearance, which indicate a brittle fracture mode. 80

Figure 4-33: Specific wear rate of R260 rail steel samples. 81

Figure 4-34: COF vs sliding distance plot of the R260 rail samples. 82

Figure 4-35: Specific wear rate vs average hardness of the R260 rail samples. 82

Figure 4-36: COF vs Average hardness (HV_{10}) plot for R260 rail samples. 83

LIST OF EQUATIONS

Equation 2-1: Yield strength 16
Equation 2-2: Thermite welding reaction 1 22
Equation 2-3: Thermite welding reaction 2 22
Equation 2-4: Thermite welding reaction 3 22
Equation 3-1: Hardness calculation 43
Equation 3-2: Archard equation 45

LIST OF ABBREVIATIONS

Abbreviation	Meaning
µm	Micrometer
ASTM	American society for testing and material
BCC	Body centred cubic
C	Carbon
CE	Carbon equivalent
CGR	Cape Town government railways
CGHAZ	Coarse grain heat affected zone
COF	Coefficient of friction
Cr	Chromium
Cu	Copper
CWR	Continuous welded rail
EDM	Electro discharge machine
FAST	Facility for accelerated service testing
Fe	Iron
FGHAZ	Fine grain heat affected zone
g/cm^3	Grams per cubic meters
GPW	Gas pressure welding
HAZ	Heat affected zone
HB	Brinell hardness
HV	Vickers hardness
ICHAZ	Inter-critical heat affected zone
KPa	Kilopascal
Ltd	Limited liability company
Min	Minutes
mm	Millimetres
Mn	Manganese
Mo	Molybdenum
MPa	Megapascal
NDT	Non-destructive testing
Ni	Nickel

nm	Nanometers
OM	Optical microscope
P	Phosphorus
PRASA	Passenger rail agency of South Africa
RCF	Rolling contact fatigue
S	Sulphur
SA	South Africa
SEM	Scanning electron microscope
Si	Silicon
SOC	State owned corporation
TW	Thermite welding
UIC	Unit identification code
UK	United Kingdom
UTS	Ultimate tensile strength
V	Vanadium
Wt%	Weight percentage
XRD	X-Ray diffraction

1. CHAPTER 1

1.1 Introduction

Transnet SOC Ltd is the backbone of South Africa`s railway industry, which owns the continent's largest rail network (Transnet, 2017). Transnet is recognized as a world-class heavy haul freight rail company that specialises in the rail transportation through their operating division (OD) (Transnet, 2017). There are 6 core divisions within Transnet operating division, namely; Transnet freight rail (TFR), Transnet national port authority (TNPA), Transnet port terminal (TPT), Transnet engineering (TE), Transnet pipelines (TPL), and Transnet property (TP) (Transnet, 2017).

Transnet freight rail (TFR) is the largest operating division which is recognised as the world class heavy haul freight that specialises in the transportation of commodities for the export, regional and domestic markets (Our Divisions Transnet Freight Rail, 2021). The division utilizies and maintains approximately 31 00 km track of rail route, over which coal and iron ore are transported (Our Divisions Transnet Freight Rail, 2021).

The railway tracks that TFR utilizes are made of grade R260 conventional pearlitic structure rail steels (Transnet Rail Network – Technical, 2021). These rail steels are joined together by continuous welded rail (CWR) (Transnet Rail Network – Technical, 2021). The CWR is the method used to join two rail ends since the discountinuation of the bolted tracks (Transnet Rail Network – Technical, 2021).

Thermite welding (TW) and flash butt welding (FBW) are the most commonly used CWR methods at TFR and other railway industries worldwide (Skyttebol et al., 2005). Flash butt is a welding method which is commonly performed in stationery plants (Wang *et al.,* 2012). This welding process uses electrical induction as a heating method for rails and hydraulic forging of the heated rails to form a high performance joints (Wang *et al.,* 2012). Whereas, thermite welding method is an on-field welding process used to permanently join two rail ends by using silica sand mould (Yang et al,. 2018). In this process, an exothermic reaction between active iron oxides and a highly reactive aluminium produce molten metal (Yang et al,. 2018).

Thermite welding is the most preferred joining process over FBW because it is an on-site welding method, there are low welding costs associated with TW, electrical power is not required, and the process is efficient for both short term and long term maintenance intervention when compared to FBW (Yang et al., 2018). The welds that are produced by TW are found to

be prone to the formation of detrimental defects which includes but not limited to; shrinkage cavities, gas pockets, lack of fusion, hot tears and inclusions (Mutton and Alvarez, 2004, Skyttebol et al., 2005, and Chen et al., 2006).

Myers et al. (1982) investigated the structure and properties of thermite welds in rails. The study found that the variation in microstructure and mechanical properties led to poor ductility and impact toughness, which subsequently lead to weld failures. The study reported that rail thermite weld defects can be considered to be a contributing reason for poor ductility and impact toughness of thermite rail welds.

A welding gap was introduced when rails were joined using TW method to minimise weld failures due to the heterogenous microstructural and mechanical properties. The welding gap was further incorporated to accommodate rail expansion, particularly in response to elevated temperatures, which typically occurs when the rail is exposed to hot weather conditions (Webster et al., 1997).

Traditionally, a weld gap of 24 mm was created between two rail ends that were joined together using TW method (Webster et al., 1997). These welds were found to be experiencing plastic deformation and gradual failures (O`brisen, 2014), experiencing high rolling contact loads after being in service for a long time (O`brisen, 2014).

Mohassel et al. (2011) studied the mechanical and metallurgical properties of the wide gap of aluminothermic rail welds. The study reported that the yield and tensile strength of a wide weld gap of 50 mm was 98% and 95% of the parent rail, respectively, whereas the yield and tensile strength of a narrow gap weld (25mm) were about 99% and 88% of the parent rail respectively. According to these findings, the tensile strength properties of the wide weld gap was significantly higher than the narrow weld gap.

The primary objective of this research was to investigate the effect of increasing weld gap on the microstructural characteristics, heat-affected zone (HAZ) dimensions, mechanical properties, and wear behavior of TW R260-60E1 pearlitic rail steel.

A weld gap of 40 mm and 50 mm were used in this study to investigate the variation in the microstructure characterisation, mechanical properties and wear resistance behaviour. Microstructure characterisation included microstructural profile, encompassing grain morphology, phase distribution, and interstitial features. Mechanical properties, included hardness distribution profile, tensile strength, and impact toughness.

1.2 Research Questions

The key research questions addressed in this investigation study were as follows:

1. What effect does the weld gap of 40 mm and 50 mm have on the HAZ width distribution profile?

2. How does a weld gap of 40 mm and 50 mm affect the microstructure of the weld and HAZ?

3. How does the weld gap of 40 mm and 50 mm influence mechanical properties (i.e.hardness, tensile strength, and impact resistance) and wear resistance behaviour of the TW R260-60E1 pearlitic rail?

1.3 Research Problem Statement

The welding gap between two rail ends is one of the variables that influences the microstructure characterisation, mechanical properties and wear resistance behaviour of the rail thermite welds. The welding gap was intentionally incorporated to accommodate rail expansion, particularly in response to elevated temperatures, which typically occured when the rail was exposed to hot weather conditions (Webster et al., 1997). The presence of the welding gap between two rail ends reduced the risk of rail weld failures during services (O`Brisen, 2014).

Traditionally, a weld gap of 24 mm was created between two rail ends that were joined through the TW method (Webster et al, 1997). These welds were observed to experience challenges of high stress concentrations and were unable to withstand high rolling contact loads during service life, leading to plastic deformation and eventual weld failures (O`brisen, 2014).

The failure resilience of railway steels under high rolling contact loads during service life was compromised by various detrimental defects such as shatter cracks, shelling, detailed fracture, and wear (O`brisen, 2014). These defects posed serious threats to structural integrity and require careful consideration in material selection, design, and maintenance (O`brisen, 2014).

The purpose of this research project was to assess the effect of the microstructural characterisation, heat-affected zone (HAZ) dimensions, mechanical properties, and wear resistance behaviour of TW R260-60E1 pearlitic rail steel when the weld gap is set to be 40 mm and 50 mm.

1.4 Hypothesis

It is known that the weld gap has an influence in the microstructure characterisation, mechanical properties and wear resistance behaviour of the rail thermite welds. Increasing the weld gap of TW R260-60E1 pearlitic rail steel to 40 mm and 50 mm will result in an improvement in microstructural, mechanical and wear properties of rail thermite welds.

1.5 Research Aims and Objectives

The aim of this study was to determine the effect the weld gap set at 40 mm and 50 mm on the microstructure, mechanical and wear properties of the TWR260-60E1 rail steel.

The research aim was achieved by assessing the following objectives:

- Analyse the effect on HAZ width distribution profile when the weld gap of TW R260-60E1 pearlitic rail steel is set to be 40 mm and 50 mm.
- Evaluate the microstructure of the TW R260-60E1 pearlitic rail steel with a weld gap of 40 mm and 50 mm.
- Study the mechanical properties (hardness, tensile strength and impact resistance) when the weld gap on the TW R260-60E1 pearlitic rail steel is set to be 40 mm and 50 mm.
- Determine the wear resistance properties of the 40 mm and 50 mm weld gap joint of TW R260-60E1 pearlitic rail.

1.6 Significance of the Research

The significance of this research lies in its pivotal role in enhancing the reliability of TW R260-60E1 pearlitic rail steel, thereby addressing critical safety concerns and operational efficiency within the railway infrastructure. By meticulously investigating the effects of weld gap variations on the microstructure, mechanical properties, and wear resistance of this rail steel grade, the study aims to develop optimized welding parameters that mitigate the risks associated with rail expansion.

This optimization will not only diminishes the likelihood of train accidents stemming from rail deformation but also reduces the potential for human fatalities resulting from derailments or structural failures. Furthermore, the anticipated extension of rail lifespan resulting from improved welding practices promises significant economic benefits by minimizing maintenance costs and downtime associated with premature rail replacement.

Ultimately, the outcomes of this research endeavor are poised to contribute substantially to the safety, reliability, and longevity of railway systems, thereby fostering enhanced transportation sustainability and societal well-being.

1.7 Description of the Dissertation

The description of this dissertation is outlined in the following manner:

Chapter One of this dissertation includes the background of the research study, research questions, problem statement, hypothesis, aim and objectives, significance of the research, and the description of the dissertation.

Chapter Two details the literature review on the history of railway rails. It also examines different rail profiles and grades commonly used, the formation of pearlitic structure and the role of cooling rate in order to produce pearlitic steel, the transition of joining rail tracks from the use of bolts to the currently used continuous welded rail (CWR) tracks, and lastly, the review addresses previous studies that focused on the effect of the weld gap on the microstructure, mechanical properties, and wear resistance for TW rail steel.

Chapter Three describes the experimental procedure that was followed to achieve the objectives of this research study. This includes thermite welding method on rail steels, non-destructive testing to assess the weld quality on both surface and the sub surface, metallographic examination, mechanical (tensile and Charpy test) and wear testing.

Chapter Four presents the results and discussion of all the tests and analysis that were carried out in this research study for the characterisation of the TW R260-60E1 pearlitic rail steel when the weld gap is set to 40 mm and 50 mm.

Chapter Five and Six Focuses on the conclusion and recommendations derived from the findings of this study respectively.

2. CHAPTER 2

2.1 Background and literature review

2.1.1 Railway rail in South Africa

South Africa`s railway lines are mostly controlled by two government entities namely, Passenger Rail Agency of South Africa (PRASA) and Transnet company. PRASA is responsible for transporting commuters across the country. Whereas, Transnet company through transnet operation division (OD) is responsible for transporting of heavy loads and goods to different part of the country (Transnet, 2017).

Transnet operating division is divided into 6 core divisions, those core divisions are; Transnet freight rail (TFR), Transnet national port authority (TNPA), Transnet port terminal (TPT), Transnet engineering (TE), Transnet pipelines (TPL), and Transnet property (TP) (Transnet, 2017).

Transnet freight rail (TFR) is the largest operating division which is recognised as the world class heavy haul freight that specialises in the transportation of commodities for exports, and regional and domestic markets (Our Divisions Transnet Freight Rail, 2021). The division utilisies and maintains approximately 31 00 km track of rail route, over which commodities (coal, and iron ore) are transported (Our Divisions Transnet Freight Rail, 2021).

The railway lines that Transnet freight rail uses for the transportation of heavy loads are designed using the conventional pearlite steel of grade R260 (Transnet Rail Network – Technical, 2021). This steel grade is composed of high carbon content and alloying elements such as manganese and chromium (Transnet Rail Network – Technical, 2021).

2.1.2 Rails profiles and grades

Profillidis (2006) study investigation focused on Railway Management and Engineering. The investigation findings reported that prior to the 20th century, most of the countries globally had to choose between two different types of cross-sectional shapes (profiles) of the rails.

The first option was flat bottom rail; this rail shape can be laid directly on the sleepers. The second option was bullhead rail; this rail shape was double headed and it used to sit on the chair with the expectation that when the upper part was worn, then it could be inverted so as to use the lower part of the rail (Profillidis, 2006).

Around the 20th century, it was noted that the bullhead rail was not meeting expectations. Most of the countries, with the exception of some metros in the UK (United Kingdon) took a decision to discountinue the usage of the bullhead rail profile, and opted to use the flat bottom rail profile (Profillidis, 2006).

The flat bottom rail profile was composed of the head (upper part), the web, and the foot (base) regions as shown in Figure 2-1.

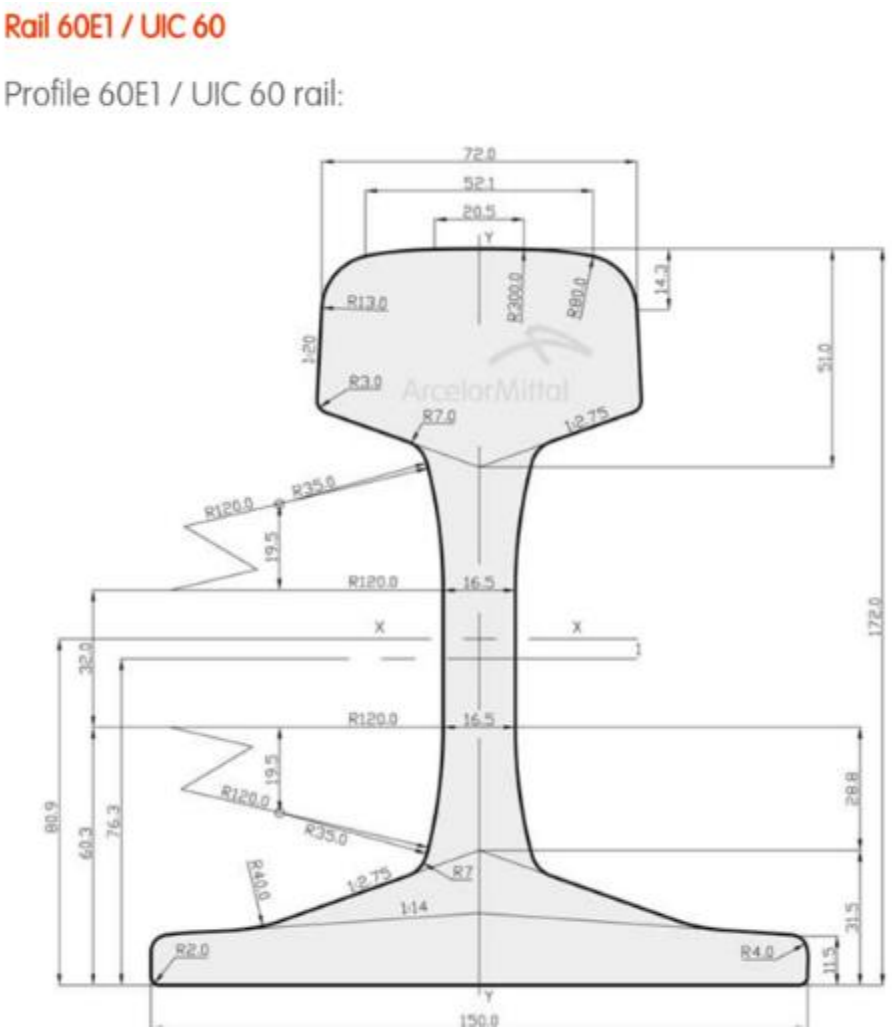


Figure 2-1: Flat bottom rail profiles (EN 13674-1: 2017).

The flat rail profiles were produced (in various sizes) according to design standards that identified vertical axis symmetric rail profiles. These standards generally introduced rail profiles which presented a suitable contact with train wheels. The two most common flat bottom profiles used in the UK were the 56E1 and 60E1 rail grades (Profillidis, 2006).

Table 2-1 showed that 60E1 rail grades with a mass weight of 60.2 kg/m was designed as per the EN 13674 – 1 standard.

Table 2-2 showed design dimensions of the 60E1 rail grades in each region (head, web, and foot) as per EN 13674 – 1 standard. The web region had a greater height compared to foot and head regions, whereas the foot region had a greater length when compared to the web and head regions.

Table 2-3 showed that surface area to volume ratio (SA:V) of web region was greater than surface area to volume ratio of head and foot region. The SA:V was calculated using the design dimension as per EN 13674 – 1 standard (Liberty OneSteel, 2017).

Table 2-1: Dimensions o-f R260 – 60E1 rail according to EN 13674 - 1 standard.

Type of rail	Standard	Dimensions mm					Section (S)	Mass (m)
		H	B	C	D	E	(mm^2)	(kg/m)
60E1	EN 13674 - 1	172.00	150.00	72.00	51.00	16.50	7686	60.21

Table 2-2: Dimensions of R260 – 60E1 rail regions according to EN 13674 - 1 standard.

60E1 – R260 rail regions	Length (mm)	Height (mm)	Width (mm)
Head	72.00	51.00	20.50
Web	19.50	89.50	16.50
Foot/Base	150.00	31.50	11.50

Table 2-3: Surface area – Volume ratio (SA: V) of the 60E1 - R260 regions (Liberty OneSteel, 2017).

60E1 – R260 rail regions	SA: V
Head	2.5
Web	3.3
Foot/Base	2.7

Depending on the country and their requirements, rails can be graded by tensile strength (according to UIC – International Union of Railways), hardness (European Standards), and weight per standard length (Profillidis, 2006) .

Profillidis (2006) reported that wear resistance rail grades UIC 900A and 900B which were mostly used in UK had a minimum tensile strengths of 88 kg/mm2 and 103 kg/mm2

respectively. This was to be different when it came to the grading of the American rails which were reported to have a minimum tensile strength of 90 kg/mm2.

Meader (1999) study investigation focused on the welding for railroad industry. The study investigation reported that high strength rails included surface hardness for rails of at least 300 Brinell, and for rails with a surface hardness between 341 - 388 Brinell on alloy and heat treated rails. Meader (1999) further reported that high strength rail had greater yield strength and tensile strength when compared to standard rails.

Table 2-4 showed that the high strength rail grade had better yield and tensile strength when compared to the standard rail grade.

Table 2-4: The required tensile properties for standard and high strength rails (Meade 1999).

Rail grade	Yield strength (MPa) Min	Tensile strength (MPa) Min	Elongation in 50 mm (%) Min
Standard	483	965	9
High strength	759	1172	10

On rails that are graded by weight per standard length, the UK and North America grade their rails in pounds per yard (lb/yd) with the normal range being 115 lb/yd to 141 lb/yd which is equivalent to 57.0 kg/m to 69.9 kg/m respectively according to European grading standard. In Europe, the normal range is 40 kg/m to 60 kg/m.

Knupp et al. (1978) study investigation focused on the review of the manufacturing, processing and the use of rail steels in North America. The investigation reported that the heaviest rail mass produced had the weight of 155 lb/yd which is equivalent to 76.9 kg/m according to European standard.

2.1.3 Rail steel materials

In 18th century, rails were made of a cast iron material. These rails were found to be prone to failures, which was largely contributed by their brittle behaviour (Cannon et al., 2003). The brittle nuture of these rails made it difficult for the load to be redistributed within plastic deformation (Cannon et al., 2003).

Around the 19th century, the cast iron rails were gradually replaced with steel rails (Cannon et al., 2003). The steel rails were preferred since they were proven to have good mechanical

properties, especially strength and ductility which were better than those of cast iron rails (Cannon et al., 2003). Majority of the countries in the world have shifted from the utilization of the cast iron rails, to the new and modern steel rails (Cannon et al., 2003). Corus Rail Products (2008) introduced three rail grades of steels (Table 2-5) which were graded by tensile strength and are commonly found in the UK and North America.

The three introduced rail grades steels were in accordance with UIC specifications and had no heat treatment specifications. The three rail types were mostly preferred because they showed good and acceptable ranges of chemical composition, tensile strength and elongation of rail steels (Cannon et al., 2003).

Table 2-5 showed that rail grade 900A and 900B which were graded by tensile strength had high tensile strength and carbon content that was above 0.55 wt%. Both rail grades had maximum elongation (%) of 10%. Whereas the rail grade 700 which was also graded by tensile strength had relatively low tensile strength and carbon content, but high elongation when compared to the other two grades.

The Institute of Rail Welding-Cambridge-UK also introduced three rail grades which were graded by hardness and are in accordance with Europen specification. These rail steels were found to be mostly common in UK rail network.

Table 2-6 showed that the tensile strength and carbon content was high for 260 rails grade and 350HT rail grade compared to 220 rail grade. The high carbon content and tensile strength on the two rail grades was influenced by high average hardness values, whereas 220 rail grade had low average hardness value. The maximum carbon content on the rail grade 220 was 0.60 wt%, when compared to 260 rail grade and 350HT rail grade which had maximum carbon content of 0.80 wt% and 0.82 wt% respectively. The carbon content found on the 260 rail grade, and 350HT rail grade was in the range of eutectoid steel (0.8 wt% C) (Bramfitt 2001).

Table 2-5: Three grades of rails introduced by Corus Rail products (2008) (UIC860: 2008).

Grade (MPa)	Tensile Strength (MPa)	Elongation (%)	Chemical composition (wt%) Fe is the bulk				
			C	Mn	Si	S	P
700	680-830	≥ 14	0.40-0.60	0.80-1.25	0.05-0.35	≤ 0.050	≤ 0.050
900A	880-1030	≥ 10	0.60-0.80	0.80-1.30	0.10-0.50	≤ 0.040	≤ 0.040
900B	880-1030	≥ 10	0.55-0.75	1.30-1.70	0.10-0.50	≤ 0.040	≤ 0.040

Table 2-6: Three grades of rail steels introduced by institute of Rail Welding (EN13674-1:2018).

Grade	Hardness (HB)	*Hardness (HV_{10})	Tensile Strength (MPa) min	Elongation (%) min	Chemical composition (wt%) Fe is the bulk				
					C	Mn	Si	S	P
220	220-260	220-260	770	12	0.50-0.60	1.0-1.25	0.20-0.60	0.008-0.030	≤ 0.030
260	260-330	260-342	880	9	0.70-0.80	0.95-1.25	0.20-0.60	0.008-0.030	≤ 0.030
350HT	350-390	361-407	1175	9	0.70-0.82	0.65-1.25	0.13-0.60	0.008-0.030	≤ 0.025

*Minimum hardness on the weld shall not be less than p-30 HV_{10} and the maximum hardness on the weld should not exceed p+60 HV_{10}, where p is the average hardness on the parent rail.

Rail grades steels that were produced by Corus Rail Products (2008) (Table 2-5), and those that were produced by The Institute of Rail Welding-Cambridge-UK (Table 2-6) had a carbon content that was slightly lower than the carbon content found in eutectoid steels (Figure 2-2). Whereas the 900A grail grade steel had a carbon content of up to 0.8 wt% which was in the range of eutectoid steel (0.8 wt% C) (Bramfitt 2001). The rail grade steels microstructure were found to be dominated by pearlite structures with a small amount of ferrite which covered the grain boundaries of pearlite.

The pearlite structures on these rail grade steels were found to consist of alternating lamellae of ferrite and cementite. These findings were consistent with Franlin et al. (2008), and Garnham and Davis (2008) findings. Franlin et al. (2008) investigated the modelling rail steel microstructure and its effect on crack initiation, whereas Garnham and Davis (2008) investigated the role of deformed rail microstructure on rolling contact fatigue initiation.

Bramfitt (2001) investigation focused on steels near eutectoid in the encyclodia of materials. The study reported that the mechanical properties of carbon steels were influenced by the volume fractions of ferrite, pearlite and cementite, which were primarily determined by the carbon content.

In addition to carbon content, there were other elements which were included in the composition of these rail steels as noted in Table 2-5 and Table 2-6. The presence and importance of manganese and silicon in these rail steels was mainly to counter the effect of the unavoidable contaminants such as sulphur and phosphorus (Schroeder, 1982).

Gomes et al. (1997) study investigation focused on effect of microstructural parameters on the mechanical properties of eutectoid rail steels. The study reported that these mechanical properties were also related to the interlamellar spacing of the pearlite for a given carbon content. Gomes et al. (1997) study further reported that rail steels with high carbon content were nearly fully pearlite, this meant that the changes in the mechanical properties depended on pearlite interlamellar spacing variation.

Interlamellar spacing variations can be controlled by cooling rate of rail steels during manufacturing. This means that fast cooling rate led to smaller interlamellar spacing, and slow cooling rate led to wider interlamellar spacing (Gomes et al., 1997). Consequentially, the decrease in the pearlite interlamellar spacing led to an increase in mechanical properties (hardness and tensile properties).

The relationship between the pearlite interlamellar spacing and the mechanical properties (hardness and tensile properties) indicated that pearlitic rail steels were depended on the prio austenite grain size and temperature at which transformation of pearlite occured. This meant that austenitizing temperature had a directly proportional relationship with prio austenite grain sizes. As austenitizing temperature was increased, the prio austenite grain sizes also increased. The increase in austenitizing temperature and prio austenite grain sizes influenced an increase in pearlite interlamellar spacing. The mechanical properties of the rail steel decreased with an increase in pearlite interlamellar spacing.

Table 2-7 showed relationship between transformation temperature, pearlite interlamellar spacing, and tensile and yield strength. At a high transformation temperature, wider pearlite interlamellar spacing was produced. Wider pearlite interlamellar spacing yields lower yield and tensile strength, and narrow interlamellar spacing yields higher yield and tensile strength.

Table 2-7: Changes in yield and tensile strength with the variations of interlamellar spacings and cooling rates of a pearlitic rail steel (Gomes et al. 1997).

Austenitizing temperature (°C)	Transformation temperature (°C)	Mean true interlamellar spacing (nm)	Yield stress (MPa)	Tensile strength (MPa)
1150	560	225	613	997
	610	291	542	954
	640	353	483	902

2.1.4 Pearlitic microstructure formation

The lamellar microstructure, which is also known as `pearlite` was formed during a eutectoid transformation (Mittemeijer, 2010). The pearlite microstructure is characterized by broad ferrite (α) and small cementite (Fe_3C) lamellae.

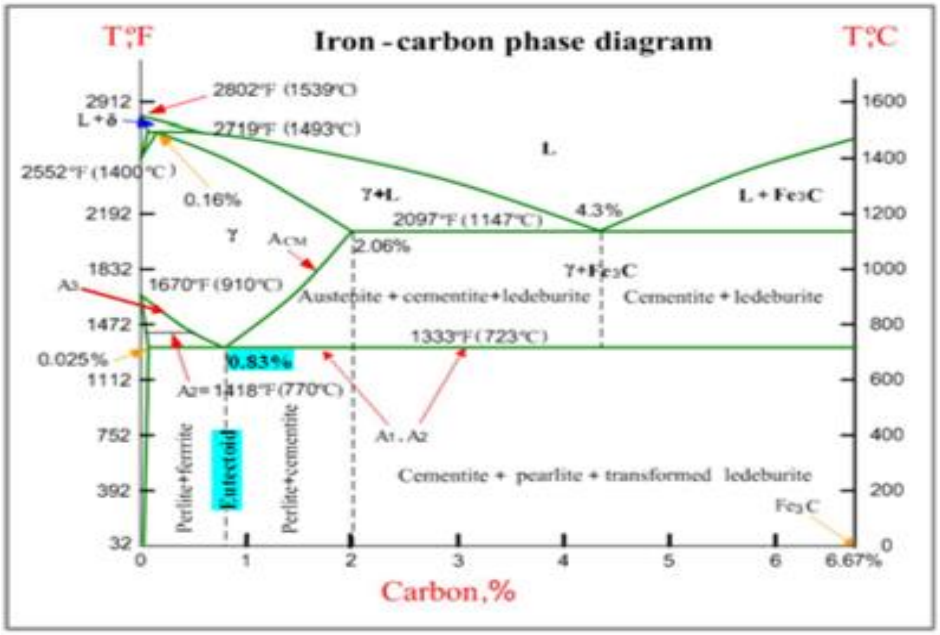


Figure 2-2: Phase diagram of iron-carbon (SubsTech 2012).

Mittemeijer (2010) study reported that by applying the lever rule at temperatures below the eutectoid, pearlite composition can be adjusted to about 90 wt% α and 10 wt% Fe_3C. It was also worth noting that the mass and volume percentage of α and of Fe_3C were almost the same,

this was supported by the fact that the density of α and of Fe_3C were approximately equivalent (7.7 and 7.9 g/cm^3, respectively).

Figure 2-2 showed that during the cooling process from A_1 temperature, pearlite (α) colony and Fe_3C lamellae nucleated at an austenite (γ) grain boundary to ensure that a cooling process from the γ field occured for both hypo-eutectoid alloy (below about 0.8 wt% C) and hyper-eutectoid alloy (above 0.8 wt% C).

Upon cooling from the γ field, a hypo-eutectoid alloy started by forming α particles (formation of proeutectoid ferrite) until A_1 was reached, where eutectoid transformation occured for the remaining C-enriched γ phases. The hyper-eutectoid alloy started by first forming Fe_3C particles (formation of proeutectoid cementite) until the A_1 temperature was reached at which the eutectoid transformation occured for the remaining C-impoverished γ phase. Both the formed proeutectoid phases nucleated and grew at the γ-grain boundaries.

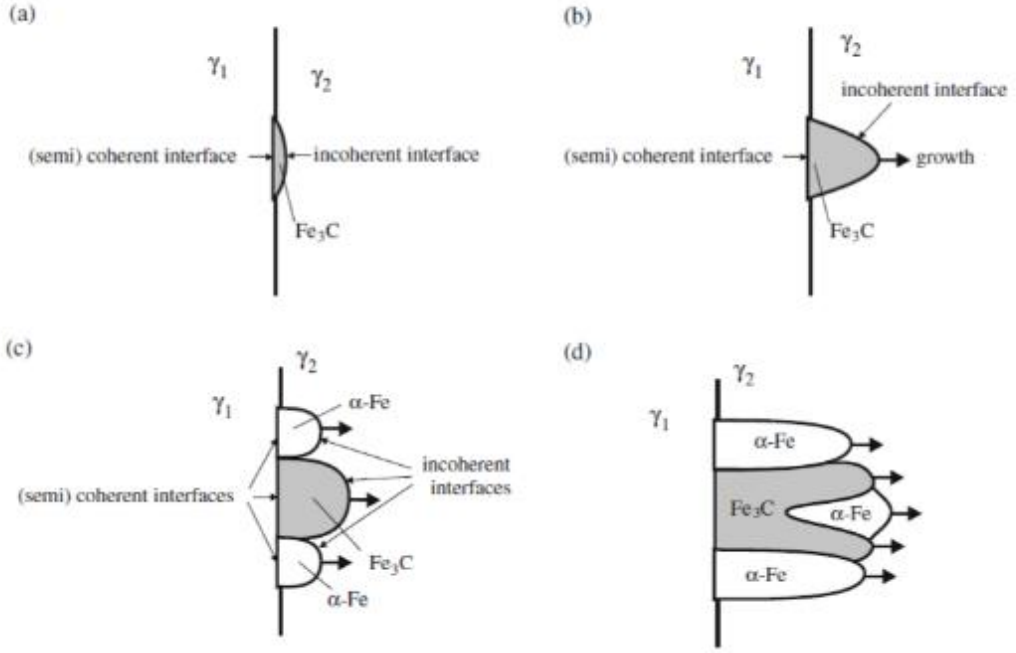


Figure 2-3: Schematic illustration of the formation of pearlite from γ: (a) Nucleation of an Fe_3C crystal at the interface of two γ grains, γ1 and γ2, establishing a semi-coherent interface with γ1 and an incoherent interface with γ2. (b) Growth of the Fe_3C grain into γ2. (c) Nucleation of α at the γ1/ γ2 interface in the C depleted γ matrix of γ2 adjacent to the Fe_3C grain. (d) Branching of Fe_3C lamella (Mittemeijer 2010).

The investigation by Mittemeijer (2010) further reported that the initiation of the pearlite colony was formed through Fe_3C crystals at the γ-grain boundary. A low energy interface which might be semi-coherent arised when the Fe_3C crystal nucleated first, this establishes one of the neighbouring γ grains (γ_1 in Figure 2-3a).

The low energy interface was energetically favourable and exhibited a good packing of atoms. Consequently, the transfer of atoms was challenging and thus resulted in a semi-coherent interface with low mobility. In the case where an incoherent high energy interface arised, the Fe_3C crystal nucleated and established another neighbouring γ grains (γ_2 in Figure 2-3b). This interface resulted in a bad packing of atoms in both grains of Fe_3C and γ_2; the transfer of atoms was easier and thus resulted in a incoherent interface with high mobility (Mittemeijer 2010).

Having high mobility of atoms resulted in growth of Fe_3C grain. As Fe_3C grew into the γ_2 grains, carbon got depleted, which led to increasing the driving force for the formation of α grains. Within the γ-grain boundary, the α grains were formed adjacent to Fe_3C grain. This meant that the newly formed relationship of α and Fe_3C grains also had a semi-coherent interface with γ_1 and, an incoherent interface with γ_2 grains (Figure 2-3c) (Mittemeijer 2010).

Hence, this type of nucleation formed a lamellar structure of α and Fe3C (pearlite colony) at the γ-grain boundary, which grews laterally into the γ_2 grains. Branching of an Fe_3C lamella (or an α lamella) into parallel may occur (Figure 2-3d), which in its extreme form resulted in a pearlite colony consisting of single crystal of Fe_3C and single crystal of α (Mittemeijer 2010).

The growth rate of the eutectoid colony depended not only on the distribution speed of the components but also on the interlamellar spacing (Mittemeijer, 2010). This meant that the larger the interlamellar spacing, the slower the colony growth rate. Therefore, it was expected that low eutectoid transformation temperatures result in fine interlamellar spacing, which compensated for the low diffusion rate at low temperature (Mittemeijer, 2010).

It was also noted that spherical Fe_3C grains had the smallest surface area per unit volume than lamellar product geometry grains (Mittemeijer, 2010). Hence, during the eutectoid transformation, a lamellar product geometry developed instead on the spherical Fe_3C grains in an α matrix (Mittemeijer, 2010). The small surface area per volume found on spherical Fe_3C grain led to a slow diffusion process whereas it could have been faster on the lamellar product geometry (Mittemeijer, 2010). However, increasing system energy due to the increase of α/Fe_3C interface energy upon decreasing the interlamellar spacing prevent incidence of vanishingly small values for interlamellar spacing (Mittemeijer, 2010).

2.1.4.1 Microstructure and mechanical properties of the pearlitic steel

Kalouse et al. (1985) study investigation focused on wear resistance and worn metallograph of pearlite, bainite and tempered martensite rail steel microstructures of high hardness. The study

reported that hardness of rail steels had a directly proportional relationship with the tensile strength and wear resistance of the rail steels.

The findings of the investigation further reported that as hardness of the rail steels increased, the tensile strength also increased, which in turn enhanced wear resistance (Kalouse et al., 1985). The hardness of pearlitic rail steel was increased by decreasing the interlamellar spacing and increasing alloying elements like carbon, manganese, and chromium (Gladman et al., 1972). High carbon content and fine pearlitic spacing resulted in rail steels with high hardness and yield strength (Gladman et al., 1972). Therefore, the shorter the interlamellar spacing, the better the mechanical properties of the rail steel (Gladman et al., 1972).

Gladman et al. (1972) used Equations 2-1 to prove the strength of ferrite/pearlite steels. Gladman et al. (1972) work showed that the interlamellar spacing of ferrite and cementite lamellae in pearlite become more important with an increase in the amount of pearlite.

Hyzak and Bernstern (1976) study investigation focused on fully pearlitic microstructures in steels containing 0.81% C. The investigation did not only evaluated the effect of pearlite interlamellar spacing, S, but also the effect of austenite grain size, d, and pearlite colony size, P, on mechanical properties. The findings of the investigation reported that the hardness of pearlitic steel increases as the interlamellar spacing decreases. It also showed that with the decrease in interlamellar spacing, the strength, toughness and wear resistance of the steel showed improvement (Gladman et al., 1972).

Equation 2-1: Yield strength

$$Yield\ strength\ (MPa) = 2.18\left(S^{-\frac{1}{2}}\right) - 0.40\left(P^{-\frac{1}{2}}\right) - 2.88\left(d^{-\frac{1}{2}}\right) + 52.30$$

Wear behaviour of pearlitic rails had been studied at the Facility for Accelerated Service Testing (FAST) in Pueblo Colorado (Gladman et al., 1972). FAST used 4.8-mile-long pearlitic rail steel to study the wear behaviour (Gladman et al., 1972). The wear behaviour was determined for two steels exhibiting the same 100% pearlitic structure, and one had a greater hardness than the other (Gladman et al., 1972).

Brown and Krauss (1982) showed that wear is a three-stage process, where the 1st stage involved severe plastic deformation in the surface layer of the rail. When two steels were evaluated, the depth of the deformed zone was found to be shallower in the harder steel.

The 2nd stage consisted of the development of subsurface cracks in severely deformed layer, generally at the interface of the deformed layer and the un-deformed microstructure. The crack propagation to the surface of the rail and associated spalling off of small slivers or flakes of the rail constituted the 3rd stage of wear. This sequence of deformation and fracture was repeated many times to produce substantial rail wear.

Girsch and Heyder (2006) studied advance pearlitic rail steels with the following grades: R260, R350HT, 370LHT, 400UHC and advance bainitic rail steels with grade DOBAIN430. The research focused more on improving the wear and rolling contact fatigue (RCF) resistance.

The investigation reported that RCF resistance of the rail grade 370LHT was approximately 20% higher when compared compared to the RCF resistance of rail grade R350HT, but it was 50% higher when compared to the RCF resistance of the standard rail grade R260 (Girsch and Heyder, 2006). Investigation findings further reported that wear and RCF performance of the bainitic rail steel with grade DOBAIN430 were similar to pearlitic rails of grade 370LHT (Girsch and Heyder, 2006).

Chaves et al (2009) investigation study focused on effect of the microstructure on steel and the wear resistance of a pearlite steel. AISI1080 steel material and pin-on-disc sliding wear testers were used to analyse the microstructure effect on the wear resistance.

AISI1080 steel was isothermally treated at five temperatures using dilatometer with an intention to obtain pearlite, bainite and martensite structures. After these treatments, bainite and martensite samples were tempered at 500 ºC. It was possible to achieve pearlitic specimens with interlamellar spacing ranging from 70 +/- nm to 243 +/- nm.

Chaves et al. (2009) investigation reported that the wear resistance of the sample with pearlitic structures was inversely proportional to interlamellar spacing. It was further observed that fine pearlite had 30% lower mass loss and superior sliding wear resistance than coarse pearlite, and fine pearlitic structures tended to present a better wear performance when compared to bainitic or martensitic structures.

Nikas et al. (2017) investigation study focused on the characterizing deformed pearlitic rail steels on a R260 grade of rail steel head region. To achieve the objectives of the investigation, Nikas et al. (2017) measured the hardness of pearlitic lamellas, so that the results could give an overview of the deformed microstructure in the surface of the rail, this was done by using knoop hardness testing method. The microstructure characterization of the material was done

by optical microscope and scanning electron microscopy with an intention to evaluate the changes in the microstructure due to large deformation. The study findings reported that a strong steep gradient can be observed in the top 50 microns per meter of the rail, while deeper into the rail.

2.1.5 Joining of rail ends into tracks

2.1.5.1 Bolted tracks.

Historically, rails were bolted together to produce a continuous railroad track. The ends of adjoining rails were connected using two bore through steel plates which were known as fishplates at UK and joint bars at North America (Ookaboo, 2009). The steel plates were used in pairs to connect the rail ends, each side was connected and bolted with usually four or six bolts per joint (Ookaboo, 2009).

North American practice adviced that the bolts should be placed in opposite directions as it would reduce the risk of derailment in the event that a wheel flange strikes the joint which would results into the bolts being sheared (Ookaboo, 2009). North American practice further claimed that this practise ensured that the rails were less likely to be checked out of alignment (Ookaboo, 2009). Whereas, the UK practice made all bolt heads on the same side of the rail (Indiamart, 2014).

Wu and Thompson (2003) investigation focused on the impact noise generation due to a wheel posing over rail joints. The investigation reported that when joining rail ends, small gaps (usually 5-20 mm width) know as expansion joints should be left between the rail ends to allow for expansion on the rails in hot conditions. The investigation further reported that the the rail end holes through which bolts pass are oval shaped. The oval shape design was to allow free movement and expansion for bolted rails. The UK practice made rail joints on both rails to be adjacent to each other, whereas North American practice installs the rail joints in a sequential system.

Wu and Thompson (2003) investigation also reported that there are two requirements of these assembly joints. The first requirement which was considered as a geometrical requirement was intended to achieve a smooth running surface during the assembly of joints, in order to achieve that, the bolted rail ends should be connected vertically and horizontally. The second requirement which was considered as a mechanical requirement intended to compensate for rail discontinuity at the joints by using fishplates to cover the lost vertical bending stiffness.

To satisfy the mechanical requirement, the cross section of the fishplates should be sufficiently thick and the bolts must be tightly fastened. However, the tight fastening of the bolts contrast with the other mechanical requirement of free axial movement of the rail ends at the joint to cope with expansion. Free axial movement was very important as it prevented the creation of high axial rail forces which could be caused by changes in the temperature of the weather (Wu and Thompson, 2003).

Kerr and Cox (1999) investigation study focused on analysis and tests of bonded insulated rail joints subjected to vertical wheel loads. The investigation findings reported that the bending stiffness of two fishplates was much lower than that of the rail. So, even when the fishplates were tightly bolted to the rails, the assembly joint remained the weakest structure in the rail track.

The small gaps that were left between the rails resulted into noisy and annoying sounds when the train passes over joint tracks. The sound was identified to be as a result of high dynamic impact forces which were created by an interaction between train wheels and rail joints. The interaction between the train wheel and rail joints led to an increase in vertical deflections and dynamic forces, causing worsening of the joint assembly and depression of the supporting ballast in the vicinity of the joint (Kerr and Cox 1999).

The rail joint tracks became financially unsustainable especially on heavily operated railroads with high train speeds and high axle loads. On top of the high maintenance cost, the joints needed to be continuously lubricated, the joints also damaged the train wheels and increased power consumption of the running train (Kerr and Cox 1999).

The rail joints tracks had defects that resulted into breaking of the running surface of the railway during service. The study investigation by Lim et al. (2003) focused on stability of continuous welded rail track. The findings of the study investigation reported that with the introduction of modern high speed trains, the rail joint had many failures which included the development of cracks around the bolts holes.

The rail joint problems led the railroad industry to look for railroad structure without joints. Around the 20th century, Germany became the first country in the world to introduce the first continuous welded rail track. Continuous welded rail tracks were reported to be a sutaible replacement, especially on the railroads that accommodate high axle loads and trains with high speeds.

2.1.5.2 Continuous welded rail tracks

The railroad industries around the world have modernized their railroads by implementing continuous welded rail (CWR) tracks to accommodate high axle loads and trains with high speeds. Within the continuous welded rail tracks, the rail ends are welded together to form a continuous rail with a long length. Skyttebol et al. (2005) reported that the use of welding methods for joining rails was standard procedure all over the world.

Lim et al. (2003) investigation reported that continuous welded rail tracks had fewer joints when compared to bolted rail tracks, the low number of joints resulted into a reduction in impact loading, track maintenance costs, and ensured a smooth ride. Lim et al. (2003) investigation further reported that trains can now run at high speeds with less friction and power consumption on the continuous welded rail tracks. Tawfik et al (2008) investigation study focused on alleviating tensile residual stresses in flash butt welds by localized rapid post weld heat treatment. Tawfik et al. (2008) and Lim et al. (2003) findings were aligned.

Railroad rails can physically expand in hot weather and contract in cold weather conditions if they are not restricted (Brown et al., 1976). To prevent longitudinal rail movement relative to the sleepers on which the rails were laid, railroads usually used anchors or clips for restriction (Brown et al., 1976). Anchors were more often used with wood sleepers, while special clips were used for fastening the rail concrete or steel sleepers (Brown et al., 1976). However, if longitudinal restriction was insufficient, the track could be distorted in hot weather and thus a derailment could occur (Brown et al., 1976).

When laying new rails or replacing defective ones, the rails could be pre-stressed if the rail temperature during laying differs from what was desirable (Tawfik et al., 2008). Brown et al. (1976) investigation focused on the method of laying railroad rail. The investigation reported that their were two stressing practice that were used for laying railroad rails, the railroad rails can either be expanded by heating, or they can be stretched by using hydraulic equipment.

Brown et al. (1976) further reported that the railroads should be tightly fastened to the sleepers in their expanded status. This practice ensured that rails would not expand much more during hot weather. In cold weather, their contraction would be prevented by tight fastening.

Garcia et al. (2017) reported that CWR took over from bolted tracks around the 1930`s. The technologies that were introduced to achieve a smooth continuous rail track were flash-butt and aluminothermic welding processes (Garcia et al., 2017).

Garcia et al. (2017) identified that the advantages of CWR over the bolted joint tracks were that they reduced the maintenance costs of the tracks, improved track stability, allowed higher running speeds for trains, and improved passenger comfort.

Tawfik et al. (2008) pointed out that poorly executed continuous welded rail (CWR) installations can result in structural discontinuities due to variation in microstructure, mechanical properties and residual stresses when compared to parent rails. These discontinuities in CWR could increase the risk of train accidents and human fatalities.

Commonly used continuously welded rails methods include flash-butt welding (FBW), gas pressure welding (GPW), and thermite welding (TW). FBW and GPW are mostly used with stationary equipment and are used to weld large section of rails, which are transported out to tracks, whereas the TW is used in an in-track since it provides easy alignment and simplicity. This method can also be considered for replacing defective or broken rails (or welds) and installing rail insulation joints (Saarna and Laansoo, 2004).

Saarna and Laansoo (2004) study investigation reported that the disadvantages about using TW over FBW were that about 17% of rail failures occured in TW when compared with 7.9% contributed by FBW. Whereas, the advantages of using the TW method included the simplicity and robustness of the necessary equipment, the ability to conduct the process on-site, low cost, portability, independence from electrical power, and the quality of the welding consumables was ensured by strict quality control.

2.1.6 Thermite welding

2.1.6.1 Thermite welding process

Aluminothermic/Thermite welding (TW) method is one of the most used welding methods in railway industry to weld rails into CWR tracks. This method uses a thermite reaction to join two rail ends together (Yang et al., 2018). The two rail ends welded are carefully aligned and fixed with a gap of about ~24 mm between them (Webster et al., 1997). Thermite welding kits consist of one aluminothermic charge, one self-tapping thimble, the mould clamps and the aluminothermic crucible (Yang et al., 2018).

The ceramic mould is then placed around the gap and sealed by luting sand (Figure 2-4). The reaction is composed of an oxidised iron alloy powder mixture, metallic aluminium and other alloys, which are then poured into a crucible placed over a ceramic mould as shown in Figure 2-4 (Lonsdale, 1999).

The mixture promotes a thermite reaction as it is mixed with alloy additives such as ferromanganese to ensure that the composition of the mixture is adjusted so that the weld rail composition can be comparable to the parent rail (Lonsdale, 1999). The thermite mixture which is poured in the crucible and placed in the ceramic mould is ignited by an ignition agent (Lonsdale, 1999).

The thermite welding process is based on the reaction:

Equation 2-2: Thermite welding reaction 1

$$Iron\ oxide + alloy\ element + aluminium = steel + slag + heat$$

The reaction takes place in a vessel, since the thermite mixture has an ignition point in excess of 2000 ℃ special means must be adopted for the ignition (Yang et al., 2018). The reaction immediately starts by igniting the main aluminothermic charge, which lasts 5-35 seconds (Lonsdale, 1999). When the reaction is complete, molten steel and molten aluminium oxide slag should be produced in a molten state (Lonsdale, 1999). The specific gravity difference should separate these two in a crucible (Lonsdale, 1999). Aluminium slag should float to the upper part of the crucible (Lonsdale, 1999). This thermite reaction should be the reduction reaction where aluminium reduces oxidized iron as described in Equations 2-3 and 2-4 (Lonsdale, 1999).

Equation 2-3: Thermite welding reaction 2

$$Fe_2O_3 + 2Al \rightarrow Ale_2O_3 + 2\text{Fe}$$

Equation 2-4: Thermite welding reaction 3

$$\mathbf{3}Fe_3O_4 + \mathbf{8}Al \rightarrow \mathbf{4}Ale_2O_3 + \mathbf{9Fe}$$

After removing the slag, the molten steel (at a temperature above 2000 ℃) is discharged into a ceramic mould which exposes the end of the rail to superheated steel, welding the two rail ends together, then the tapping and solidification process takes place (Yang et al., 2018). This process takes approximately 4 minutes (Meade, 1999). This process is followed by the trimming, whereby excess metal around the rail is sheared off and removed by grinding (Meade, 1999). The time required from the start of the process and when the rail is ready for a train to run over it is usually approximately 45 min to more than an hour, depending on the section and ambient temperature (Liveleak, 2013).

The reliability of thermite welds is difficult to assess because each one is implemented using a separate casting (Yang et al., 2018). The continuous use of TW for joining rails is attributed to its portability, flexibility, convenience and cost-effectiveness (Yang et al,. 2018).

Thermite welds properties are influenced by many variables which includes; alignment of rail ends, size of the gap between rail ends, rail cross section variance, cleanliness of rail ends, work quality of mould assembling, mould cleanliness, amount and duration of preheat, excessive rail movement during solidification, weather during welding, welder skill, and time until mould is removed (Yang et a., 2018). The ignorant of these variable can lead to segregations, inclusions and surface defects that have harmful contributions to integrity of the welded rails.

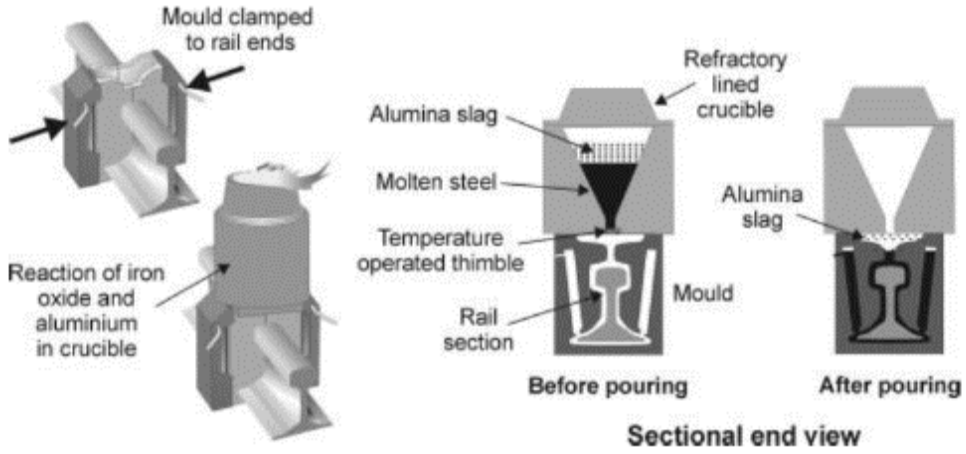


Figure 2-4: Schematic of the rail thermite welding process (Altintas 2013).

Meade (1999) study investigation reported that the role of aluminium within the TW method was to react with oxide and act as an oxidizer in the weld charger to reduce the porosity and increase the rail weld's mechanical strength. In ensuring a quality weld, the aluminium quantity must be carefully controlled (Meade, 1999). Meade (1999) further reported that having too much aluminum can increase the weld brittleness, hence it was important to control all weld charge contents and keep them within specifications in order to achieve acceptable weld quality.

Table 2-8 showed the composition and tensile strength of parent rail and two thermite welds rails (weld 1, and weld 2). The parent rail was shown to have a carbon content of 0.75 wt%, which was close to the carbon content of the eutectoid steel (0.80 wt%). Whereas weld 1 and weld 2 had carbon content of 0.54 wt% and 0.48 wt% respectively. The rail steel had high

tensile strength of 906.5 MPa, when compared to tensile strength of weld 1 and weld 2 which were 801.8 MPa and 792.8 MPa respectively. The difference in tensile strength between rail steel, weld 1, and weld 2 indicated that with high carbon content, high tensile strength will be obtained.

Table 2-8: Composition and tensile properties of a rail and two standard thermite welds (Myers et al.,1982).

Metal	Tensile strength (MPa)	γ (%)	Chemical composition (wt%) Fe is the remainder									
			C	Mn	Si	Al	S	P	Ni	Cr	Mo	Ti
Rail	906.5	12	0.75	0.84	0.17	ND	0.022	0.020	0.08	0.04	0.01	-
Weld 1	801.8	2.5	0.54	1.40	0.38	0.68	0.019	0.031	0.04	0.01	0.10	0.05
Weld 2	792.8	1.0	0.48	1.32	0.35	0.33	0.020	0.032	0.04	0.03	0.09	0.03

Myers et al (1982) study investigation focused on the chemical composition of thermite welds in rails. The study reported that the chemical composition of thermite welds differed considerably from those of the parent rails, where the carbon content was lower, and manganese and silicon content were higher with the present of aluminum (Table 2-8).

The aluminothermic steel must have a chemical composition, carbon equivalent (C.E = C+ Mn/6), microstructure and hardness number to match that of the rail (Garcia et al. 2017). It was also noted that the weld metal hardness can be varied over a narrow range (± 20 HBS) (Garcia et al. 2017).

2.1.6.1.1 The effect of TW on the microstructure characterisation and mechanical properties.

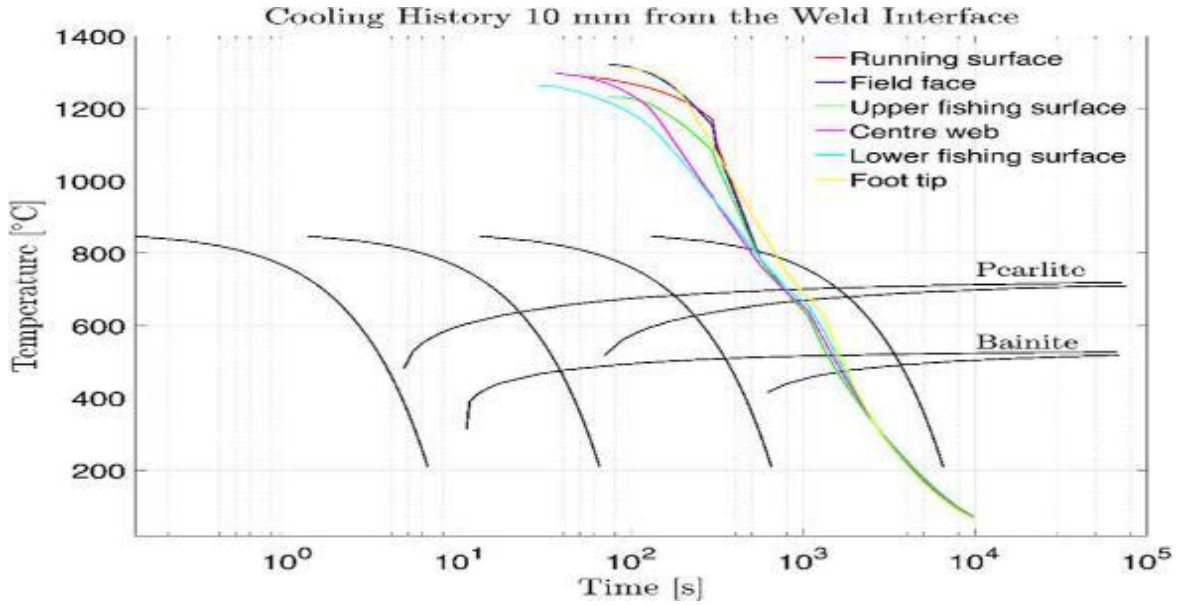


Figure 2-5: Cooling curve for different points in rail cross section and CCT diagram for R260 steel (constructed by JMatPro).

The microstructure of thermite weld largely depends on cooling rate of the rail welded joints (Myers et al., 1982). The cooling rate can either be fast or slow, and can be impacted by many factors which includes but not limited to; the amount and duration of the preheating, the weld gap between the two rail ends to be welded, the rail size, and the weather conditions (Myers et al., 1982).

The microstructure of the thermite welded rail after cooling may be estimated from the calculated cooling rate and the CCT diagram shown in Figure 2-5. The CCT diagram has been constructed by JMatPro based on the chemical composition for R260 steel grade in Table 3-1. It is vital to preheat the rail ends in order to provide a slower cooling rate, as the steel had a carbon equivalent of more than 0.42 and therefore the formation of martensite and bainite at a higher cooling rate must be avoided (Garcia et al., 2017).

The investigation by Myers et al. (1982) reported that a microstructure that consist of intragranular Widmanstattern ferrite with small isolated grains of pearlite, and ferrite at prior austenite grain boundaries was produced when a fast cooling rate was achieved on thermite weld metal (Figure 2-6a). Whereas, the slow cooling rate support formation of pearlite rather than intragranular Widmanstattern ferrite (Figure 2-6b).

Myers et al. (1982) further reported that slow cooling rate can produce a thermite weld metal microstructure that was different across the weld. The centre of the weld which was a high heat

flux area consisted of perlite and pro-eutectoid ferrite structures (Figure 2-7), whereas, away from the centre of the weld which experiences less heat than the centre of the weld, produced a mixed structure of pearlite grains in regions where intragranular Widmanstattern ferrite dominates. However, if the volume to surface ratio of the weld was big enough, the microstructure may also consist of the mixed structure of pearlite and pro-eutectoid ferrite across the weld metal (Schroeder and Poirier, 1984, and Meric et al., 2002).

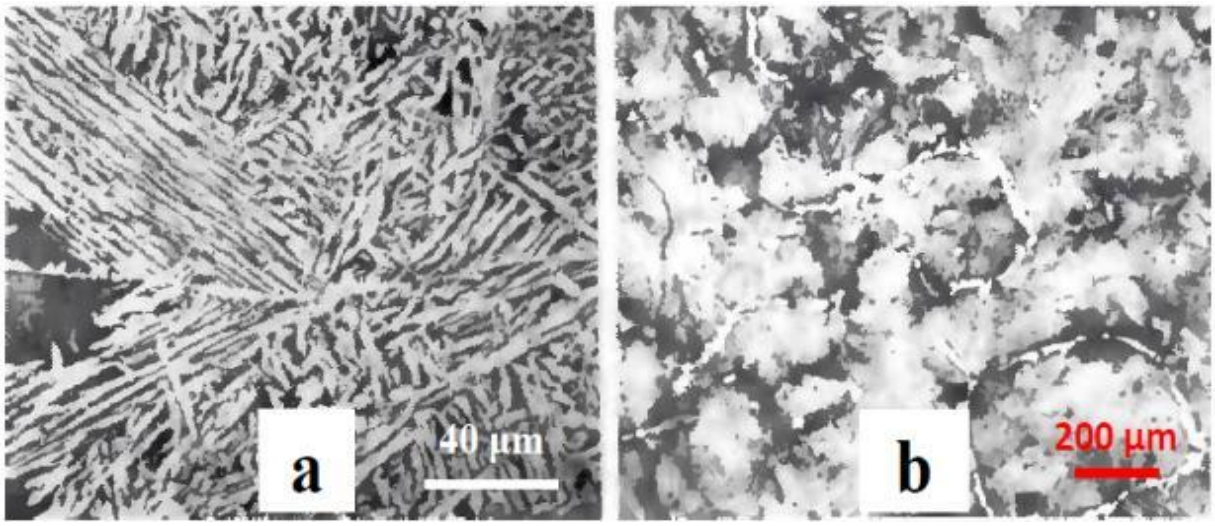


Figure 2-6: Microstructures of standard thermite welds show (a) intragranular Widmanstätten ferrite with small, isolated grains of pearlite, and (b) pearlite and pro-eutectoid ferrite (Myers et al. 1982).

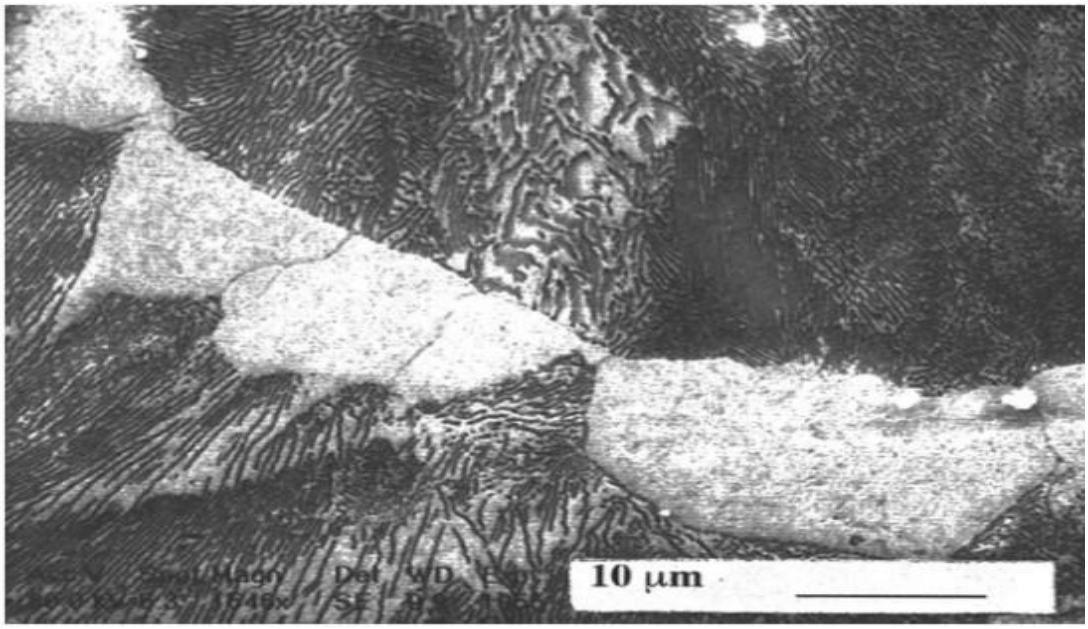


Figure 2-7: Microstructure of a standard thermite weld metal shows pearlite and pro-eutectoid ferrite at prior austenite grain boundaries at higher magnification (SEM) (Ilic et al. 1999).

The microstructure of intragranular Widmanstätten ferrite in standard thermite weld metal was associated with parallel segregated bands close to the fusion zone. Those bands consisted of pearlite with intragranular Widmanstätten ferrite. The bands were found to be rich in aluminium and in manganese (Illic et al., 1999).

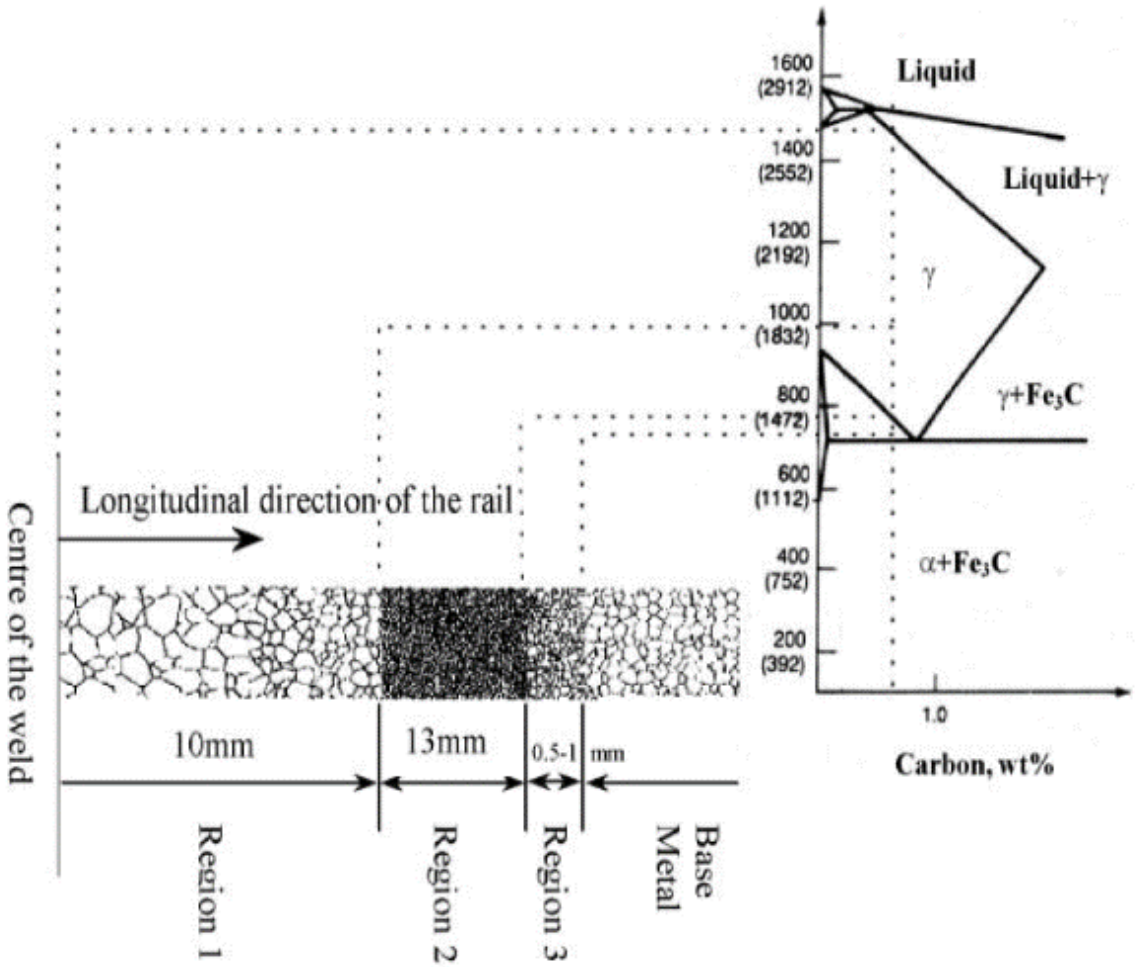


Figure 2-8: Schematic microstructure of the weldmented zone showing the correlation between changes in grain size within welded zone and the iron – carbon binary diagram along the rail after the changes TW process with their corresponding phases (SubsTech, 2012).

Region 1 was referred to as the weld centre, and it was found close to the centre of the joints. This region can be noted by the course recrystalized grains, large deformation, and high temperature in comparison to other parts of the weld (SubsTech, 2012). When moving away from the centre of the weld, the temperature was reduced, and therefore the size of the grains decreased (SubsTech, 2012).

Region 2 was referred to as the weld zone where the temperature was just above A_3 (the critical temperature in the Fe-Fe_3C phase diagram) and the plastic deformation was enough to recrystallize the whole of this region (SubsTech, 2012). Whereas region 3 was narrow than the

other 2 regions, and it was referred to as the HAZ. The temperature on region 3 was settled at the $\alpha + \gamma$ zone in the phase diagram of Fe-Fe_3C (SubsTech, 2012).

The HAZ has hardness distribution that varies, and its decreases with the move from the fusion zone towards the interface between the parent rail and the HAZ. These variation were reported by Myers et al. (1982), Schroeder and Poirier (1984), and later by Meric et al. (2002).

Myers et al. (1982) reported that the bands are harder than the non-segregated regions of the weld metal, hence the peak hardness in the HAZ was always in the region close to the fusion zone. Myers et al. (1982) further reported that the minimum hardness was mostly observed at the outer edge of the HAZ (HAZ/parent rail steel interface), where the microstructure was partially spheroidized pearlite.

The investigation by Bramfitt et al. (1997) reported that fully pearlitic head hardened rail can be between the range of 360 BHN to 380 BHN. Bramfitt et al. (1997) further reported that wear rates for head hardened rail were seen to be superior to wear rates for standard rail tests at the Association of American railroads (AAR) facility for accelerated service testing (FAST).

Although there was little correlation between thermite weld batter rate and hardness in same recent FAST work, higher rail thermite weld hardness should intuitively perform better. The good properties of high hardness had enforced thermite weld manufactures to adjust and balance their chemistry and add more of charges that can ensure harder welds, and good mechanical and microstructural properties (Bramfitt et al., 1997).

The hardness of most weld charges were improved to match that of standard rail at 285 BHN, whereas today, several thermite weld charge hardness (fully pearlitic) are available in standard hardness (305 BHN +/-20), high strength weld with a hardness level that is between 340 BHN (+/-20) to 370 BHN (+/-20) (Saarna and Laansoo, 2004).

The aluminum and manganese charge contents plays a vital role on the hardness distribution of the thermite weld, as the rail weld can either be harder or softer than the parent rail (Saarna and Laansoo, 2004). Carefully controlled aluminium content can improve the hardness of the weld, whereas controlled manganese content can have the ability to alter the rail thermite weld fracture toughness from brittle to ductility behaviour (Saarna and Laansoo, 2004). The hardness difference between the rail thermite weld and the parent rail rail can lead to uneven wear which can increase the noise level during rail service, and induce stresses on the rail (Saarna and Laansoo, 2004).

Meade (1999) reported that high hardness on the rail thermite welds were usually preferred because they increased the resistance to fatigue and deformation. Meade (1999) further reported that harder thermite welds held up more under increasingly hard axle loadings, and helped to prevent rail head depressions at the weld.

Mutton and Alvarez (2004) investigation reported that thermite weld joints that have low hardness and wide HAZ are sensitive to batter (localized plastic deformation due to variations in strength or hardness through the weld). To avoid batter, and to ensure that a comparable hardness distribution is achieved between rail thermite weld and parent rail, a short preheating must be part of the thermite weld process.

The investigation by Illic et al. (1999), and Lonsdale (1999) reported that thermite weld was cast steel and the microstructure in the fusion zone consisted entirely of coarse columnar dendrite grains aligned in the direction of heat flow (Figure 2-8). The coarse columnar dendrite grains contributed to thermite welds being brittle with low fatigue resistance . Illic et al. (1999), and Lonsdale (1999) studies further reported that in order to refine the microstructure, improve the ductility and toughness of the thermite weld, normalization heat treatment to lower the cast steel structures should be utilized.

In order to achieve good mechanical properties (tensile strength, and fracture toughness), manufactures saw it best to refined the grain size of the welds to be smaller (Mutton and Alvarez 2004). Smaller grains possess better tensile strength, ductility and facture toughness properties when compared to welds with larger grain sizes (Mutton and Alvarez 2004).

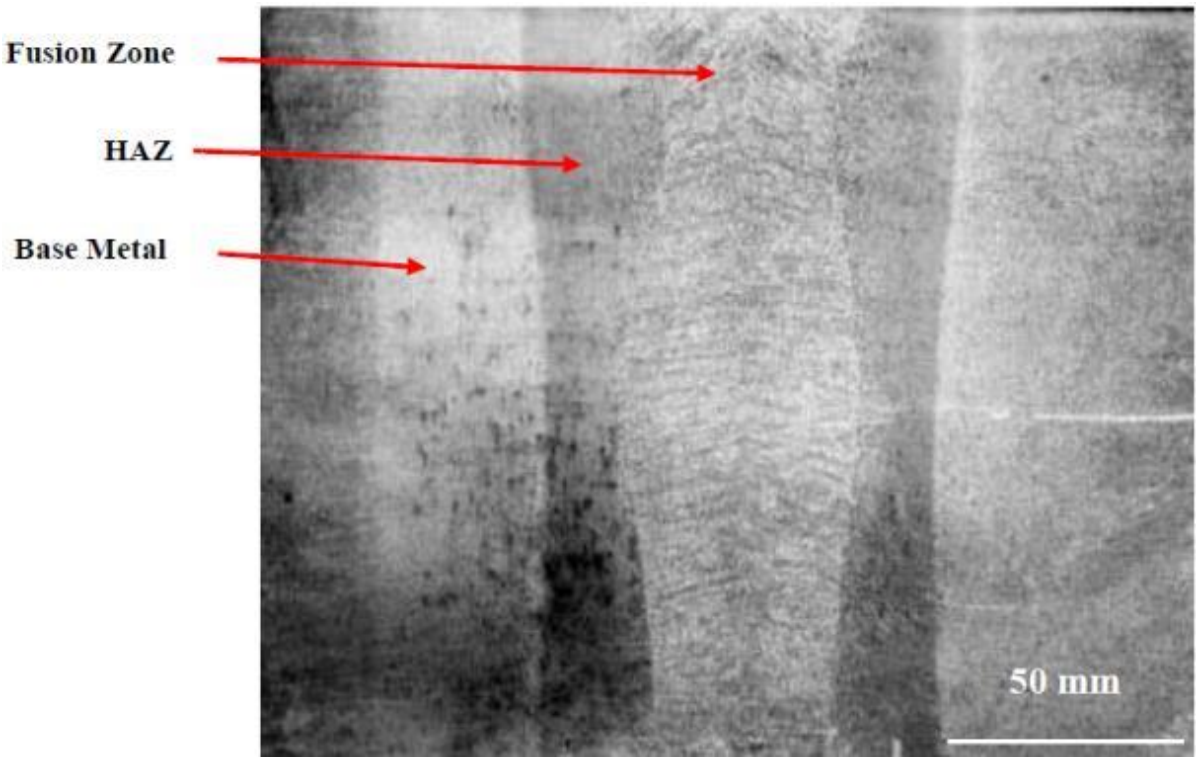


Figure 2-9: Etched and photographed macrostructure of a standard thermite weld rail with 24 mm weld gap, showing columnar grains (weld and HAZ widths are 40-50 and 15-25 mm respectively) (Webster et al. 1997).

Myers et al. (1982) reported that tensile properties results which were tested and compared between two thermite welds with slightly different chemical composition, and parent rail, showed that tensile properties of both the thermite welds were lower than that of parent rail (Table 2-8). These findings were an indicative that thermite weld exhibit low tensile ductility and impact toughness than parent rail. Microporosity, and numerous inclusions presented in the interdendrtic region of the thermite weld attributed to low tensile properties and impact toughness on the thermite weld (Myers et al., 1982).

Myers et al. (1982) investigation further reported that standard pearlite rail steel has an average yield strength of about 480 MPa, a tensile strength of about 910 MPa, an elongation of 11% (a 25.4 mm gauge length) and a reduction in area of 14% by comparison. Typical values for thermite welded rails showed a tensile strength of 790 MPa, an elongation of only 1% to 3% (a 127 mm gauge length) and a reduction in area of 1% to 3%. Myers et al. (1982) investigation also reported that even though a thermite weld was installed according to recommended procedures and was free of micro-defects; its mechanical properties were usually lower than those of the parent rail.

Schroeder and Poirier (1984) research investigation focused on mechanical properties of thermite welds of various combinations of rails which were joined using standard alloy thermite charges. The investigation reported that martensite can not be formed, regardless of the rail or weld metal composition. The research investigation further reported that Charpy impact energies with the range between 1.5J to 2.8J at 20˚C were measured. These low results were measured at the thermite weld. The rail thermite weld also showed a reduction in area that was very low and was ranging between 2% to 6% for tensile ductility, and all their surface exhibite brittle transgranular cleavage.

Illic et al. (1999) study investigation focused on mechanical properties, hardness distribution, fracture mechanism and microstructure of thermite welded rail joints before and after heat treatment (normalization at 820˚C for 45 minuts, and then air cooling at room temperature). The study reported that heat treatment for rail thermite weld joints improved the tensile properties, and altered the fracture mechanism type from brittle to ductile.

Meric et al. (2002) study investigation focused on the mechanical and metallurgical properties of the weld zone in rail thermite weld with short preheating. The study reported that the microstructure of a weld zone had no martensite, instead it had pro-eutectoid ferrite and pearlite structures.

Sergejev and Mikhailov (2008) research investigation focused on analysis of factors affecting fractures of rails welded by alumino-thermite welding. The research investigation revealed that the pores and non-metallic inclusions in rail thermite weld act as sites for stress concentration and consequently sources of cracks formation.

The study investigation by Saita et al. (2013) compared the properties of the JIS60 rail grade material (parent material) with those of thermite welded rails. The study revealed that although the chemical composition of welded rails were like the one`s of parent rails, the microstructure and mechanical properties differed. The study also reported that HAZ's width impacts the mechanical properties of the welded rails.

Saita et al. (2013) study proved that wider HAZ resulted in poor mechanical properties and high residual stresses, whereas narrow HAZ resulted in good mechanical properties and low residual stresses. To improve the microstructure characterisation, mechanical properties, and residual stresses of the JIS60 rail material, post weld heat treatment was applied.

2.1.6.1.2 Effects of weld gap on the microstructure characterisation and mechanical properties

Thermite welding method is the widely used and most preferred rail welding method across the world (Yang et al., 2018). This welding method is widely preferred because it is an on-site welding method, low cost welding, easy to use and mobile, and require no electrical power (Yang et al., 2018). The weld that is produced through TW still represents discontinuities in the track structure due to variation in the microstructure characterisation and mechanical properties (Yang et al., 2018). These variations can play a significant roles in increasing the risk of weld failures under service (Yang et al., 2018).

When two rail ends are joined together during thermite weld, a welding gap should be created so as to allow rail expansion that normally happen when the rail is in service and is experiences hot conditions. Traditionally, a weld gap of 24 mm was created between two rail ends that were joined together using TW method (Webster et al., 1997). These welds were found to be experiencing plastic deformation and gradual failures (Webster et al., 1997). The failures were largely contributed by that after the rail had been in service for a long time, they then start to experience difficulties with high rolling contact loads (Webster et al., 1997).

The risk of rail weld failures can be improved by ensuring that the microstructure and mechanical properties found on the rail weld are compatible to those found on the parent rail. In rail tracks, rail welds constitute areas where the mechanical and metallurgical properties differ from the parent rail. The rail welds can at time act as starting points for rail fracture or fatigue cracks.

Mohassel et al. (2011) study investigation focused on mechanical and metallurgical properties of wide gap aluminothermic rail welds. The study reported that yield and tensile strength of wide gap welds (50 mm) were about 98% and 95% of the parent rail respectively, whereas yield and tensile strength of a narrow gap weld (25mm) were about 99% and 88% of parent rail respectively. According to the findings, tensile strength of the wide gap was significantly higher than narrow gap welds. This proved the capability of wide gap welds applications instead narrow gap welds.

Mohassel et al. (2011) study further reported that the fracture toughness mean value of wide gap and narrow welds were reported to be 75% and 60% of parent rail respectively. The mean value of wide gap weld fracture toughness were found to be lower than the average of those reported for carbon steel and higher than narrow gap welds.

Garcia et al. (2017) study investigation focused on microstructure and mechanical properties of rail aluminothermic welding. The study reported that welds with wide gap had narrow lamellar spacing between the ferrite and cementite in the pearlite, which in turns decreased the plasticity and elongation, and increased the yield strength, tensile strength and hardness when compared to welds with narrow gaps.

Table 2-9 showed preheating temperature for each weld gaps. Thate table showed that wide weld gap required low preheating tempearature, whereas narrow weld gaps required high preheating temperature.

Table 2-10 showed preheating process and the time it takes to preheat. SP1 (propane-induced air) required more time, when compared to SP2 (propane-oxygen).

Table 2-9: Preheating process and aluminothermic welding features (Garcia et al. 2017).

Type	Welding gap (mm)	Preheat temperature (°C)	Observations
NP	18±2	850-900	
SP	25±2	350-600	
SP WG	50±2	350-600	Repairs, Maintenance

Table 2-10: Preheating process and times (Garcia et al. 2017).

Process	Time
SP1 (propane-induced air)	5 minutes
SP2 (propane-oxygen)	90 seconds
SP3 (petrol-induced air)	3/5 minutes

Garcia et al. (2017) further reported that welds with wide gaps required less preheating time and temperature when compare to welds with narrow gap. (Table 2-9 and 2-10).

Chen et al. (2014) investigation focused on weld defect formation in rail thermite welds, the investigation looked at the influence of welding conditions on shrinkage cavity formation. The investigation examined the influence of preheating time on shrinkage cavity formation on 3 sample with the weld gap 25 mm, 38 mm, and 52 mm. The findings of the investigation reported that larger weld gap (52 mm) eliminated the development of shrinkage cavity, and reduced the preheating time, and the average liquid temperature significantly.

2.1.7 Rail steels and rail welds failures

Cannon et al. (2003) investigation focused on an overview of rail defects. The investigation reported that the rail failures can be divided into three groups; those that created from rail manufacturing defects, those that are originate from defects due to incorrect handling, installation, and those caused by fatigue damage.

Farhangi and Mousavizadeh (2007) study investigation reported that when contact stresses are applied by train wheels, plastic deformation will produce substantial fracturing and then realignment of hard cementite lamellae in parallel to wear surface (running surface) of the rail. Farhangi and Mousavizadeh (2007) findings were aligning with Perez and Beynon (1993).

Perez and Beynon (1993) study investigation focused on microstructure and wear resistance of pearlite rail steels. The study findings reported that softer ferrite matrix were significantly deformed, leading to a reduction in the interlamellar spacing close to contact surface. Perez and Beynon (1993) findings were argued by Daymond and Priesmeyer (2002) study investigation that focused on elastoplastic deformation of ferritic steel and cementite studied by neutron diffraction and self consistent modelling. The study by Daymond and Priesmeyer (2002) reported that plastic deformation of pearlite was as a results of the soft ferrite lamellae deformation only, at least at low plastic strains.

Perez and Beynon (1993) findings further reported that during wear process, the pearlite structure of rail steel were modified through plastic deformation within the rail-train wheels contact area, and the new structure should resist the wear and decrease the further wear rate.

The variation of the interlamellar spacing also had an important effect on fatigue fracture, which was considered a major contributing failure mechanism in reducing rail lifetime under high axle load conditions.

Gomes et al. (1997) investigation focused on effect of microstructural parameters on the mechanical properties of eutectoid rail steels. The investigation reported that finer interlamellar spacing had higher resistance to fatigue crack initiation. Saarna and Laanso (2004), and Cannon et al. (2003) study investigations argued that rail fractures caused by fatigue damage can be efficiently reduced by changing rail profile, maintenance of the rail track, and improving the rail materl properties.

Several reasons were identified for welded rail failures, those reason includes but not limited to; harh environment, continually varying load, forces and stresses to which railroads rails are subjected during service. These rail weld failures or defects are unavoidable in rail steels. The defect created during rail manufacturing such as segregations, inclusions and surface defects have harmful contributions to integrity of the welded rails (Cannon et al., 2003).

Desimone and Beretta (2006) study investigation reported that straight-break and horizontal split web (HSW) were the two main failures that the welded rail experienced (Josefson and Ringsberg 2009). Cracks in both type of failures may initiate at defects existing in the rail or may be formed in the weld zone during the welding process (Josefson and Ringsberg 2009). Investigation by Mutton and Alvarez (2004) reported that HSW was a common failure mode in both FBW and TW under heavy hual axle load conditions.

The HSW fracture was created as a crack propagates approximately parallel to rail running surface (horizontally) in the web region through the weld, before branching towards head and foot of the rail at an angle of about 45˚, which consequently led to splitting of a part of running surface of the rail.

Mousavizadeh and Farhangi (2009) study investigation focused on characterization of surface defects associated with flash butt welded pearlite rails and their contribution to overload and fatigue failures. The study reported that HSW fractures of the welded rails could happen due to both fatigue and overload as the main contributing failure mechanisms.

Tawfik et al. (2008) investigation reported that the rail thermite welds were susceptible to HSW failures, especially in the middle of the web region, this was contributed by that when the high levels of tensile residual stresses in the web region combined with those induced from high axle cylic torsional loading of the rail web, initiation and propagation of fatigue cracks could happen from pre-existing defects.

Mutton and Alverez (2004) investigation reported that straight-break failure was more familiar in rails that were welded by thermite welding. The investigation further revealed that in straight-break failure, the crack propagates vertically along the transvesre plane, either at the weld centreline or at the edge of the weld collar.

Mutton and Alverez (2004) study further showed that majority of the straight-break failures initiated at the centreline of the weld were associated with centreline shrinkage cavity defects in the foot region of the rail thermite welds.

Salehi et al. (2011) study investigation focused on multi-axle fatigue analysis of aluminothermic rail welds under high axle load conditions. The study reported that initiation and propagation of straight-break failure mode cracks were strongly affected by the thermal stresses longitudinally developed in the welded rails due to the change in ambient temperatures, specifically the tensile stresses induced in colder months.

The longitudinal tensile stresses were induced in the web region of the rail weld as a result of welding processes, and bending stresses created due to influence of wheel-rail contacts. This played a huge role in increasing the risk of the brittle straight-break failure of the welded rail.

Monsouri et al. (2004) investigation focused on effect of local induction heat treatment on the induced residual stresses in the web region of a welded rail. The study reported that the possibility of weld failure in welded rails were minimized by reducing the amount of tensile residual stresses in the web region, through modification of welding conditions, or application of post weld heat treatment.

2.2 Chapter summary

Based on the available literature survey, there was research knowledge gap on analysing the microstructure, mechanical properties, and wear resistance of TW rail steel when weld gap was increased above 24 mm. However, there was vast published research pertaining to the development and characterisation of a TW R260-60E1 pearlite rail steel with a weld gap 24 mm.

Literature revealed that the microstructure of the TW pearlite rail largely depends on the heat input and the cooling rate of the rail welded joint. Slower cooling rate can be achieved by preheating the rail ends before applying TW; this method also supports the formation of pearlite and helps to avoid the formation of martensite and bainite. In contrast, when a fast-cooling rate was achieved, the weld metal mainly consisted of intragranular Widmanstätten ferrite with isolated grains of pearlite, together with ferrite at the prior austenite grain boundaries.

Literature further showed that the microstructure of intragranular Widmanstätten ferrite in standard thermite weld metal was also associated with segregated bands parallel and close to

the fusion zone/HAZ interface. Those bands consisted of pearlite with intragranular Widmanstätten ferrite, rich in aluminium and somewhat in manganese. Myers et al (1982) showed that the bands were harder than the non-segregated regions of the weld metal, hence the peak hardness in the HAZ was always in the region close to the fusion zone.

Higher hardness was mostly preferred because it increased resistance to fatigue and deformation (Myers et al.,1982). Hard welds hold up more under increasingly hard axle loadings and help prevent rail head depressions at the weld (Myers et al.,1982).

Mohassel et al. (2013) proposed a thermal model that included weld gap as one parameter to improve rail steel mechanical properties. The results suggested that increasing the weld gap leads to an increase in temperature distribution points, improving the rail steel's mechanical properties.

The projection informed by literature showed that even though the chemical composition of welded rails were almost similar to that of parent rails, the microstructure and mechanical properties were different. Literature further noticed that the HAZ's width impacts the mechanical properties of the welded rails.

Literature proved that wider HAZ show poor mechanical properties and high residual stresses, whereas narrow HAZ show good mechanical properties and low residual stresses. To improve the microstructure characterisation, mechanical properties, and residual stresses, a narrow HAZ should be achieved. Therefore, by increasing the weld gap to 40 mm and above, we would be able to see if a narrow or wider HAZ would be achieved.

3. CHAPTER 3

3.1 Experimental work

3.1.1 Introduction

The experimental approach that was adopted to achieve the objectives of this research entails the following: material sample and preparation, welding process, NDT on the welds, microstructure characterisation, hardness testing, tensile testing, Charpy impact testing, and wear testing, as per the flow chart in Figure 3-1. The experimental methodology of each test is described in sections 3.1.2 – 3.1.10

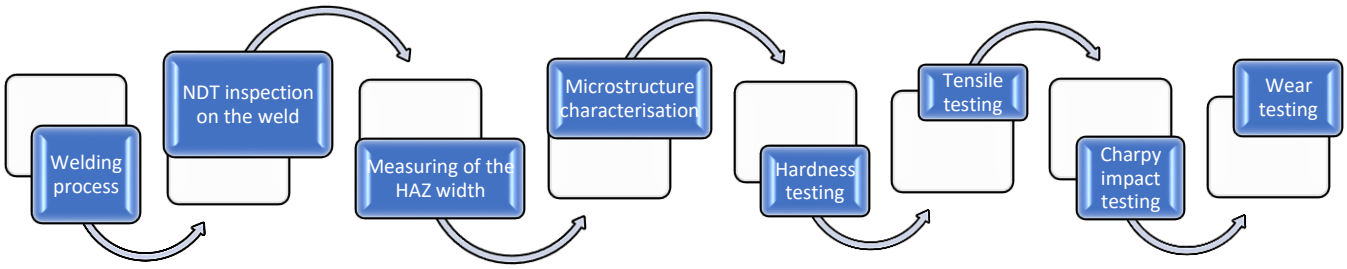


Figure 3-1: Flow chart illustrating the experimental methodology that was followed to achieve the research objective.

3.1.2 Materials

The materials used in this study were 60E1 thermite welded (TW) pearlitic rail steels of grade R260 with a weight of 60 kg/m and a weld gap of 40 mm and 50 mm, respectively. Table 3-1 shows the chemical composition of the R260-60E1 pearlite rail steels, specification chemical requirement for grade R260 (EN13674-1:2018) and the thermite weld metal. Spark chemistry analysis was used to confirm the chemical composition of the pearlite rail steel (R260-60E1) and the weld metal.

Table 3-1: Chemical composition (%) for pearlitic rail steels and thermite weld.

Material	Pearlitic steel (R260-60E1)	R260-60E1 (EN13674-1 Specification)	Weld Metal (TW R260-60E1)
C [%]	0.756	0.60 – 0.82	0.568
Si [%]	0.312	0.13 – 0.60	0.571
Mn [%]	1.160	0.65 – 1.25	1.020
Cr [%]	0.033	0.15 (max)	0.103
V [%]	-	-	0.130
Ni [%]	0.010	-	0.037
P [%]	0.023	0.030 (max)	0.033
Cu [%]	0.019	-	0.034
S [%]	0.023	0.030 (max)	0.020
Al [%]	0.002	-	0.055
Mo [%]	0.005	-	0.019
Fe [%]	Balance	Balance	Balance

3.1.3 Thermite welding of rail steel

The two sets of rail ends were cut in square. Each set was carefully aligned and fixed with a gap that was set to be 40 mm and 50 mm between each set respectively. The 40 mm and 50 mm gap was given for contraction allowance. The cut face were cleaned with kerosene oil and wire brush to remove rust, dust, or greasy material. Long steel straightedge was used to align the running edge of the rail head. The rail ends were preheated to 850 ℃ by a flame torch.

The preheating of the rail ends was done in order to wash away the poured molten metal on the rail ends, otherwise, the molten metal may end up solidifying immediately when it get in contact with cold rail end. It is vital to preheat the rail ends in order to provide a slower cooling rate, as the steel has a carbon equivalent of more than 0.42 and therefore the formation of martensite and bainite at a higher cooling rate must be avoided.

A set of prefabricated moulds of the broad gauge rail section were selected and examined for suitability. The rail profile of the mould was checked by placing the mould against the side of the rail to be welded. The mould was placed in the mould shoe. The placement of the mould was made to be central over the gap between the two rail ends. Small adjustments were made on the mould profile by rubbing the mould gently against the sides of the rail. A slag bowl was

attached to the mould shoe to collect the overflowing slag and molten metal during pouring. The mould is preheated using a welding torch. Preheating is done to dry the mould thoroughly and to bring the parts to be welded at desired temperature of 900 ℃.

Thermite reaction which was composed of an iron alloy powder mixture of an oxidized iron, metallic aluminium and other alloying additives such as ferromanganese were used to join the two rail ends together. The mixed reaction was then poured into a crucible that was placed over a ceramic mould and ignited using an ignition agent.

The reaction started by igniting the main aluminothermic charge, this lasted for about 15-35 seconds. When the reaction was completed, molten steel and aluminium oxide slag were produced in a molten state. These two were separated in a crucible by the specific gravity difference, with the aluminium slag floating to the upper part of the crucible.

After removing the slag, the molten steel (at a temperature above 2000 ℃) was discharged into a ceramic mould, which exposed the rail end to superheated steel, which welded the two rail ends together, after which the tapping and solidification process took place. This process took approximately 4 minutes, and it was followed by trimming process where excess metal around the rail were sheared off and removed by grinding.

The weld joints with the weld gap of 40 mm and 50 mm were prepared using the welding parameters of gas pressure (oxygen and propane) (KPa), duration (min), and temperature (℃). The parameters were kept constant for both the weld gap of 40 mm and 50 mm samples as shown in Table 3-2. Employing the Thermite welding technique, the weld preparation adhered to the guidelines stipulated in the EN 14730-1:2017 European welding standard.

Table 3-2: Oxy propane preheating conditions used for the thermite welded rail samples.

Welding gap (mm)	Gas Pressure (KPa)		Duration (min)	Temperature (℃)
	Oxygen	Propane		
40	200	60	6	~950
50	200	60	6	~950

3.1.4 Non-Destructive Testing

Two NDT methods that were carried out to detect surface and subsurface defects on the welded and un-welded sections of the rail samples were visual inspection (surface) and X-ray

inspection (radiograph) (subsurface). The X-ray inspection was performed according to ISO 10675 (2016) standard.

The X-ray technique (Radiograph) was carried out using a Dong 300 kV X-ray machine. The film and testing parameters that were used were 2D and 1000 mm, respectively. Source to film distance was 100 mm focal spot and 210 kV, 5m amps in 5 seconds. The testing techniques that were used were single wall, single image for rail web, and single wall and double image for foot/base.

3.1.5 Sectioning of the thermite welded rails

Wire-Electro-Discharge machining (EDM) was used to cut the thermite welded rails into manangable sample pieces. The wire EDM cuts were performed using low voltage (16 V) and low speed (0.25 mm/min) settings.

The cuts were performed through the cross section of the parent rail and the rail weld. This was carried out from the head toward the foot region of the rail to produce two halves with a weld centre. The two halves were further sectioned in the longitudinal direction from the head toward the foot region of the rail.

3.1.6 Metallographic examination

3.1.6.1 Microstructure characterisation

The TW R260-60E1 pearlitic steel microstructural characterisation was studied in the laboratory using optical microscopy (OM) and scanning electron microscopy (SEM). The different phases were identified by X-ray diffraction (XRD) techniques.Characterisation was done on the samples with the weld gap of 40 mm and 50 mm.

The samples were sectioned in the longitudinally direction across the head, web, and foot region. The weld, HAZ, and parent rail were obtained on each sample that was sectioned on the respecteve regions. Sample preparation was achieved by mounting the weld, HAZ and parent metal sample from the head, web, and foot regions in polyester resin for handling. After mounting, the samples were prepared for metallography by the following three steps.

1. Grinding: An electrically powered rotary discs fitted abrasive silicon carbide papers of different grits was utilized to remove the scratches introduced by the grinding process. The grinding process was done sequentially by using coarse grinding paper (80, 120,

and 240 grit) followed by finer grinding that was achieved by using 400, 500, 800, and 1200 grit papers, respectively.

2. Mechanical polishing: Diamond particle pastes were used to remove the new finer scratches introduced by the grinding step. Polishing was achieved by using 6, 3 and 1µm paste sequentially. The polishing was applied on special clothes fixed on electrically powered rotary discs.
3. Etching: Nital (5% HNO_3 + 95% Methanol) was used as an etchant to reveal the structural characteristics of the metal at microscopic level. The etched sample was cleaned with alcohol to prepare the surface for metallographic examination. The etched samples exposed the extent of the HAZ to be measured for all regions (refer to section 3.1.7).

3.1.6.1.1 Microstructural analysis

The optical microscope (OM) and the scanning electron microscope (SEM) were used to characterise the microstructure at different magnifications.

(a) A Zeiss optical microscope (OM) was used to define the phase constituents, metal microstructure and topography of different regions on the prepared specimen surface across the weld, HAZ, and parent metal for the head, region, and foot region, under 500 and 1000 magnifications.

(b) A scanning electron microscope (SEM) was used to determine the composition of the phases present in the matrix. Scanning electron microscope (SEM) imaging was performed using secondary electrons (SE) and backscattered electrons (BSE) in a JEOL JSM 7001F instrument fitted with an X-max 20 mm^2 energy dispersive spectrometer (EDS). ASTM E986-04 standard was used to conduct SEM.

3.1.6.1.2 Phase identification

An X-pert PRO diffractometer machine was used to perform an X-ray diffraction (XRD) technique to quantify the phases on the weld, HAZ and parent of the TW R260-60E1 pearlitic rail steel. The power source used was Fe filtered CuKα radiation, with a wavelength of 0.78 Å. The samples were scanned from 10º to 90º degrees 2θ angular range, with 0.026º angle step. The phases were identified by using Rietveld refinement by X`Pert HighScore software. The current and voltage settings for safe XRD output were 45 KV and 40 mA, respectively.

3.1.7 Measuring of Heat Affected Zone Width

A ruler was used to measure the HAZ width on the TW rail steel samples. This method was applied to both samples with 40 mm and 50 mm welding gaps. The measurements for both samples were conducted on the head, web and foot regions.

3.1.8 Hardness testing

A Vickers diamond pyramid indenter fitted to an Emco test durascan hardness testing machine with 10 kg load was used to obtain macro-hardness results for TW R260-60E1 pearlitic steel with a welding gap of 40 mm and 50 mm, respectively. The hardness measurements were taken on the head, web, and foot regions of each sample. The distribution of the measurement points was 2 mm intervals from the weld centre line to the parent rail on each region.

The basis of the Vickers macro hardness measurement consists of indentation of the samples by a square based diamond pyramid indenter, which comprised of opposite faces with an angle of 136º between them. The diamond is pressed onto the surface of the material by applying a load of 10 kg. The Vickers (HV) number is then calculated using the following formula:

Equation 3-1: Hardness calculation

$$HV = 1.854\frac{F}{D^2}$$

Where F is the applied load (measured in kilograms-force) and D^2 is the area of the indentation (measured in square millimetres). To ensure that the indentation did not deform the surrounding material and alter its properties, the hardness testing adhered to the guidelines stipulated in the EN ISO 6507-1: 2005 European international stundard. The testing was conducted at room temperature.

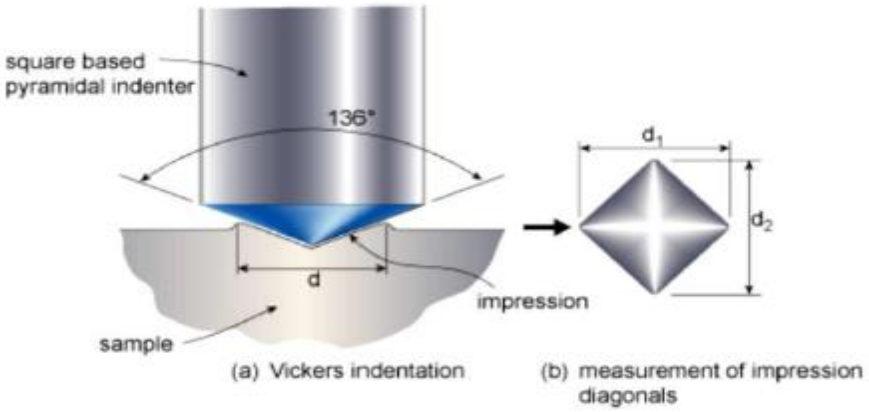


Figure 3-2: Schematic illustration of Vickers hardness test (Struers Ensuring Certainty, 2015).

3.1.9 Mechanical testing

The TW R260-60E1 pearlitic rail steels with 40 mm and 50 mm welding gaps were sectioned in preparation for mechanical testing. Tensile testing and impact charpy testing were performed to evaluate the strength and toughness of the material within the weld, heat-affected zone (HAZ), and parent rail.

3.1.9.1 Tensile test

The Tinius Olsen tensile testing machine was used to conduct the test. The weld, HAZ and parent material from the head and web region of the TW R260-60E1 pearlitic rail steels were sampled and prepared according to EN 13674-1: 2017 specification. The testing was conducted at room temperature. Table 3.3 shows that the grip section was 7 mm for all samples, whereas the distance between shoulders was different for each sample :

Table 3-3: Rail samples dimensions for tensile testing.

Rail samples	Grip section (mm)	Distance between shoulders
Web - Weld	7	22
Web - HAZ	7	22
Head - Weld	7	38
Head - HAZ	7	38
Head - Parent	7	38

3.1.9.2 Charpy Impact testing

The Charpy impact test, also known as the Charpy V-notch test, is a material toughness test by high strain rate testing that involves striking and breaking a standard notched specimen with a controlled weight pendulum swung from a set height (ASTM: A370 – 97a, 1997). The Charpy impact test assists in measuring the amount of energy absorbed by the material specimen during fracture.

The amount of energy absorbed during fracture is recorded, providing the tested material's toughness level. The test reveals whether the material can be classified as brittle or ductile. Brittle materials absorb a small amount of energy during impact testing, whereas ductile materials absorb a substantial amount of energy (ASTM: A370 – 97a, 1997).

The Tinius Olsen impact testing machine was used to conduct the test on the weld, HAZ, parent material of the head and web region of the rail metal for the TW R260-60E1 pearlitic rail steel samples. Impact tests were carried out in accordance with ASTM standard test methods for notched bar impact testing of metallic material (ASTM: E23 – 12c, 2016). Each sample followed standard V-notched Charpy impact testing procedure, with sample size of 10 × 10 × 55 mm. The impact test temperature was kept at room temperature for all samples.

3.1.10 Wear testing

The wear testing method that was used for this investigation was a ball on the disc. This method was used to perform a tribological characterization on TW R260-60E1 pearlitic rail steels. A total of 4 samples with 20 × 20 mm dimensions were extracted from the head region (parent metal and HAZ) and web region (HAZ and weld metal). The ASTM G99 standard was used as the guide for sample dimension and test procedure.

The material used for this test was the 6 mm diameter alumina (L203) balls with a high hardness of 450-500 HV_{10}. The testing parameters noted in Table 3-4 were conducted on a 100 m distance set for 1000 sec. After the abrasive wear test, the profile of the worn area was measured by Mitutoyo SJ-400 profilometer. The measured profile data was imported to Origin Lab software. Finally, the wear volume was obtained by measuring the worn area on the tested samples. The Archard equation was used to calculate the specific wear rate (k, mm^3/Nm):

Equation 3-2: Archard equation

$$K = \frac{V}{(XL)}$$

Where, V is the wear volume (mm^3), X is the sliding distance (m), and L is the normal load (N).

Table 3-4: Abrasive wear testing parameters.

Parameters	Conditions
Normal load	5N
Sliding velocity	0.025 m/s
Wear radius	3 mm
Ball hardness	450 – 500 HV_{10}

3.11 Chapter Summary

The experimental procedure was achieved by conducting a chemical analysis on the parent rail material to confirm the chemical composition of the R260-60E1 pearlitic rail steel material. The two rail ends of this material were welded together through a thermite welding method according to EN 14730-1:2017 European welding standards. Each sample half revealed three regions (head, web and foot) and each region had different weldment zones (weld metal (WM), heat affected zone (HAZ), and parent metal (PM)). Vsual examination (surface) and radiograph analysis (subsurface) were further performed on both TW R260-60E1 pearlitic rail steel samples. All the sampling and preparation for the examinations were performed successfully according to the standards.HAZ width measuments, metallographic characterisation (OP, SEM, and XRD), hardness distribution, mechanical properties (tensile strength and charpy impact toughness) and wear resistance behaviour were all assessed on the three regions across all the different weldment zones for both TW R260-60E1 pearlitic rail steel samples.

4. CHAPTER 4

4.1 Results and discussion

4.1.1 Introduction

This chapter presents the results and discussion of all tests, analyses and characterization that were carried out. The TW R260-60E1 pearlite rail steel was evaluated to determine the effect on microstructure, heat affected zone (HAZ) width, mechanical properties, and wear properties when the weld gap size was set to 40 mm and 50 mm respectively. The results and discussion are presented in sections 4.1.2 – 4.1.7.

Section 4.1.2 discusses the non-destructive testing (NDT). Heat affected zone (HAZ) width measurements results are presented in section 4.1.3. The microstructure characterisation which is subdivided into optical microscope, scanning electron microscope and X-ray diffraction (XRD) is addressed in section 4.1.4. Sections 4.1.5-4.1.7 presents the hardness distribution profile, mechanical and wear testing.

4.1.2 Non-destructive testing

Two non-destructive testing techniques were used to examine the soundness of the thermite welded rail of two samples with weld gap of 40 mm and 50 mm. The tests included the visual examination, where the surface of the material was evaluated, and the X-ray technique (radiography), where the subsurface of the material was assessed for any unwanted defects.

4.1.2.1 Visual examination

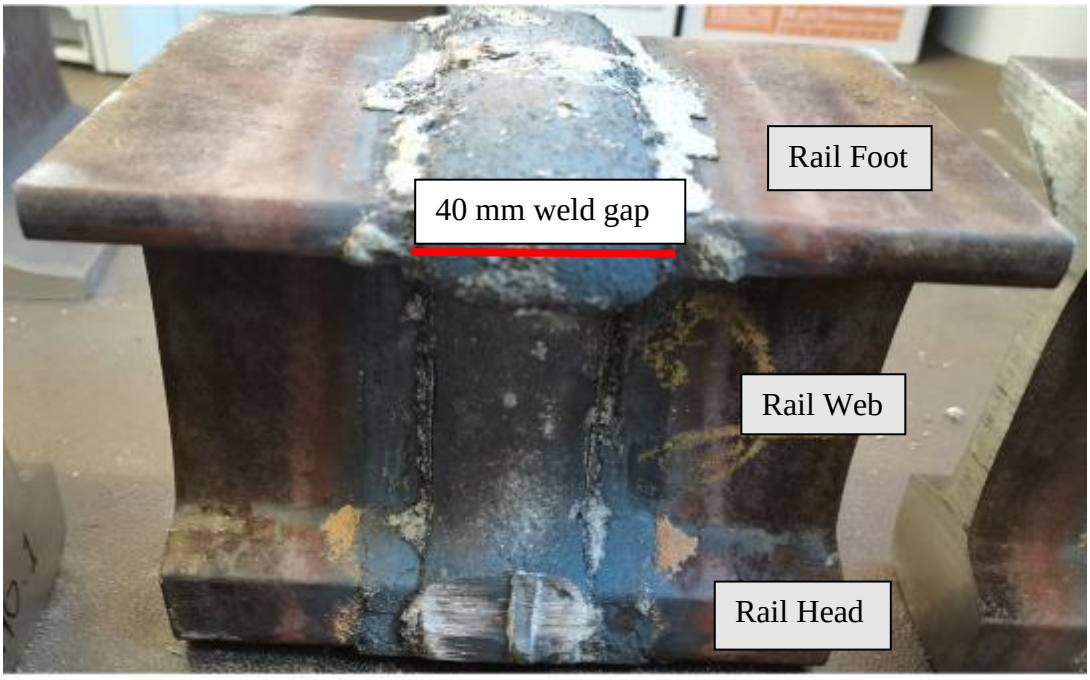


Figure 4-1: Thermite welded rail with a 40mm weld gap.

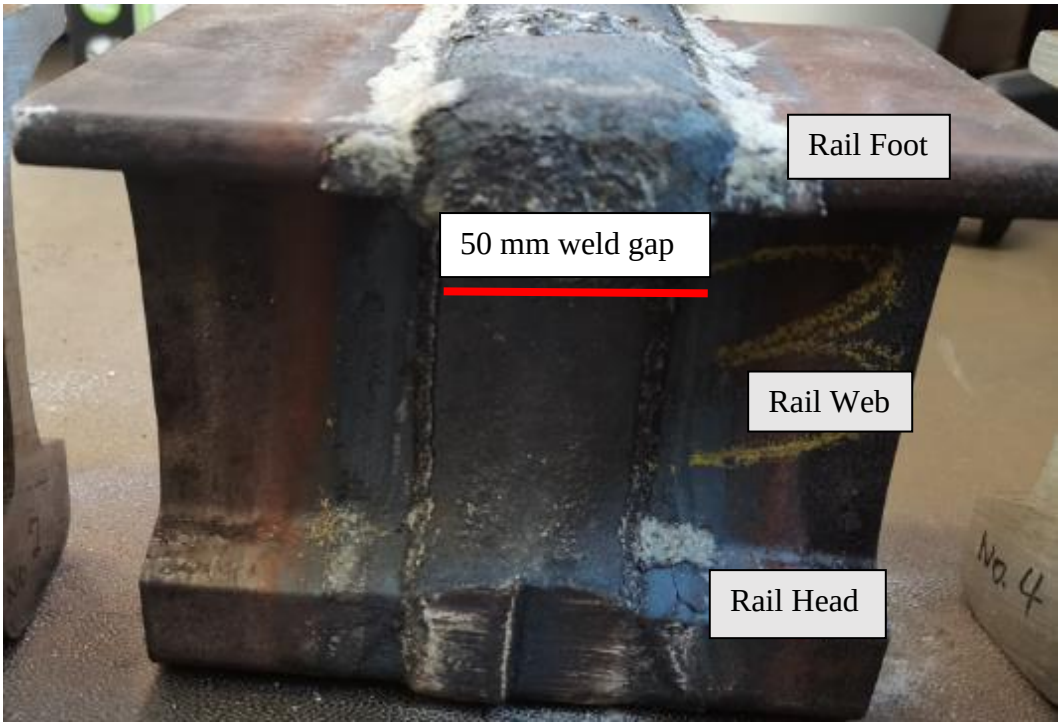


Figure 4-2: Thermite welded rail with a 50mm weld gap.

Figures 4-1 and 4-2 showed a thermite welded rail steel with a weld gap of 40 mm and 50 mm, respectively. The visual examination of both samples showed no noticeable defect on the parent and weld surface of the rail.

4.1.2.2 X-ray technique (Radiography)

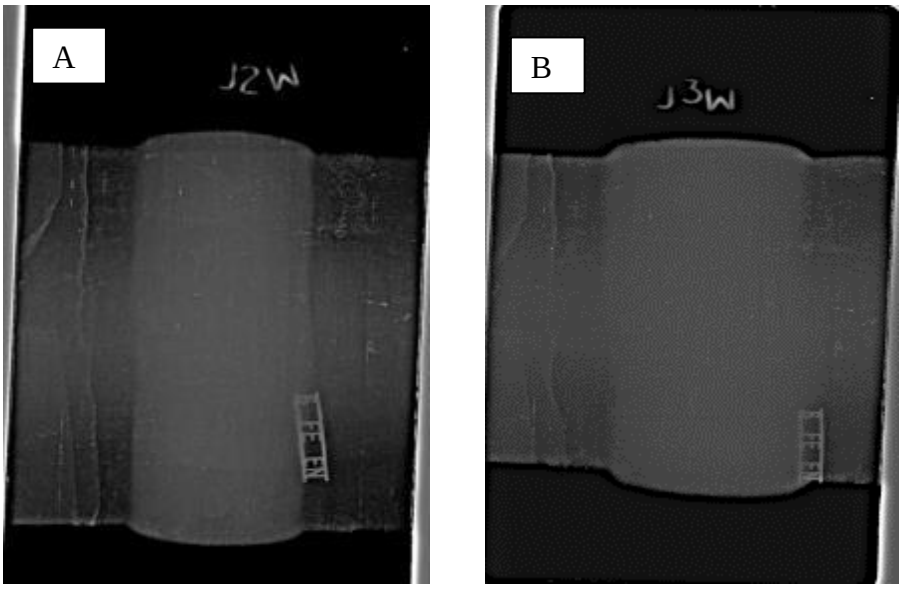


Figure 4-3: X-ray images showing head-foot region of a thermite welded rail with a weld gap of (a) 40mm and (b) 50 mm.

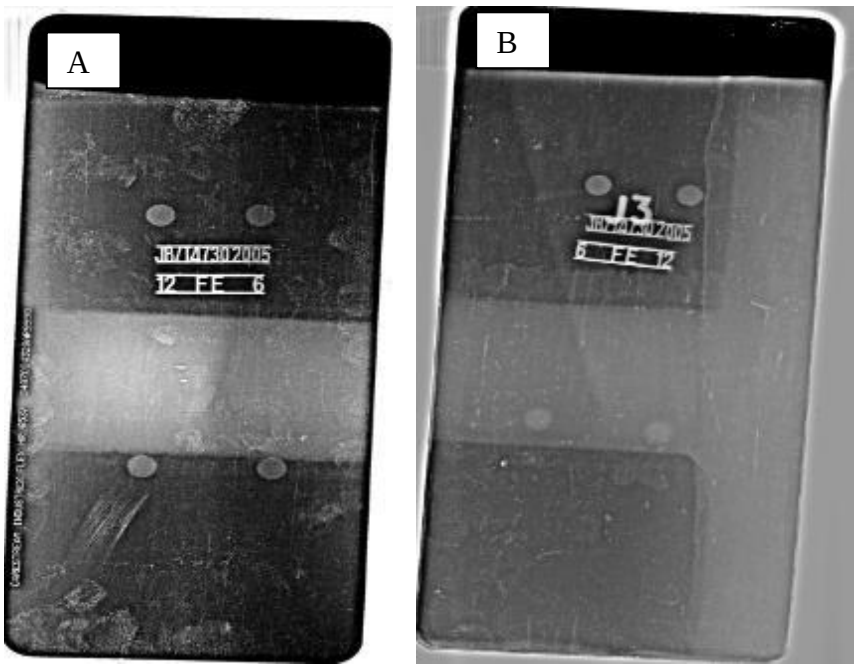


Figure 4-4: X-ray images showing the web region of a thermite welded rail with a weld gap: (a) 40 mm and (b) 50 mm.

Figures 4-3 and 4-4 showed X-ray images with results for the head-foot and web regions of the R260-60E1 TW pearlitic rail steels with a weld gap of (a) 40 mm and (b) 50 mm. The results showed no noticeable or recordable weld subsurface indications of defects such as pores and internal cracks. The absence of relevant recordable or noticeable indications on the weld

provided the assurance of the weld integrity of the joints and eliminated the possibility of weld defects that could have a detrimental effect on the weld performance. Both welds were acceptable in accordance with the NDT acceptance criteria specification (EN 14730-1,2017).

4.1.3 HAZ width measurements

The wire electro-discharge machine (wire EDM) was used to cut the samples in the longitudinal direction, as shown in Figures 4-5 and 4-6. The two longitudinal halves of each sample showed weld centre, the area where two rail ends were joined. Figures 4-5 and 4-6 further showed visible extent of the HAZ, weld, and parent rail samples on all rail regions (head, web, and foot).

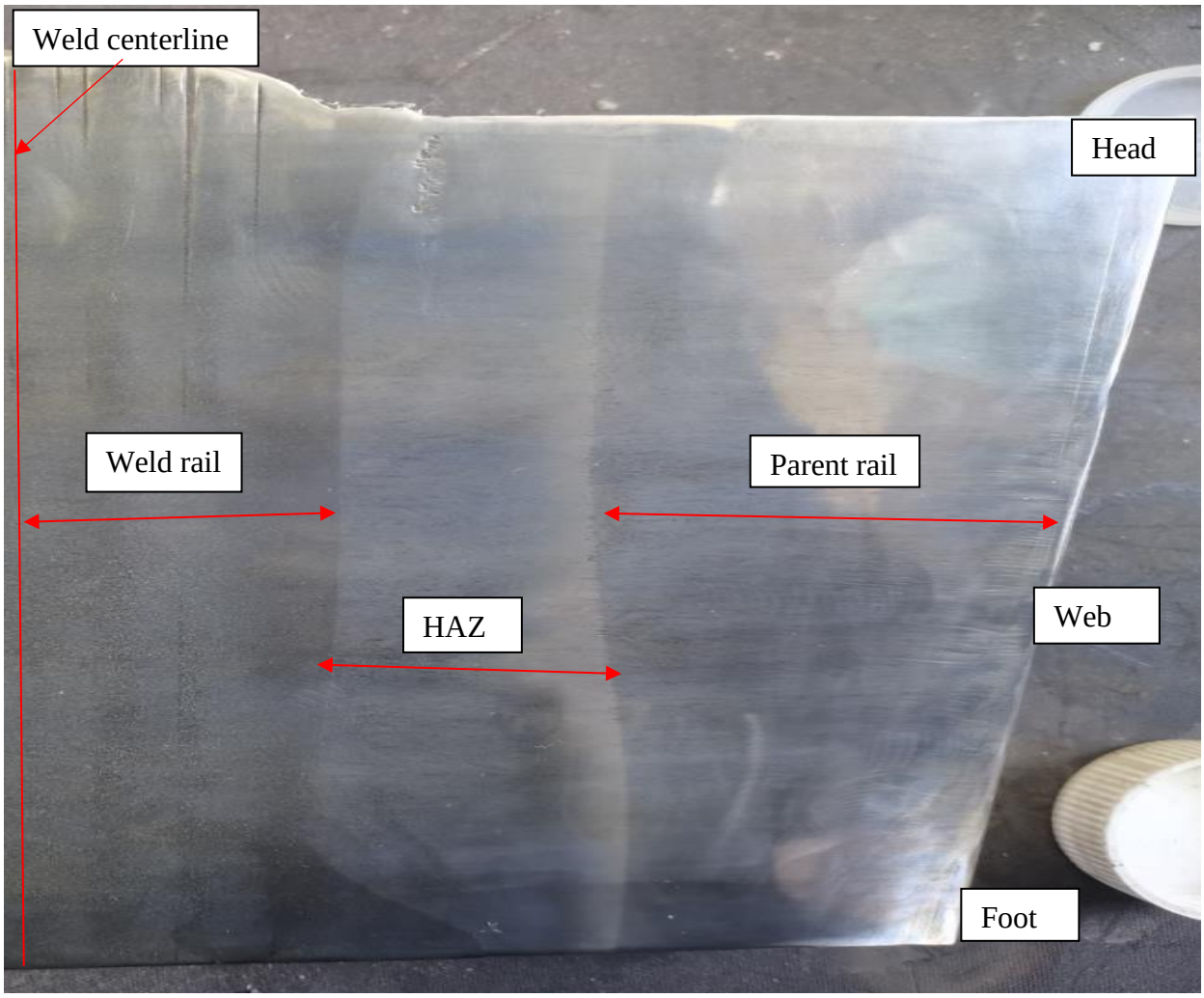


Figure 4-5: Macrograph of the ground, mechanically polished and 5% nital etched sample, extracted from the longitudinal section of the thermite welded rail. This sampling represents both the 40mm and 50mm weld gap samples.

The thermite welding of R260-60E1 pearlitic rail steels took place on the head, web, and foot regions, where molten metal was poured between two rail ends, each with a weld gap of 40

mm and 50 mm as per the objectives of this research. The weld zone was achieved by solidification of molten metal. The parent rail did not experience any melting and high heat exposure. Whereas heat affected zone (HAZ) did not experience any melting, but went through phase transformation at high temperature.

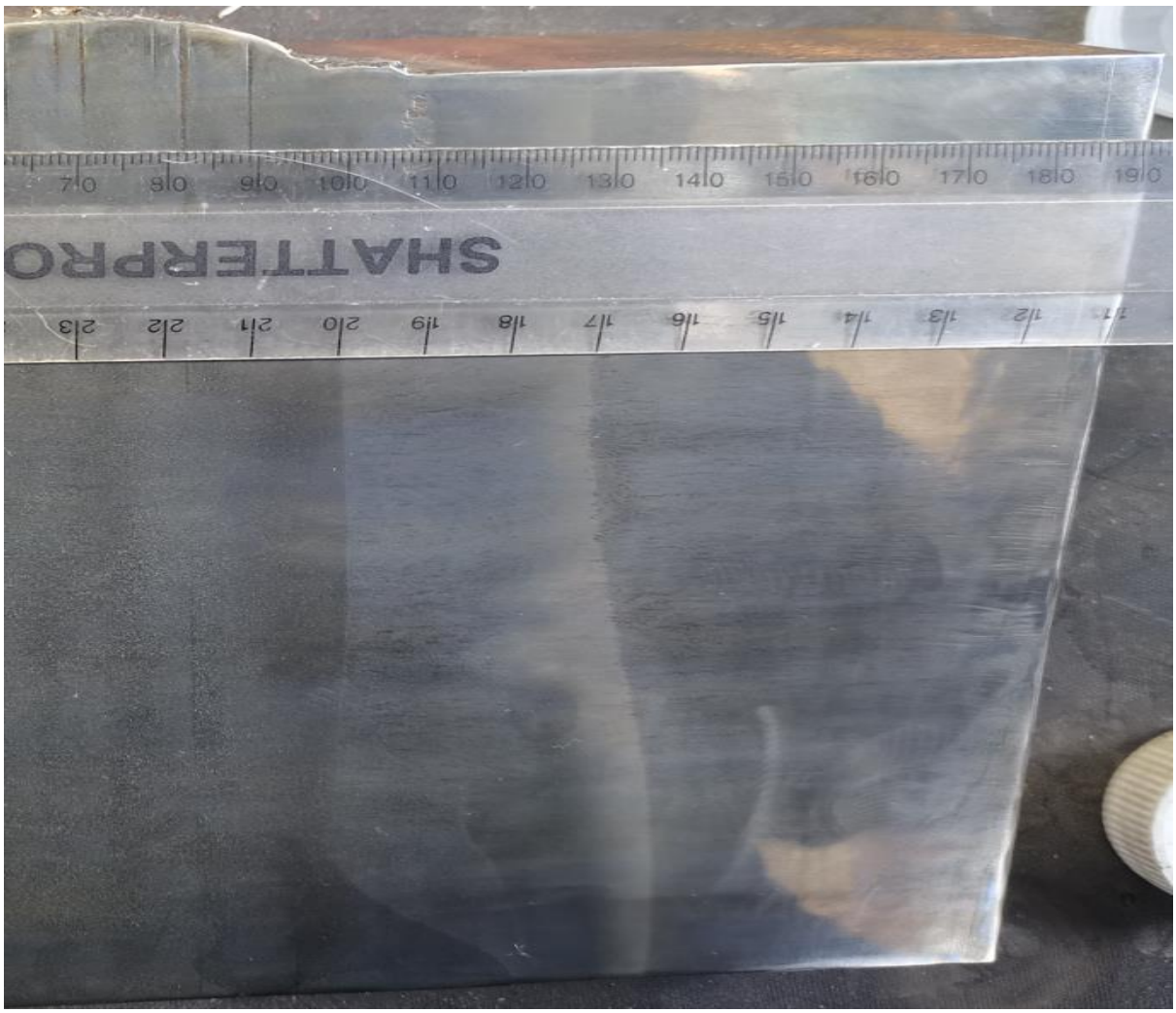


Figure 4-6: Macrograph of the ground, mechanically polished and etched with 5% nital. The sample is extracted from the longitudinal section of the thermite welded rail with a 40 mm weld gap.

A ruler was used to measure the HAZ width profile as a function of height across all three regions of TW R260-60E1 pearlitic rail steels. The HAZ was calculated from the foot to the head region with an interval of 10 mm on each region. A study by Mohassel et al. (2013) concluded that the width of the HAZ largely depends on the width of the weld gap. This relationship was confirmed by the fact that a wide weld gap yielded a narrow HAZ, whereas narrow weld gap yielded a wide HAZ.

A wider HAZ not only leads to poor mechanical properties, but it also results in less steady hardness profile across the weld (Meade,1999). Less steady hardness profile increases the lack of hardness or soft spots across the material. These soft spots can lead to weld fatigue, deformation, and premature failures (Meade,1999).

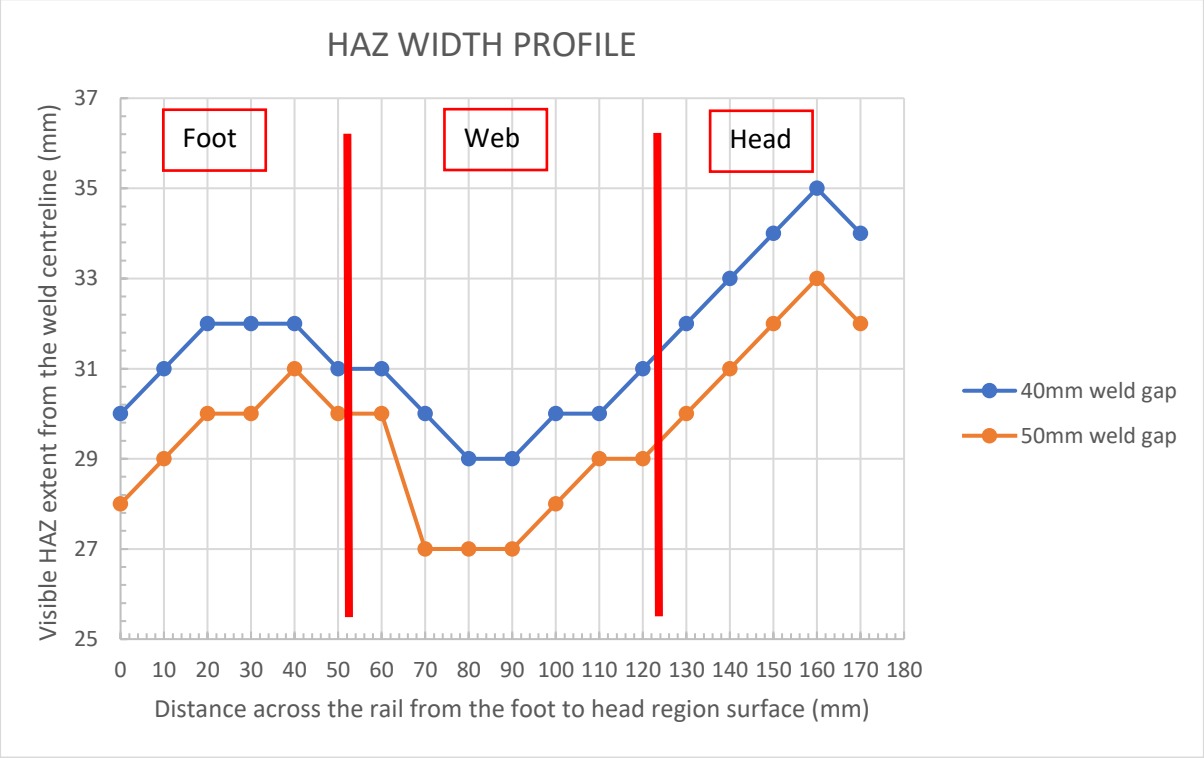


Figure 4-7: HAZ width measurements for the head, web, and foot region along the rail height of the thermite welded rail for the 40- and 50-mm weld gaps.

Figure 4-7 showed an extent of the HAZ in TW R260-60E1 pearlitic rail steels for both samples with the weld gap size of 40 mm and 50 mm. The results showed that the weld gap was inversely proportional to the HAZ width. The sample with a weld gap size of 50 mm had a narrow HAZ width when compared to the sample with a weld gap size of 40 mm. The HAZ width on both samples was noted to be narrow on the web region when compared to the head and foot region as indicated on Figure 4-7.

The HAZ was made up of four main zones, namely: coarse grain HAZ (CGHAZ), fine grail HAZ (FGHAZ), inter-critical HAZ (ICHAZ), and sub critical HAZ (SCHAZ). The study by Meade (1999) suggested that the decrease in the HAZ width affected the width of the ICHAZ, making it narrower. ICHAZ is known to have soft hardness which resulted because of the presence of spheroidized pearlite. The narrower the ICHAZ, the better the mechanical properties and wear resistance on the HAZ (Meade, 1999).

The head region had a relatively wider HAZ width. The wide HAZ width on this region indicated that heat was retained for a longer period, resulting in a slower cooling rate (Gomes et al., 1997). The slow cooling rate produces a HAZ that has a relatively wider ICHAZ, which contain spheroidized pearlite (Meade 1999).

The findings of this investigation showed that the web region had a surface area to volume ratio that was higher than the surface area to volume ratio of the head and foot regions of rail as shown on Table 2-3 (Liberty OneSteel., 2017). The high surface area to volume ratio on the web region indicated that heat dissipated during the cooling in the web region was higher, whereas the head and foot region kept the heat from the molten material for longer time and cooled more slowly, especially in the interior of these regions. These findings were consistent with the findings presented by Webster et al. (1997) in a study on a BS11 rail thermite weld.

The narrow HAZ width on the web region was as a result of a bigger surface area to volume ratio, and fast cooling rate when compared to the other two regions. The findings showed that surface area to volume ratio was inversely proportional to the HAZ width. As the surface area to volume ratio increased, HAZ width decreased (Mansouri and Monshi., 2004).

An increase in the weld gap size affects the regions of rail weld (head, web, and foot region) surface area to volume ratio which subsequently affect the HAZ width. As surface area to volume ratio increased, heat dissipation also increased. Thereafter a faster cooling rate was obtained (Mansouri and Monshi., 2004). A fast-cooling rate yields a narrow HAZ width, whereas a slow cooling rate yields a wider HAZ width (Gomes et al., 1997). The sample with a weld gap size of 50 mm had a narrow HAZ when compared to sample with weld gap size of 40 mm.

The narrow HAZ width on the sample with a weld gap size of 50 mm indicated that heat was dissipated at a faster rate (Gomes et al., 1997). The study by Meade (1999) reported that the HAZ does not experience any melting but undergoes phase transformation where δ-Fe transforms to γ-Fe, followed by a transformation change from γ-Fe to α-Fe.

Webster et al. (1997) conducted a study on S49 grade rail sample with a weld gap of 24 mm. The findings reported that HAZ width varied from 41 mm to 47 mm along the height of the rail. The results obtained in this research study showed that the sample with the weld gap of 40 mm had a measured HAZ width that varied from 29 mm to 35 mm, whereas the sample with a weld gap of 50 mm had a measured HAZ width that varied from 27 mm to 33 mm. The results

also showed that the measured minimum HAZ width on the web region for sample with weld gap of 40 mm and 50 mm were 29 mm and 27 mm respectively.

Webster et al. (1997) and Mohassel et al. (2013) reported that the width of the HAZ largely depended on the width of the weld gap. These findings were aligned with the results obtained in this investigation. The larger the weld gap, the narrower the HAZ width, and the smaller the weld gap, the wider the HAZ width (Mansouri and Monshi., 2004). Regions with bigger surface area to volume ratio had narrow HAZ when compared to regions with a smaller surface area to volume ratio (Mansouri and Monshi., 2004).

4.1.4 Microstructure characterisation

4.1.4.1 Optical microscope and scanning electron microscope.

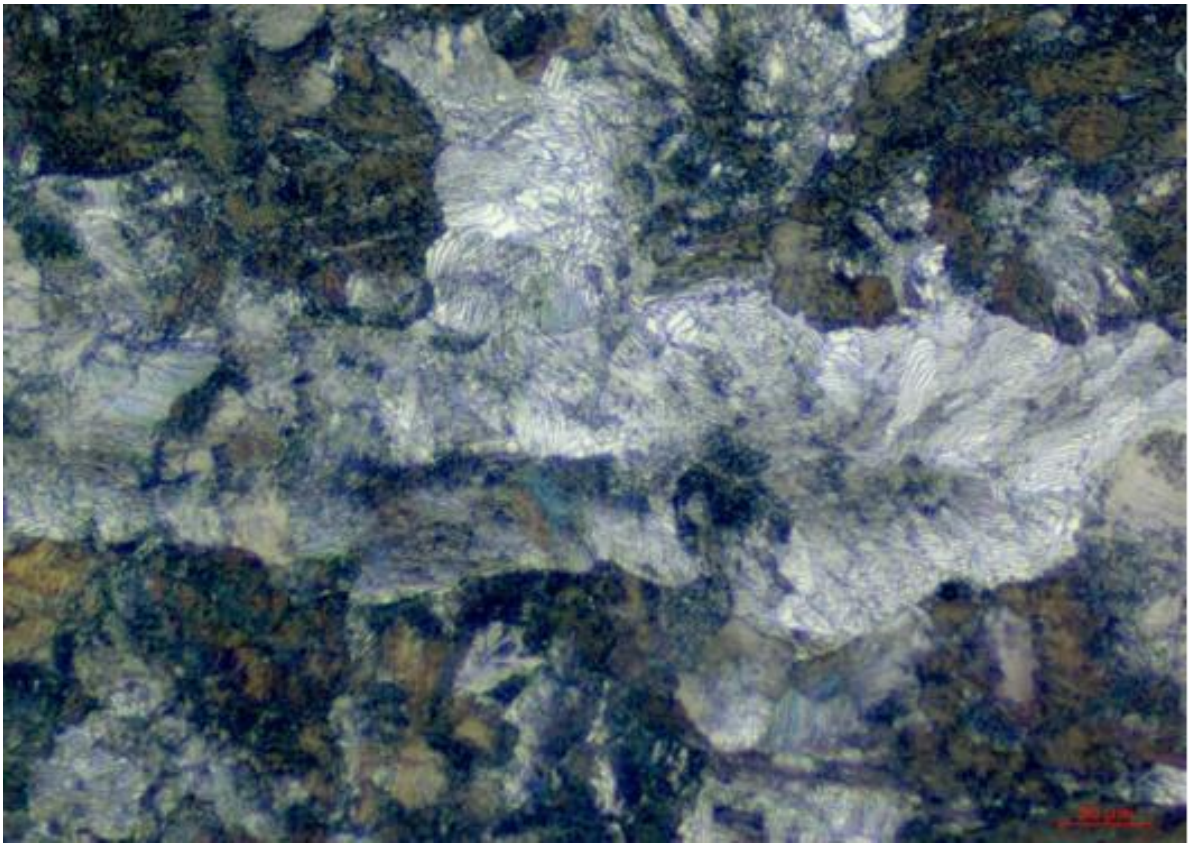


Figure 4-8: Microstructure of the R260-60E1 parent rail steel showing the pearlitic structure [Etched in 5% nital, 500x magnification].

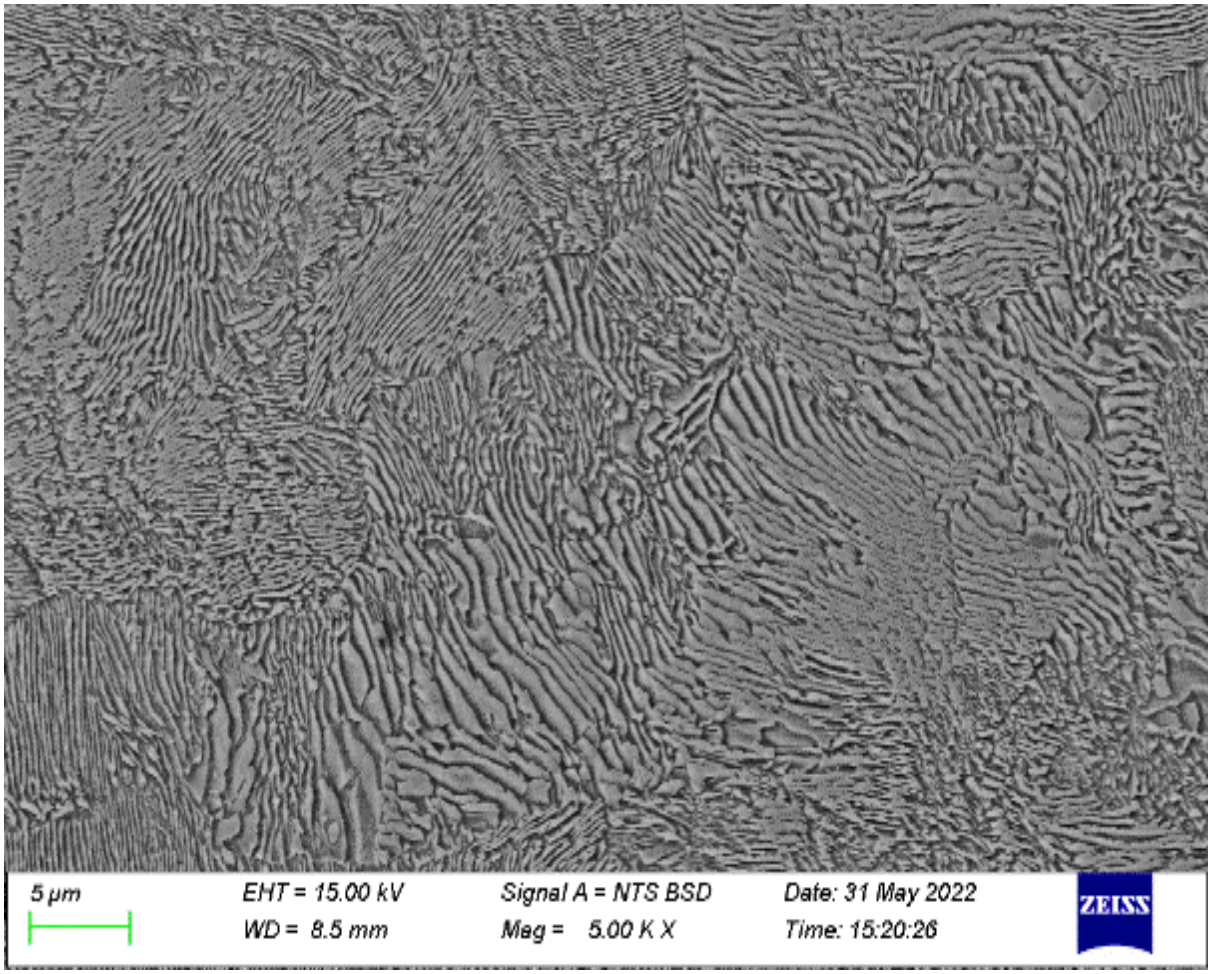


Figure 4-9: SEM image of a R260-60E1 parent rail steel showing pearlite structures at higher 5000x magnification.

The chemical composition analysis of R260-60E1 pearlitic rail steel joined by TW process presented in Table 3-1 showed that the element content of R260-60E1 rail grade was most commonly used in UK and Europe rail networks. Figure 4-8 (OP) and 4-9 (SEM) showed that the microstructure of the R260-60E1 rail was a pearlitic steel structure, consisting of alternating lamellae of ferrite and cementite.

Table 3-1 showed that the carbon content (0.756 wt%) of this rail was very close to that of eutectoid steel (0.80 wt%). It was expected that the microstructure of R260-60E1 parent rail steel will be pearlitic. These findings were compatible with the findings presented by Garnham and Davis (2008) on the same rail grade.



Figure 4-10: Microstructure of a TW R260-60E1 pearlitic rail steel taken on the weld centre. [Etched in 5% nital, 500x magnification].

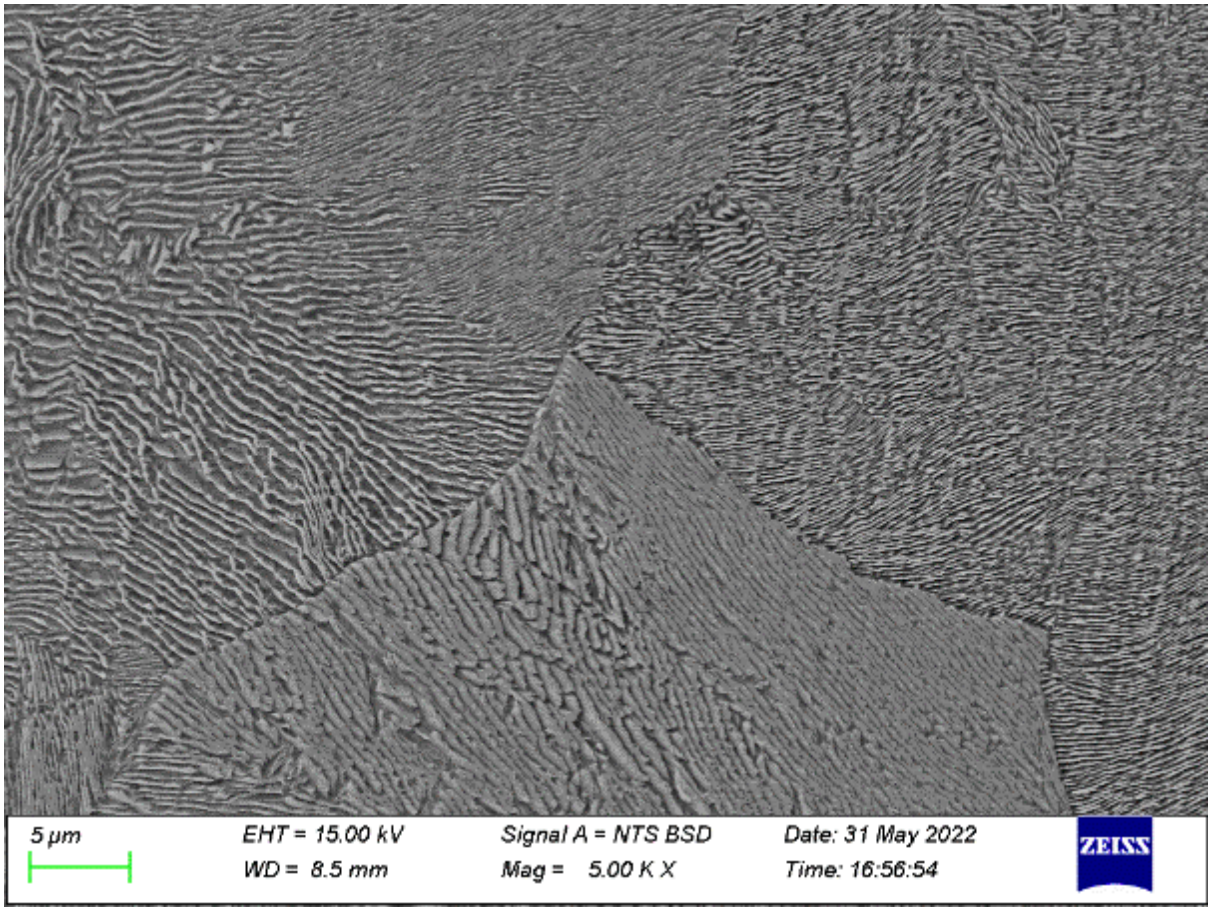


Figure 4-11: SEM image of a TW R260-60E1 pearlitic rail steel taken at the weld centre of a sample with a 50 mm weld gap using high magnification [5000x magnification]. Similar SEM image was obtained on the sample with a 40 mm weld gap.

Microstructures shown in Figures 4-10 (OP) and 4-11 (SEM) were taken on the foot region at the weld centre of the sample with a weld gap size of 50 mm. A similar microstructure was also noted on the sample with a weld gap size of 40 mm. The dominant microstructure was the pearlite structure. The pearlitic phases were in brown colour, with proeutectoid ferrite in white colour which was formed around inclusions along the grain boundaries (Figures 4-10).

No unwanted phases such as martensite or bainite were noted on the structure. This could have been that the rail ends were preheated for 6 minutes (Table 3-2) to control the solidification rate and the microstructures that formed, and to eliminate shrinkage cavities. The microstructure results found on TW for both the weld gap of 40 mm and 50 mm were consistent with those that were obtained by Meric et al. (2002), and Schroeder and Poirier (1984).

The microstructure on the weld centre was slightly similar to the microstructure found on the parent rail as they also showed fully pearlitic structures. Similarities of the microstructure of the weld rail and parent rail were as a result of the carbon content that was greater than 0.55 wt%, with the heat input in the weld centre high enough to produce a fully pearlitic structure

in all 3 regions (Table 3-1). The microstructure of the weld centre, in terms of grain and phase modification were similar to those presented by Ilic et al. (1999) in a TW on UIC 860 S49 SAE/AISI 1050 steel rail.

The heat input found in the weld centre was high enough to influence the cooling rate and grain growth. In the presence of high heat input, slow cooling rate and high grain growth were obtained (Gomes et al., 1997). Slow cooling rate allowed the cementite to distribute perfectly and the pearlite formation to occur (Gomes et al., 1997).

The pearlite grains formed during slow cooling rate were coarser when compare to the fine grained pearlites that were formed due to fast-cooling rate (Gomes et al., 1997). The formation of coarse pearlite grains depends not only on the cooling rate but also on the grain growth and heat input (Gomes et al., 1997). The higher the grain growth and heat input, the courser the pearlite grains (Gomes et al., 1997).

Gomes et al. (1997) reported that the fast-cooling rate results in the production of proeutectoid ferrite and finer pearlite grains compared to a slow cooling rate. The results from this research investigation were aligned with the findings by Gomes et al. (1997).

The heat input and cooling rate found in weld centre for samples with the weld gap size of 40 mm and 50 mm only support the formation of pearlite rather than intergranular Widmanstätten ferrite, bainite or martensite structures (Myers et al., 1982). It should also be noted that within the weld centre, the microstructures in the head, web, and foot regions on both samples were invariable as the structure and grain sizes produced were relatively the same. The microstructure similarity on these regions was due to the weld centre temperature that was evenly distributed.

Myers et al. (1982) and Tawfik et al. (2008) reported that the microstructure in the weld centre of the web region had the same grain size as the microstructure in the head and foot of the weld centre, even though the web region had slightly higher surface area to volume ratio than the foot and head of the rail. The surface area to volume ratio of the web region had little or no contribution to the grain growth within the weld centre as the temperature distribution was equal for the head, web, and foot regions (Myers et al., 1982 and Tawfik et al., 2008). Findings

obtained in this investigation were in agreement with results reported by Myers et al. (1982) and Tawfik et al. (2008).

The sample with a weld gap of 50 mm was measured to have a greater ratio of surface area to volume than the sample with the weld gap of 40 mm. It was further established that the greater the surface area to volume ratio, the faster the cooling rate, producing finer pearlite grains. The increase in weld gap increased the cooling rate, and decreased the pearlite grain sizes (Gomes et al., 1997).

The pearlite grain sizes were measured to be 43.60 µm and 41.08 µm on the weld centre of the head region for samples with the weld gap of 40 mm and 50 mm, respectively. Whereas the measured pearlite grain sizes on the web and foot region for the sample with a weld gap of 40 mm were 41.80 µm and 42.2 µm respectively, and for the sample with a weld gap of 50 mm was 40.30 µm and 40.90 µm respectively. The results showed that the sample with a weld gap of 50 mm had a relatively slightly fine pearlite grain size compared to the sample with a weld gap of 40 mm. The sample with a weld gap of 50 mm had a slightly better surface area to vulome ratio when compared to the sample with a weld gap of 40 mm. Greater surface area to volume ratio on the sample with weld gap of 50 mm resulted into a faster cooling rate, and finer pearlite grain sizes.

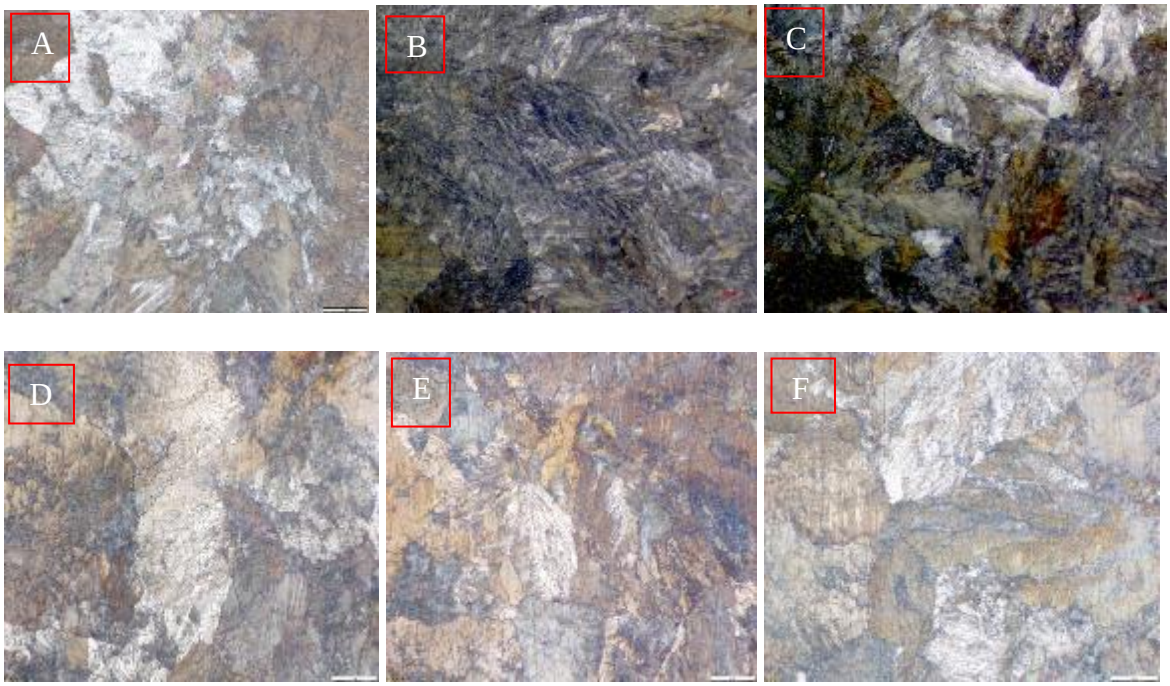


Figure 4-12: Microstructure of the TW R260-60E1 taken on the regions of the weld zone for weld gap of 40mm and 50mm: (a) 40mm-head region, (b) 40mm-web region, (c) 40mm-foot region, (d) 50mm-head region, (e) 50mm-web region, and (f) 50mm-foot region. [Etched in 5%, 500x magnification].

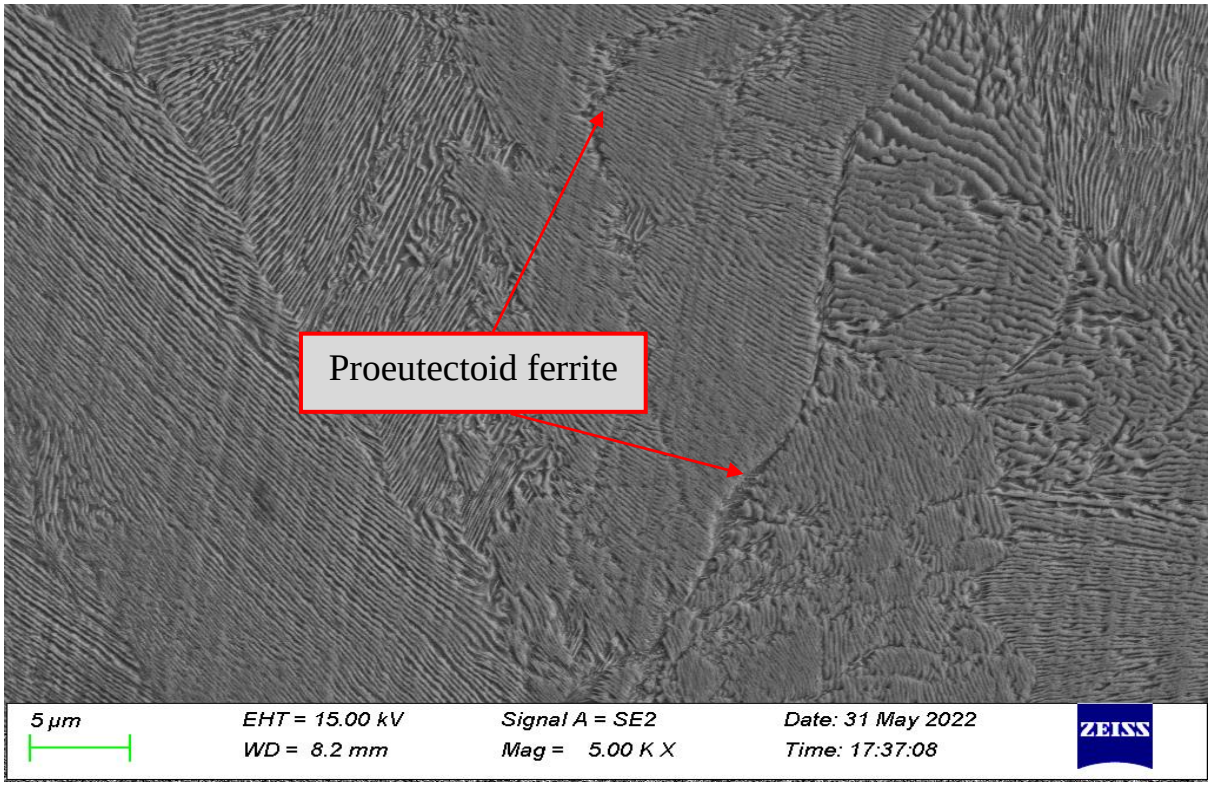


Figure 4-13: SEM image of a TW R260-60E1 pearlitic rail steel taken at the weld zone of a sample with a 50 mm weld gap using high magnification [5000x magnification]. Similar SEM image was obtained on the sample with a 40 mm weld gap.

Figures 4-12 (a-f) and Figure 4-13 showed the microstructures of the R260-60E1 pearlitic rail steels taken in weld zone of the samples with a weld gap of 40 mm and 50 mm for all 3 regions. In both samples, the heat dissipation was higher from the weld centre (region 1) to the weld zone (region 2). As the heat dissipation increased from the weld centre to the weld zone, the cooling rate increased, and the grain growth was reduced. Figure 4-13 showed the proeutectoid ferrite formed on the weld zone due to relatively fast cooling rate.

The measured pearlite grain size in the weld zone of samples presented in Figures 4-12 (a-f) was as follows: (a) 32.34 µm, (b) 30.40 µm, (c) 31.0 µm, (d) 30.80 µm, (e) 29.30 µm, (f) 29.90 µm, respectively. These results showed that as the cooling rate was increased with the move from the weld centre, towards the weld zone, the pearlite grain size was decreased.

Despite the relatively slow cooling rate, and the chemical composition, the thermite weld metal was somewhat comparable to that of the parent rail steel (Table 3-1), the thermal excursion caused by TW brought about series of microstructural changes. Since thermal welds were basically casts, it was expected that the microstructure of the weld zone will consists of long and coarse columnar crystals aligned in the direction of heat flow.

The peak temperature and cooling rate can explain the presence of ferrite at grain boundaries in the microstructure of the weld zone. The grain size of prior austenite can therefore be determined, as delineated by the proeutectoid ferrite (Tawfik et al. 2008). Accordingly, the ferrite at the grain boundaries delineates the convergence of the columnar crystals in the weld centre, and determines the grain size of the prior austenite crystals in the partially molten zone (Tawfik et al. 2008).

Microstructures of weld zone were basically pearlitic, where the slow cooling rate supported the formation of pearlite rather than intragranular Widmanstatten ferrite (Myers et al. 1982). As expected, pearlite grain size in weld zone decreased while moving away from the weld centre. This could be attributed by that upon cooling, the peak temperature decreased and the cooling rate increased on the advancing from weld centre throughout weld zone. Hence, the regions closer to weld centre keept heat longer, and thus more grain growth occured.

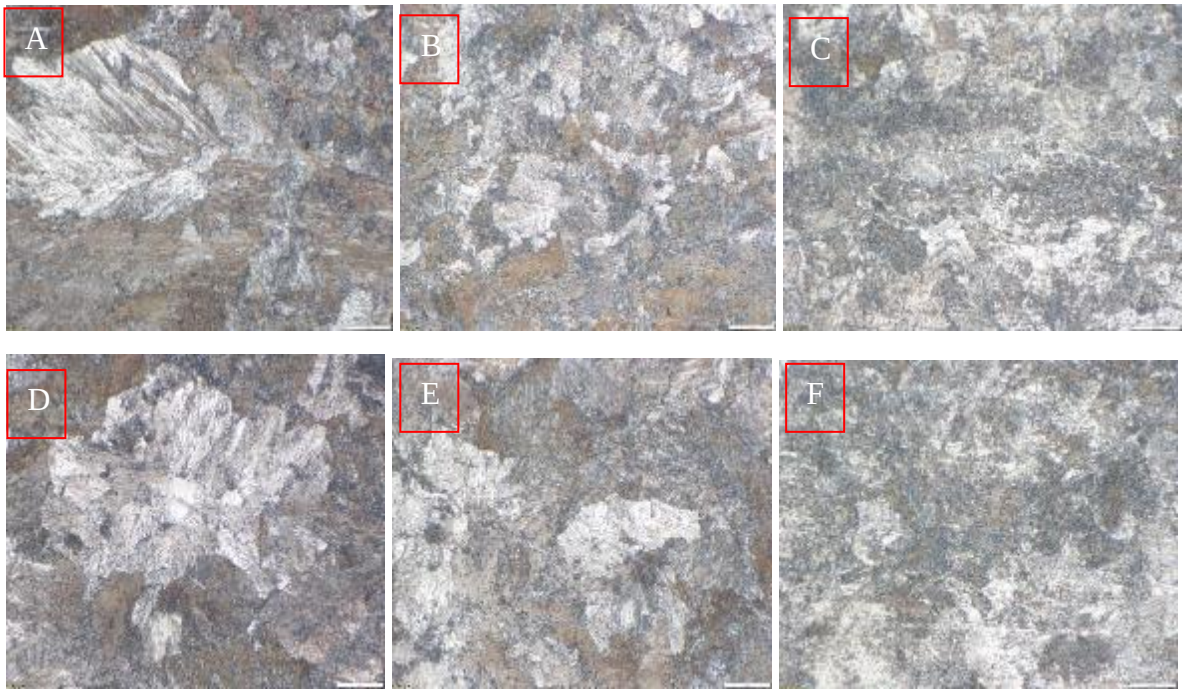


Figure 4-14: Microstructure variation across the TW R260-60E1 rail at the head and web region for weld gap of 40mm; (1) Head region: (a) CGHAZ, (b) FGHAZ, (c) ICHAZ (2) Web region: (d) CGHA (e) FGHAZ, (d) ICHAZ [Etched in 5% nital, 500x magnification].

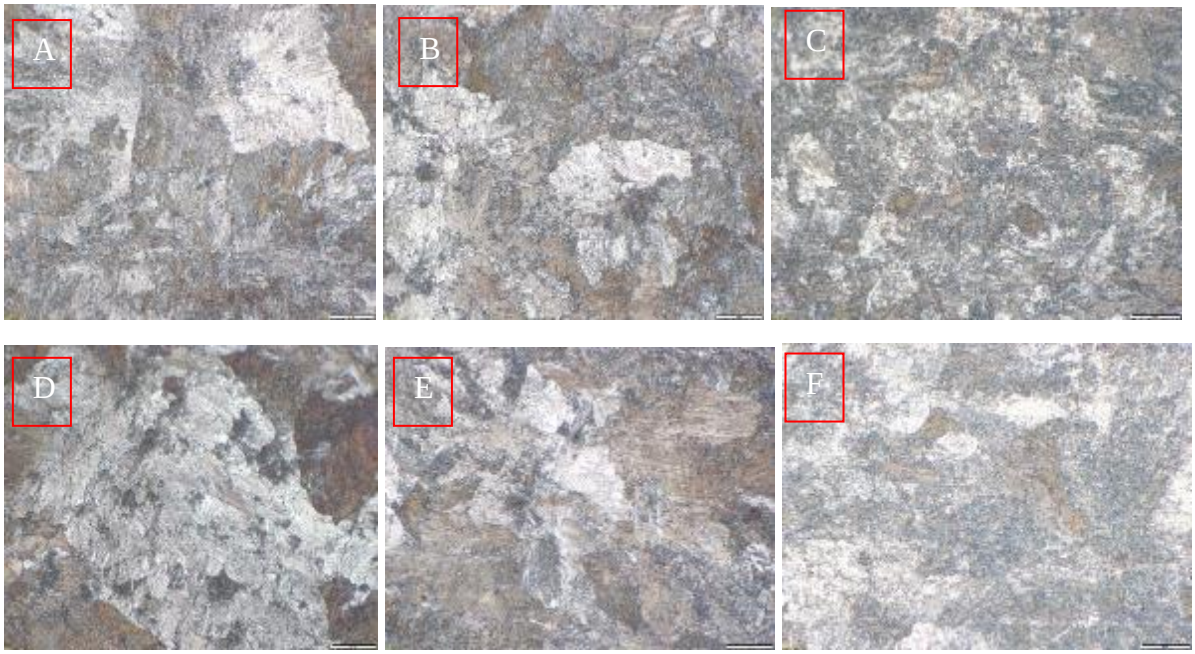


Figure 4-15: Microstructure variation across the TW R260-60E1 rail at the head and web region for weld gap of 50mm; (1) Head region: (a) CGHAZ, (b) FGHAZ, (c) ICHAZ (2) Web region: (d) CGHAZ, (e) FGHAZ, (d) ICHAZ [Etched in 5% nital, 500x magnification].

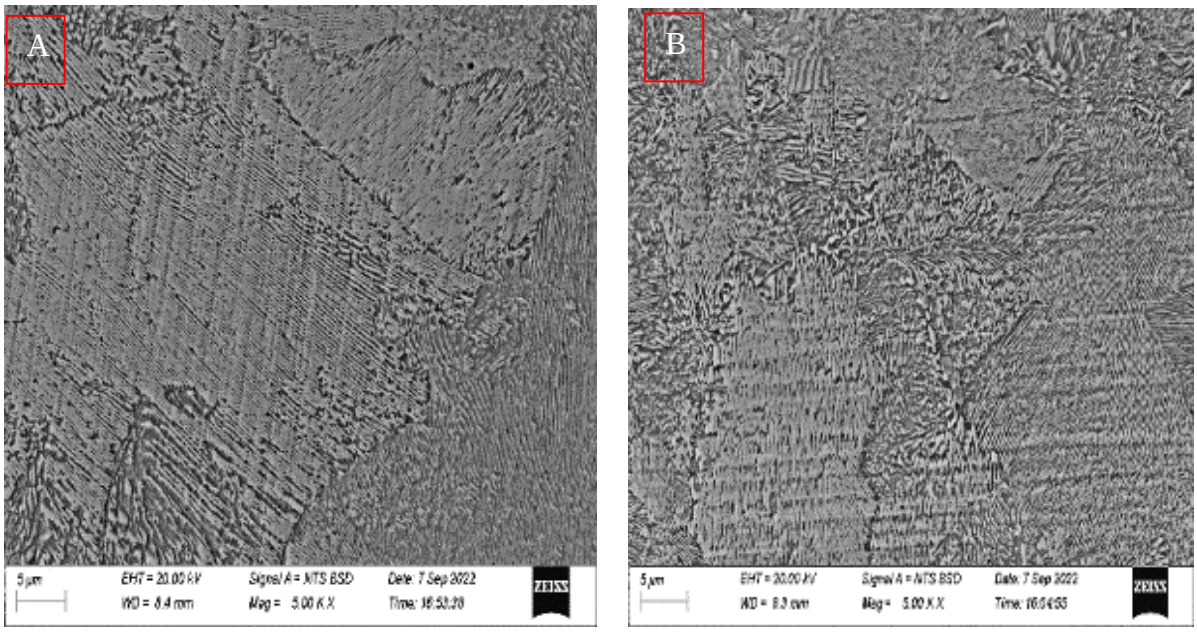


Figure 4-16: SEM image of a TW R260-60E1 rail steel showing pearlite structures at higher magnification for the (a) CGHAZ, (b) FGHAZ [5000x magnification].

Figures 4-15 (a-f) and 4-16 (a and b) showed the HAZ microstructures of the TW R260-60E1 pearlitic rail steels. The HAZ did not experience any melting, but it underwent a phase transformation at high temperatures. The temperature that was experienced in the HAZ decreased with the move from the weld zone towards the parent rail. The transformation of the HAZ grains closer to the weld zone was coarser when compared to the fine grains, which were closer to the parent rail. The HAZ grains transformed into; coarse grain heat affected zone

(CGHAZ), fine grain heat affected zone (FGHAZ) and inter-critical heat affected zone (ICHAZ) for both samples.

Table 4-1: Measured grain sizes of pearlite structure for samples with weld gap of 40 mm and 50 mm.

	40 mm			50 mm		
	Head (µm)	Web (µm)	Foot (µm)	Head (µm)	Web (µm)	Foot (µm)
CGHAZ	30.22	28.7	29.5	29.6	28.5	29.3
FGHAZ	21.4	20.26	21	20	18.8	19.6
ICHAZ	4	3.5	3.8	3.3	2.8	3

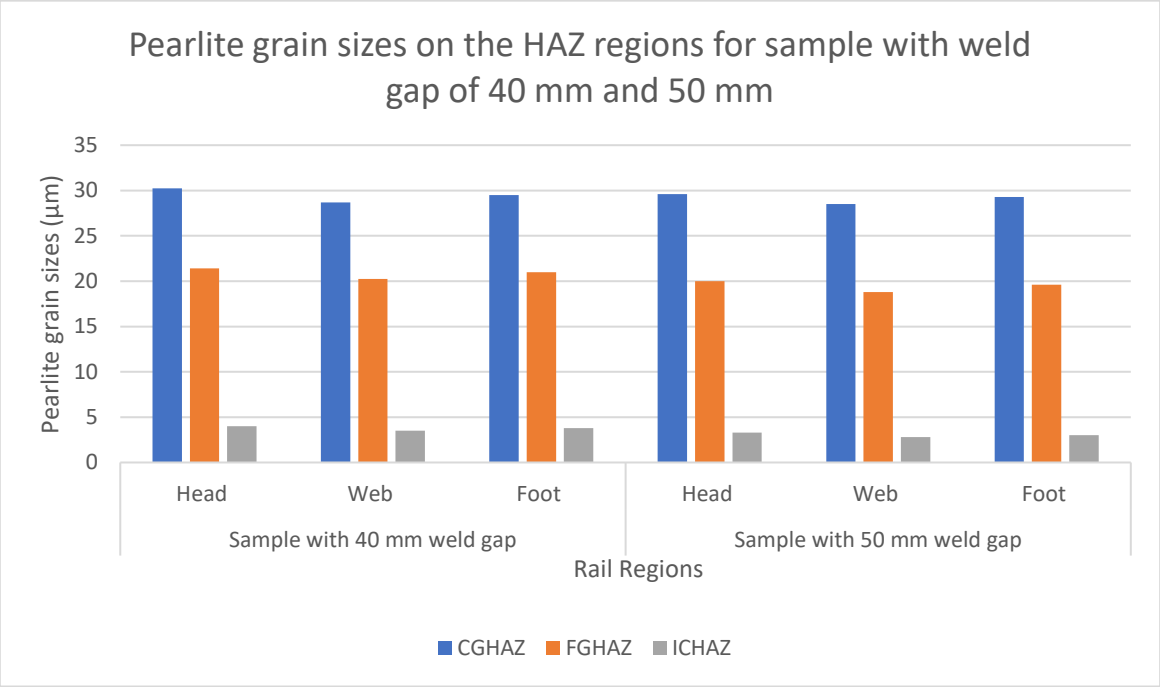


Figure 4-17: Measured grain sizes of pearlite structure for sample with weld gap of 40 mm and 50 mm.

Table 4-1 and Figure 4-17 showed the pearlite grain size effect on CGHAZ, FGHAZ, and ICHAZ when the weld gap was set to 40 mm and 50 mm. The samples with the weld gap of 50 mm were observed to have slightly smaller pearlite grain sizes than the samples with the weld gap of 40 mm.

During TW of rail steels, the CGHAZ in the region adjacent to the partially molten zone was subjected to a higher temperature compared to other regions of the HAZ, and therefore had coarse grains. Moving away, towards the unaffected parent metal, the peak temperature reached by the metal gradually reduced, and grain size decreased. Within the FGHAZ, the region just

above A_3 in the Fe-Fe_3C phase diagram was subjected to a temperature so that the grain growth was slight slower than the CGHAZ, and the grains sizes were finer (Micenko et al., 2013).

Micenko et al. (2013) confirmed that the cementite within the pearlite colony in the intercritical HAZ (between A_1 and A_3) was partially spheroidized during heating of pearlitic rail steel. Micenko et al. (2013) further suggested that the pearlite in the subcritical HAZ was subjected to tempering, in addition to a possibility of spheroidization, although the microstructure in this zone appears very similar to that of the unaffected parent metal.

The ICHAZ had the smallest pearlite grain sizes for both samples. The small pearlite grain sizes on the ICHAZ was due to the ICHAZ experiencing temperature that was below critical temperature (below A_1 temperature), within this temperature range, partially spheroidized pearlite structures and refined grains of pearlite were formed.

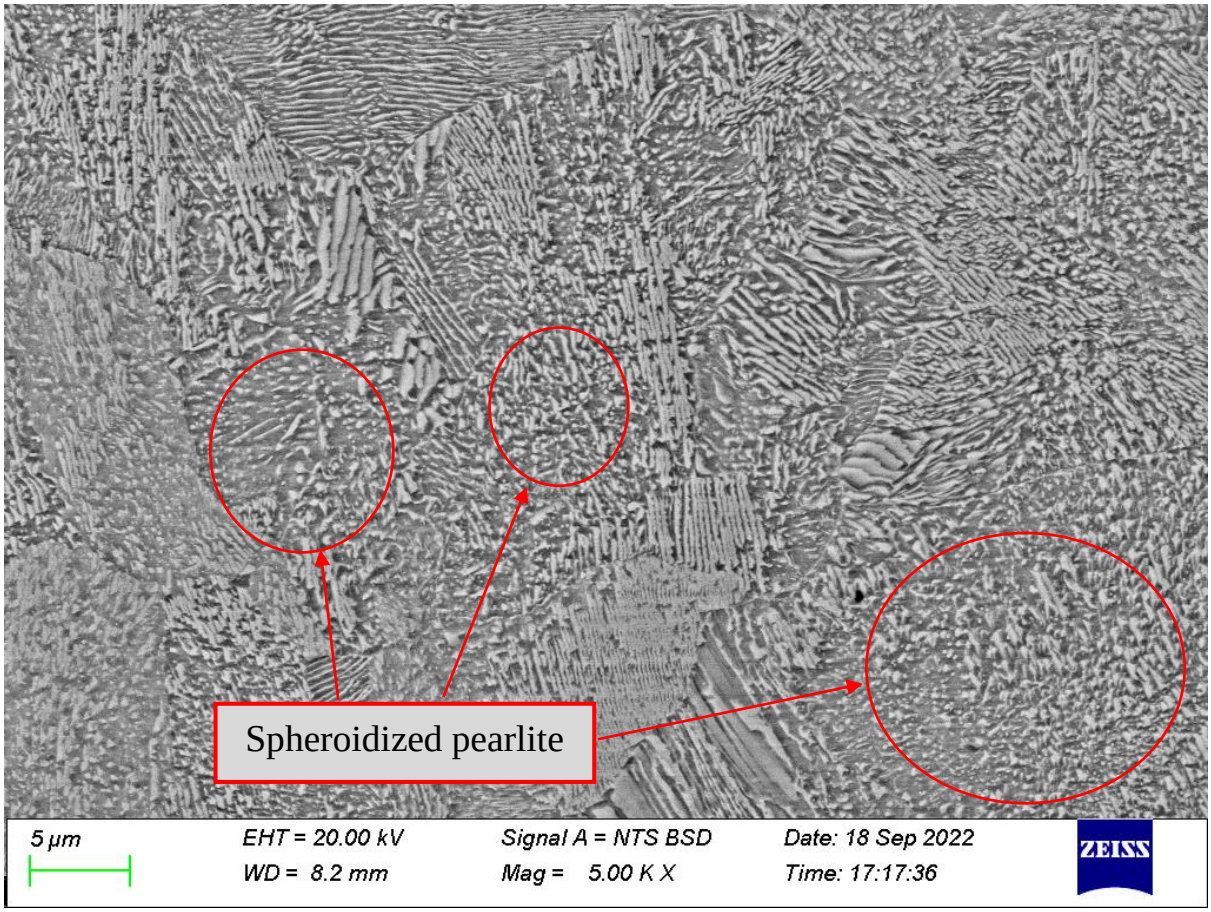


Figure 4-18: SEM image of a TW R260-60E1 rail steel showing pearlite structures at higher magnification for the ICHAZ [5000x magnification].

Figure 4-18 showed the SEM microstructure of the ICHAZ. The ICHAZ experienced a temperature that was below critical temperature (below the A_1 temperature) (Micenko et al.,

2013). Within the critical temperature range, there was a formation of spheroidized pearlite structures and refined grains of pearlite (as indicated in Figure 4-17) (Micenko et al., 2013). These spheroidized pearlite structures formed because the temperature range provided low free energy and an interfacial area to form lamellar pearlite structures (Micenko et al., 2013).

4.1.4.2 X-Ray diffraction

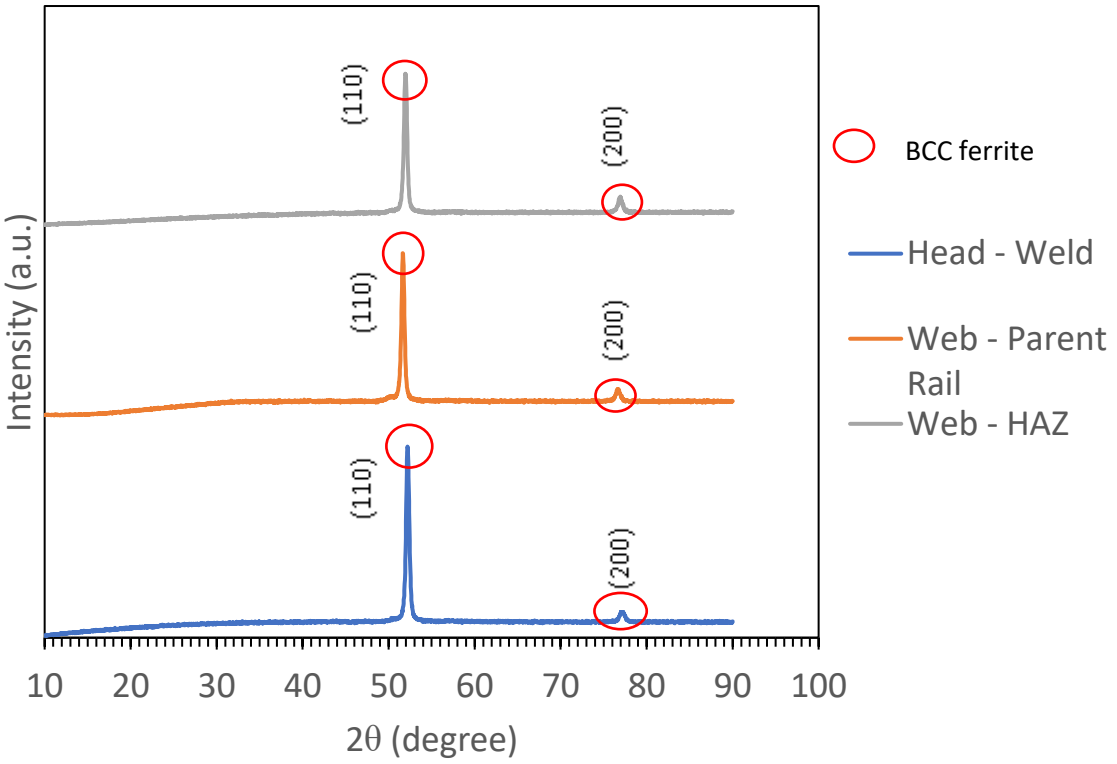


Figure 4-19: X - -Ray diffraction patterns for TW R260-60E1 rail sample with a weld gap of 50 mm.

Figure 4-19 showed XRD patterns of TW R260-60E1 pearlite rail steel sample with a weld gap of 50 mm. The samples were extracted as follow; head – weld, web – parent rail, and web – HAZ. The extraction was done on both the sample with weld gap of 40 mm and 50 mm. Similar results were obtained for both the 40 mm and 50 mm weld gap samples.

The XRD results for all the 3 regions (head, web and foot) tested in both the samples revealed that the BCC - ferrite phase was dominant as the matrix of pearlite structure with a small amount of cementite phase as products of eutectoid transformation (Webster et al., 2002).

The XRD spectra of the surface of the head – weld, web -parent rail, and web – HAZ regions showed $(110)_{ferrite}$ and $(200)_{ferrite}$ peaks, which were slightly asymmetric and there was also evidence of "blurred" and weak cementite peaks (Webster et al., 2002). These results showed that the cementite fully dissolved in the matrix by austenitization. The results further showed

lack of evidence of retained austenite, brittle martensite and/or presence of bainite phases (Myers et al., 1982).

The existence of the "blurred" and weak cementite indicates that there was perfect distribution of cementite during the slow cooling process, resulting in the formation of pearlite structures (Cullity and Stock, 2009). The (110) $_{ferrite}$ and (200) $_{ferrite}$ peaks obtained from the XRD spectra for the tested samples indicated that the high heat input and slow cooling rate on the tested samples supported the formation of pearlite structures rather than the formation of Widmanstätten ferrite bainite and / or martensite structures (Myers et al., 1982). The absence of unwanted phases such as martensite and / or bainite indicated an improvement of the samples microstructure characterisation (Myers et al., 1982).

4.1.5 Hardness distribution



Figure 4-20: Hardness distribution across the TW R260-60E1 grade rail steel of 40mm weld gap sample indented from the weld centreline to the parent rail of the head, web, and foot region.

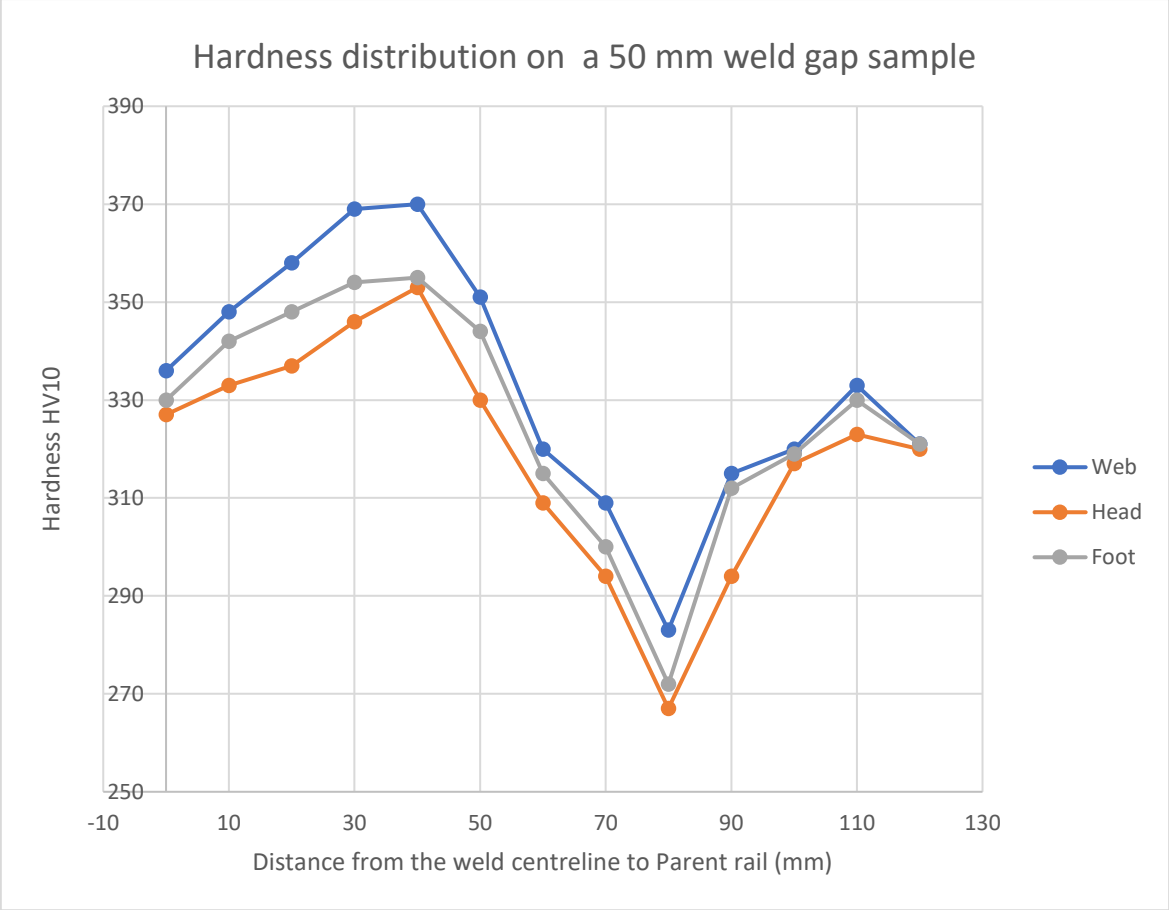


Figure 4-21: Hardness distribution across the TW R260-60E1 grade rail steel of 50mm weld gap sample indented from the weld centreline to the parent rail of the head, web, and foot region.

Table 4-2: Summary of hardness distribution values for the TW R260-60E1 rail weld on the 40 and 50 mm weld gap samples.

	40 mm weld gap				50 mm weld gap			
Regions	Weld centre (HV_{10})	Maximum (HV_{10})	Minimum (HV_{10})	Max Parent rail (HV_{10})	Weld centre (HV_{10})	Maximum (HV_{10})	Minimum (HV_{10})	Max Parent rail (HV_{10})
Web	325	358	253	307	336	370	283	333
Head	320	352	231	290	327	353	267	323
Foot	325	355	240	306	330	355	272	330

The hardness distribution across the TW 260-60E1 pearlitic rail steel for sample with a weld gap size of 40 mm and 50 mm are shown in Figures 4-20 and 4-21, respectively. Whereas,

Table 4-2 showed the summary of the hardness distribution values for the TW R260-60E1 samples.

The hardness values on the web region were seen to gradually increase with the move from the weld centreline towards the parent rail for both samples. The hardness value for weld centreline was 325 HV_{10} for sample with weld gap of 40 mm and 336 HV_{10} for sample with a weld gap 50 mm, whereas the maximum hardness value for parent rail was 358 HV_{10} for sample with weld gap of 40 mm and 370 HV_{10} for sample with weld gap 50 mm. The minimum hardness value on a parent rail for sample with gap of 40 mm was 253 $HV_{10,}$ while on a sample with weld gap of 50 mm was 283 $HV_{10.}$The minimum hardness values for both samples was obtained near the visible extent of the HAZ on the ICHAZ. The low hardness value on the ICHAZ was attributed by the presence of partially spheroidized pearlite structures and refined grains of pearlite.

The hardness profile was seen to gradually recover with the move from the ICHAZ to parent rail. The obtained maximum hardness value was 307 HV_{10} and 333 HV_{10} for a sample with the weld gap of 40 mm and 50 mm respectively. The hardness improvement in the parent rail was attributed by high carbon cantent and presence of fully pearlitic structures.

The web region hardness results showed that the sample with a weld gap of 50 mm had better or greater hardness values when compared to those found on sample with the weld gap of 40 mm.

Slow cooling rates attributed to a larger interlamellar spacing of the pearlitic steels, which in turn, resulted into a decreases on the hardness values (Gomes et al. 1997). The hardness values of the weld zone exceeded those of the parent rail, even with preheating of the samples. The variations in results were affected by the change in cooling rate, pearlite grain size, and interlamellar spacing (Gomes et al., 1997).

The results in Figures 4-20 and 4-21 showed that the weld centre exhibited coarser pearlite grain sizes and interlamellar spacing in comparison to weld zone and parent rail. The coarse pearlite grain size and interlamellar spacing at the weld center resulted in a decreasing hardness distribution profile, in contrast to the increasing hardness distribution curve observed across the weld zone (Gomes et al., 1997). The increase in the hardness distribution profile on the weld zone was attributed by finer pearlitite grain sizes and interlamellar spacing. These observation were aligned with Gomes et al. (1997) findings.

The results in Table 4-2 showed that the web region in the parent rail had a maximum hardness profile of 307 HV_{10}, for sample with weld gap of 40 mm, and 333 HV_{10} for sample with weld gap of 50 mm. Both the hardness results were within the EN ISO 6507-1 specification limit of (260 – 342) HV_{10}. The results further showed that the web region of the welded rail had a maximum hardness value of 358 HV_{10} for sample with weld gap of 40 mm, and 370 HV_{10} for sample with the weld gap of 50 mm. Both the hardness results were within the EN ISO 6507-1 specification where the maximum hardness in the weld should not be more than (260 – 342) HV_{10} + 60 HV_{10}. The maximum hardness distribution in the foot and the head regions were 355 HV_{10} and 352 HV_{10}, respectively for sample with weld gap of 40 mm. whereas the maximum hardness distribution in the foot and the head regions for sample with the weld gap of 50 mm were 355 HV_{10} and 353 $HV_{10,}$ respectively.

Table 4-2 showed that the sample with the weld gap of 40 mm had the minimum hardness values of 253 HV_{10} on the web region, 240 HV_{10} on the foot region, and 231 HV_{10} on the head region. These hardness values were within the EN ISO 6507-1 specification where the minimum hardness on the weld should not be less than (260 – 342) HV_{10} - 30 HV_{10}. Whereas the sample with weld gap of 50 mm had a minimum hardness distribution profile values of 283 HV_{10} on the web region, 272 HV_{10} in the foot region, and 267 HV_{10} in the head region. These hardness values were within the EN ISO 6507-1 specification where the minimum hardness in the weld should not be less than (260 – 342) HV_{10} - 30 HV_{10}. The minimum hardness across the weld, observed in the intercritical zone, could be attributed to the partially spheroidized pearlite structure in this zone which consists of a partially spheroidised cementite in a soft ferrite matrix. These results are aligned with by Myers et al. (1982), Schroeder and Poirier (1984) and Merıç et al. (2002) findings.

The area which was closest to the parent rail, and which had the liw hardness values is known as the inter-critical heat affected zone (ICHAZ). The ICHAZ experienced temperature that was below the critical temperature, A_1 (Micenko et al., 2013). The microstructure in this area was almost similar to the microstructure of the parent rail. However, partially spheroidized pearlite and fine pearlitic grains were formed in this region.

Meade (1999) suggested that the TW rail joints which had low hardnes in the fusion zone, weld zones or wide HAZ were susceptible to batter (localized plastic deformation due to variations in strength or hardness across the weld), which resulted in increased impact loading and

contributed to premature failure of the weld. The extent of the batter can be limited by rail grinding, which is carried out as part of a prevention maintenance profile.

The findings of this investigation are in agreement with the study by Meric et al. (2002) where it was reported that hardness evaluation of the thermite welded rails that were subjected to preheating, showed maximum hardness values at the edge of the weld rail, whereas minimum values were observed at the interface between the HAZ and the parent rail. The preheating duration of 6 minutes was achieved for this research investigation.

A study by Saarna and Laansoo (2004) suggested that high hardness was most preferred as it increases resistance to fatigue and deformation. Meade (1999) further recommended that hard welds hold better under increasingly hard axle loadings and help prevent rail head depressions at the weld. Saarna and Laansoo (2004), and Meade (1999) findings indicated that the sample with the weld gap of 50 mm will have better resistance to fatigue failures and any deformation since they showed high hardness results when compared to the sample with the weld gap of 40 mm.

4.1.6 Mechanical properties

Mechanical properties have a strong correlation with microstructural grain size, hardness distribution and HAZ width. The mechanical tests results (tensile strength and impact toughness) for TW R260-60E1 did not present a significant variance between samples with the weld gap size of 40 mm and 50 mm. For the purpose of this research investigation, the sample with the weld gap of 50 mm was therefore used to conduct mechanical testing because it showed slightly better results.

The width of the HAZ has an impact on mechanical properties of the welded rail. Saita et al. (2013) reported that a wide HAZ width showed poor mechanical properties and high residual stresses, whereas narrow HAZ width showed good mechanical properties and low residual stresses. From the current investigation, a narrow HAZ was observed in the 40 mm weld gap sample, and a wider HAZ width observed in the 50 mm weld gap sample.

An investigation by Garcia et al. (2017) on the microstructure and mechanical properties of rail aluminothermic welding reported that welds with wide gap had narrow lamellar spacing between the ferrite and cementite in the pearlite, which in turns decreased plasticity and elongation, and increased the yield strength, tensile strength and hardness when compared to welds with narrow gaps.

Garcia et al. (2017) further reported that welds with wide gaps required less preheating duration and temperature when compare to welds with narrow gap (Table 2-9 and 2-10). For this research investigation, both the samples with a 40 mm and 50 mm weld gap were preheated for 6 min, at 950˚C temperature. Chen et al. (2014) reported that the larger weld gap (52 mm) helps eliminate the development of shrinkage cavity, and can reduce the preheating time and the average liquid temperature significantly.

4.1.6.1 Tensile testing

Tensile tests were carried at room temperature on five pieces of the TW R260-60E1 pearlitic rail steels. The pieces that were tested were extracted as follow; head-parent rail, head- HAZ, head-weld, web-HAZ, and web-weld. No piece was taken on the foot region as it showed closely related properties to those in the head region.

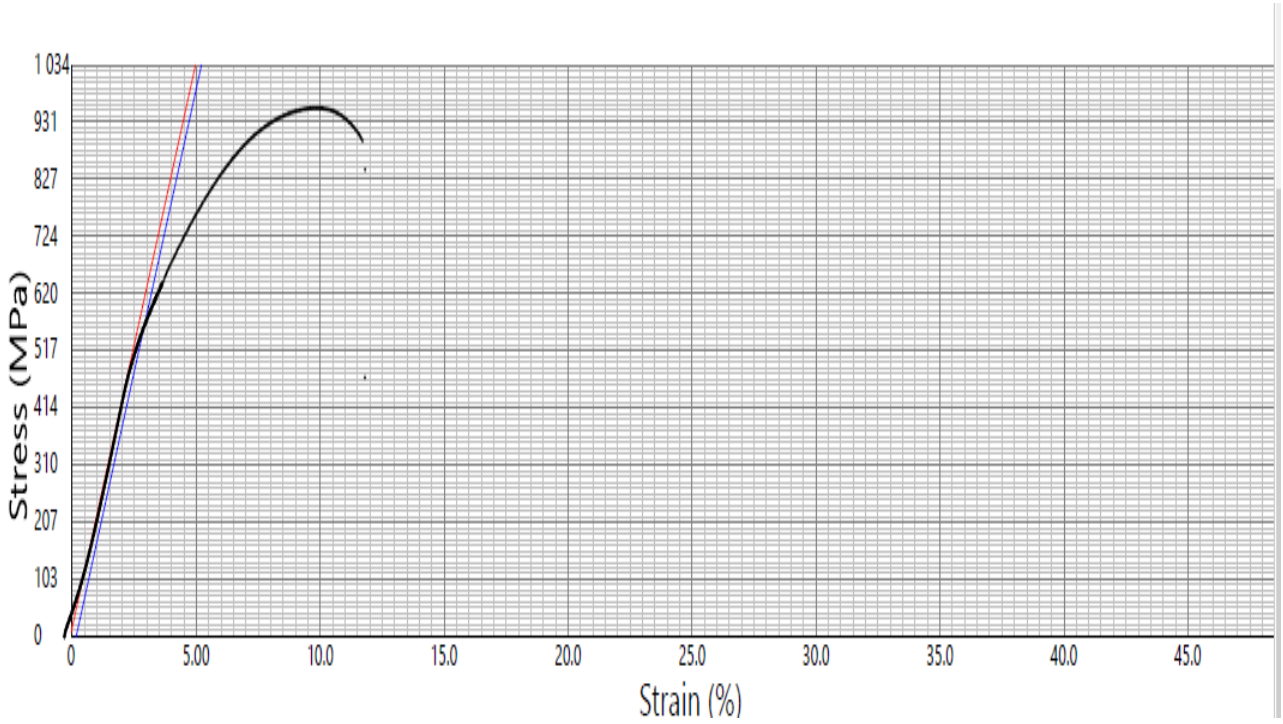


Figure 4-22: Mechanical tensile stress vs tensile stain curve typical of high strength and high ductile material of a head - parent rail sample with a weld gap of 50 mm.

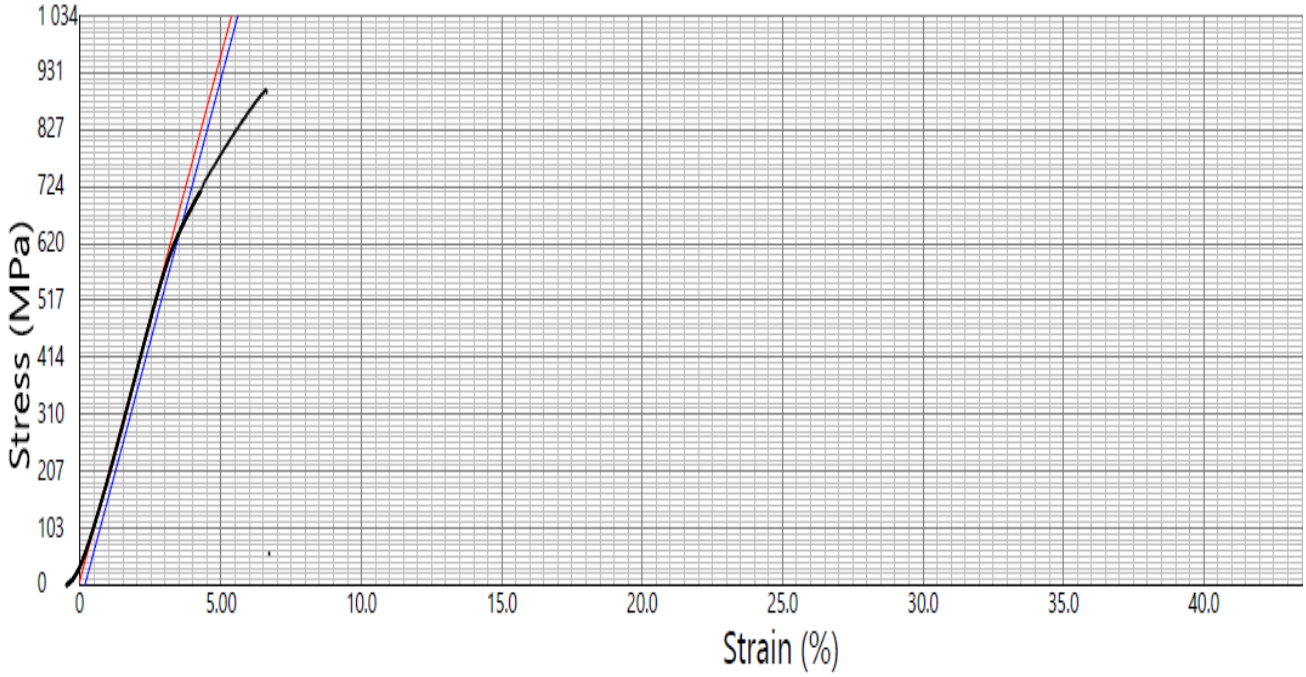


Figure 4-23: Mechanical tensile stress vs tensile stain curve typical of high strength and high ductile material of a head - HAZ sample with a weld gap of 50 mm.

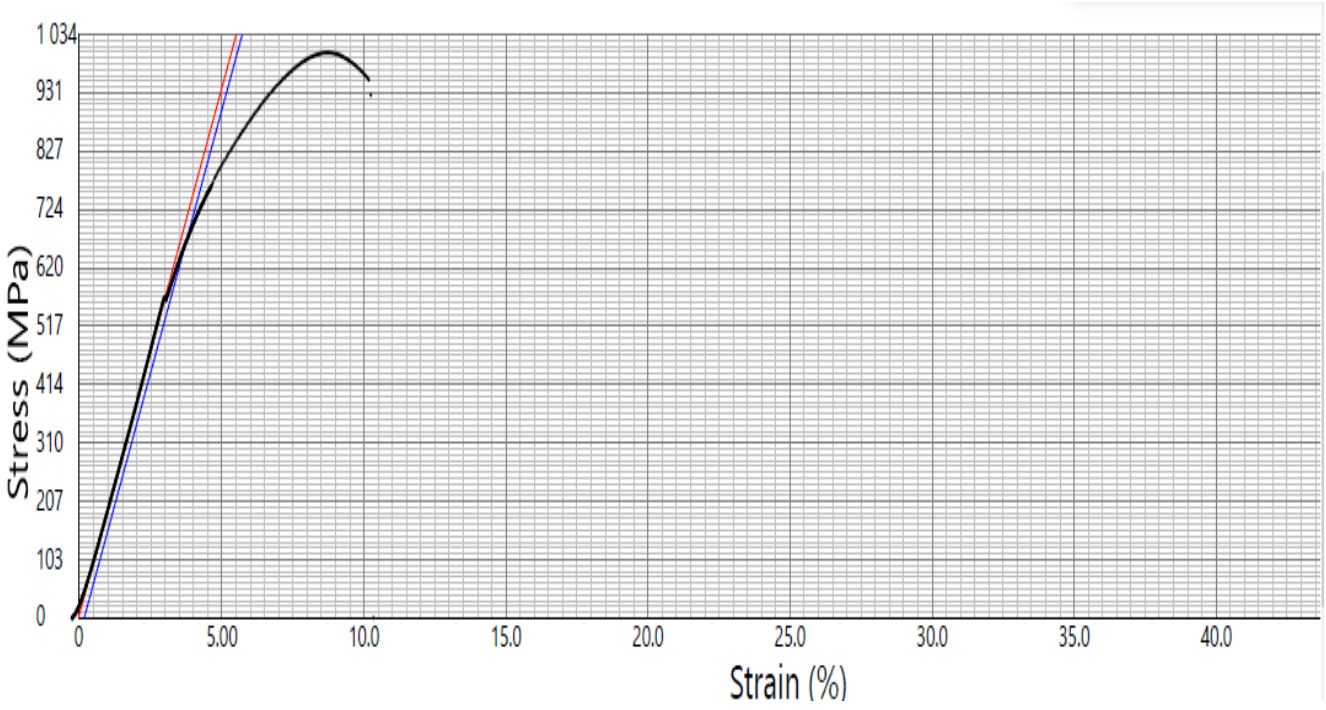


Figure 4-24: Mechanical tensile stress vs tensile stain curve typical of high strength and high ductile material of a web - HAZ sample with a weld gap of 50 mm.

Figure 4-22 to 4-24 showed the tensile stress vs strain curves of high strength and ductility material obtained during testing. Figure 4-22 showed that the head-parent rail had mechanical

tensile stress of 956 MPa with a strain of 11.80%. Whereas, Figure 4-24 showed that the web-HAZ sample had mechanical tensile stress of 1080 MPa with a strain of 10.2 %.

Table 4-3: Tensile test results of a TW R260-60E1 rail steels.

R260-60E1 Rail	UTS (MPa)	Elongation (%)
Head-Parent rail	956	11.80
Head-HAZ	913	7.30
Head-Weld	874	6.43
Web-HAZ	1080	10.2
Web-Weld	900	6.90

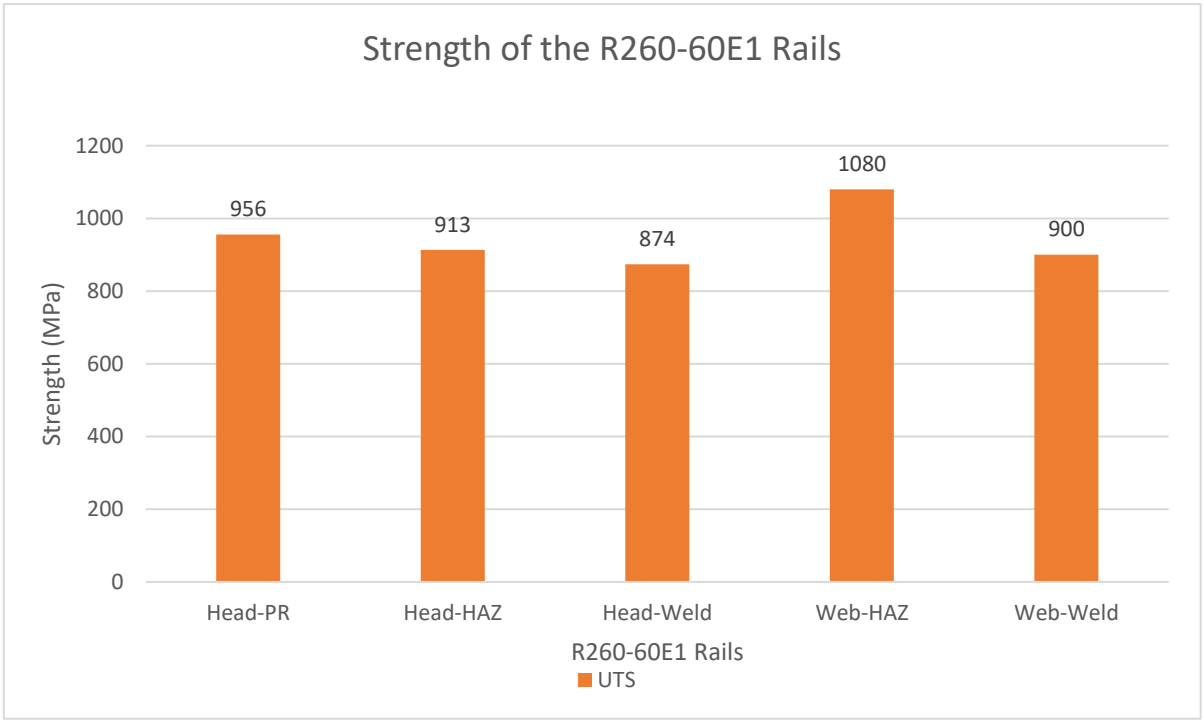


Figure 4-25: UTS results for TW R260-60E1 rails at room temperature.



Figure 4-26: Photo showing the sample that was tensile tested on the HAZ of the web region.

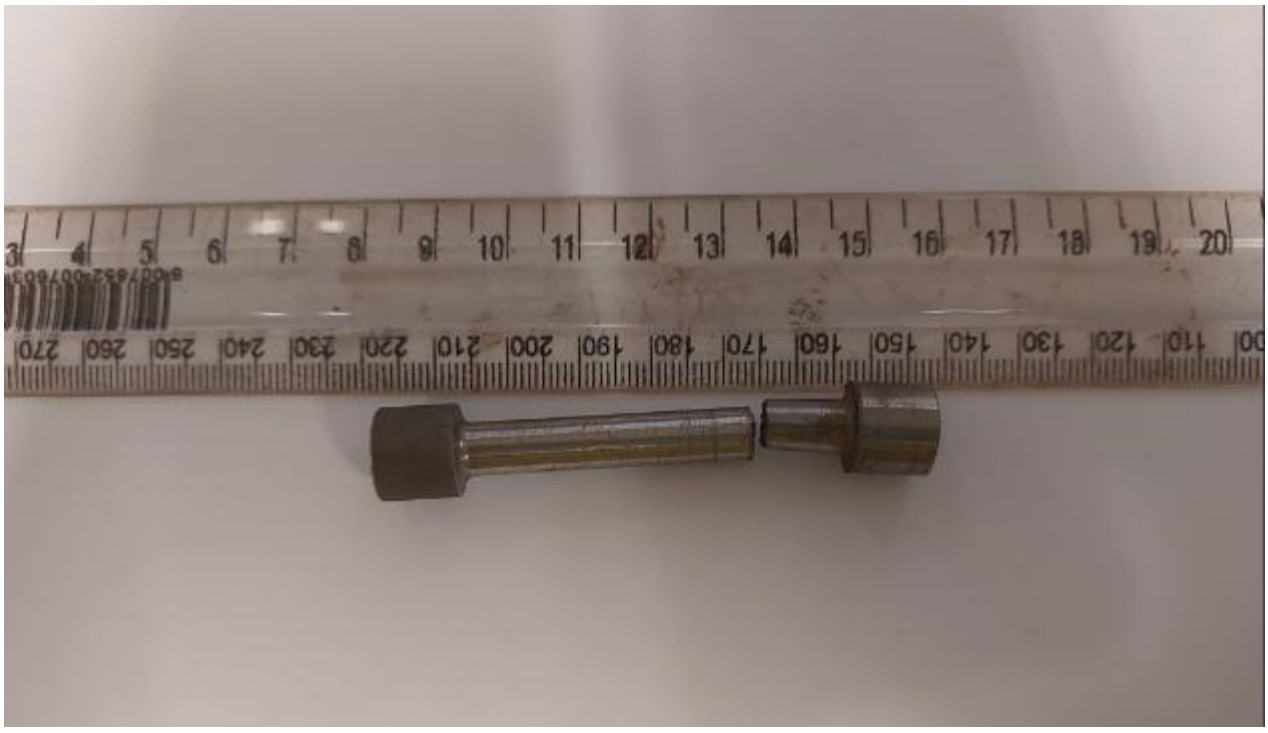


Figure 4-27: Photo showing the sample that was tensile tested on the weld of the web region.



Figure 4-28: Photo showing the sample that was tensile tested on the parent of the head region.



Figure 4-29: Photo showing the sample that was tensile tested on the weld of the head region.

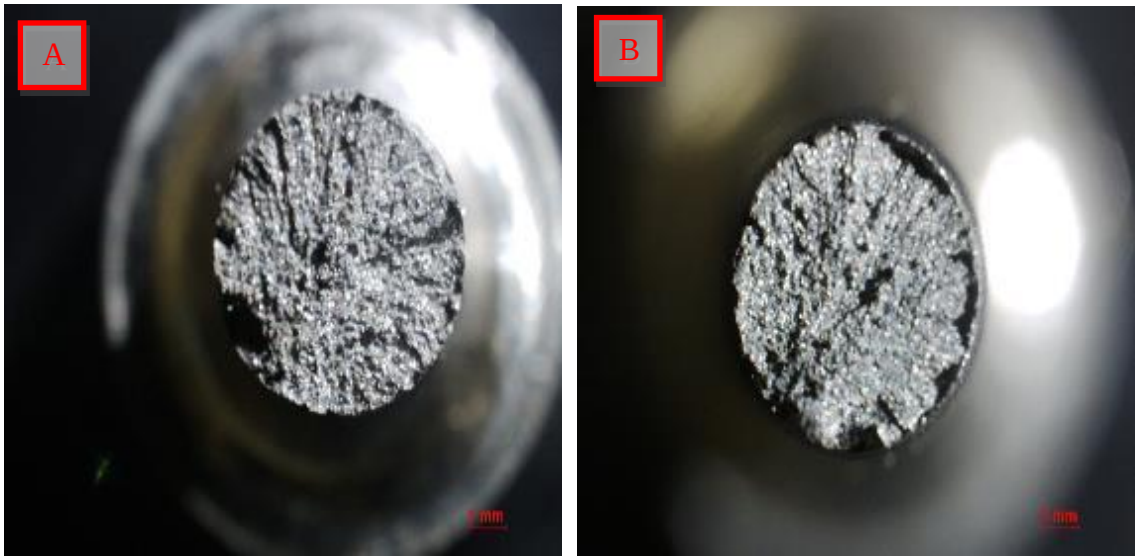


Figure 4-30: Fracture surface stereo image of the sample that was tensile tested on the HAZ of the web region. The fracture surface showed partial brittle with a flat appearance. Similar images were observed on the other samples.

The tensile test results of all the 5 pieces were shown in Table 4-3 and Figure 4-25. The ultimate tensile strength (UTS) measured on the parent rail of the head region (Head – parent rail) was 956 MPa, with an elongation of 11.8%. The UTS conformed to the EN 13674-1 code in which R260-60E1 pearlitic rail sample had a minimum UTS of 880 MPa and a minimum elongation of 9%. These results also conformed with the findings by Sonon et al. (1978) and Myers et al. (1982), where the standard pearlite rail steel had an average yield strength of 480 MPa, UTS of 910MPa, elongation of 11% (a 25.4 mm gauge length) and a reduction in the area of 14% by comparison.

The ultimate tensile testing strength (UTS) measured on the weld of the head region (Head-weld) and the web region (Web-weld) were 874 MPa and 900 MPa, respectively. The measured weld UTS results on the head and web region were below the measured parent rail UTS of 956 MPa. The parent rail was estimated to have greater UTS than welded rail, which was attributed to the fact that parent rail had a higher carbon content and higher ductility than the weld, which exhibited brittle behaviour.

Saita et al. (2013) focused on comparing the properties of the JIS60 rail grade material (parent material) with those of thermite welded rails. The study indicated that although the chemical composition of welded rails were similar to that of the parent rails, the microstructure and mechanical properties differed. Similar observations were made in this study. To improve the microstructure characterisation, mechanical properties, and residual stresses of the JIS60 rail material, post weld heat treatment was applied (Saita et al., 2013).

The difference in the weld UTS between the head and web regions was further impacted by the pearlite grain sizes, interlamellar spacing and cooling rate (Myers., 1982). The UTS measured on the HAZ of the head region (Head-HAZ) and the web region (Web-HAZ) were 900 MPa and 1080 MPa, respectively as noted in Table 4-3 and Figure 4-25. The measured UTS results in the head-parent was 956 MPa. The results showed that the UTS measured in the head – parent was above the UTS of the head HAZ, but below the UTS measured on the web - HAZ. The narrow HAZ width on the web region had a significant impact on improving the UTS. This region experienced a fast cooling rate, resulting in refinement of the pearlite grain sizes and interlamellar spacing in the region, rendering them fine.

The tensile strength of the 50 mm weld gap was significantly higher than the 40 mm weld gap. This proved that the wider weld gap had better properties than the narrow weld gap. The findings from this investigation were aligned with results reported by Mohassel et al. (2011) on mechanical and metallurgical properties of wide gap aluminothermic rail welds.

4.1.6.2 Charpy Impact testing

Charpy impact tests was performed at room temperature and was carried on the head – parent rail, head – HAZ, head – weld, web – HAZ, and web – weld pieces of TW R260-60E1 pearlitic rail steel. No piece was taken on the foot region as it showed closely related properties to those in the head region.

Table 4-4: Impact test results of a TW R260-60E1 rail steel samples with a 50mm weld gap.

R260-60E1 Rail	Impact Energy (J)	UTS (MPa)
Head-Parent rail	4	956
Head-HAZ	4.8	913
Head-Weld	5.6	874
Web-HAZ	4.3	1080
Web-Weld	6	900

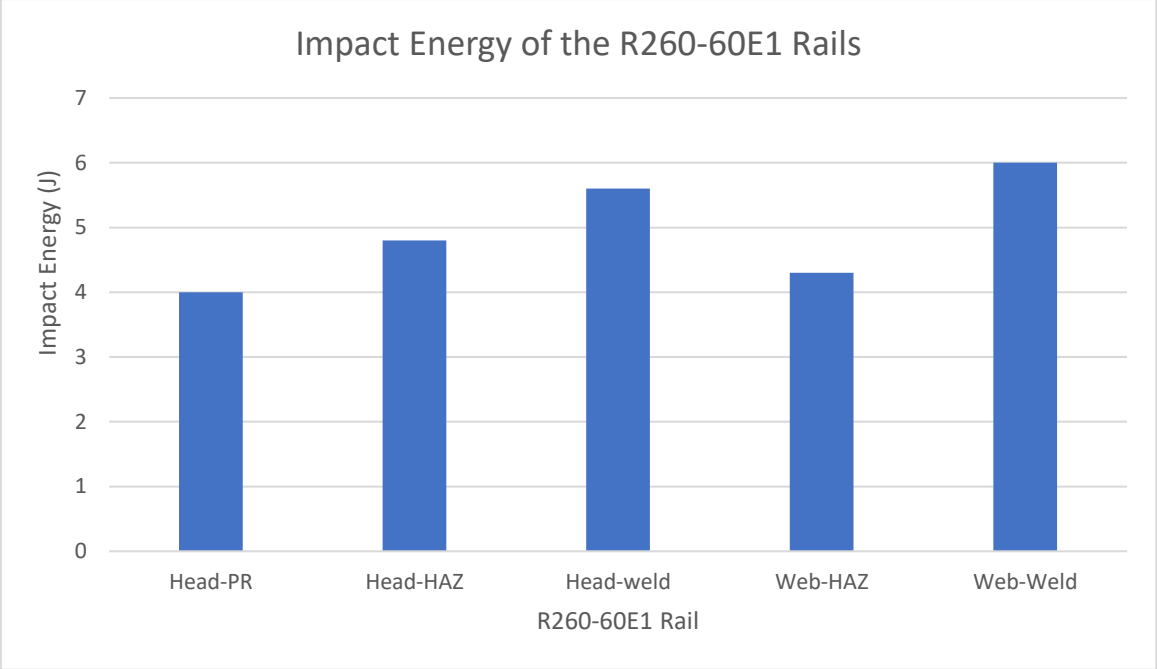


Figure 4-31: Impact Energy for TW R260-60E1 rails at room temperature.

The results indicated that TW R260-60E1 pearlitic rail steel samples exhibited a low impact energy at room temperature. The low impact energy indicated that samples were brittle and required less energy to break. The brittle behaviour on TW R260-60E1 pearlitic rail steel samples was attributed to higher carbon content of the parent rail (0.756 wt % C) and weld metal (0.568 wt % C).

The impact energy results obtained on the weld of the head region (Head-Weld) and web region (Web-Weld) were 5.6 J and 6 J, respectively as indicated in Table 4-4 and Figure 4-31. The impact test results obtained on parent rail of the head (Head-Parent rail) was 4 J and the values obtained on HAZ of the head region (Head-HAZ) and web region (Web-HAZ) were 4.8 J and 4.3 J, respectively as indicated in Table 4-4 and Figure 4-31. These results were consistent with the nature of TW R260-60E1 pearlitic rail steel material, which was characterised by its high material strength and high carbon content, contributing to its brittle behaviour.

An investigation by Mohassel et al. (2011) reported that the fracture toughness mean value of wide gap and narrow welds were 75% and 60% of parent rail respectively. The mean value of wide gap weld fracture toughness were found to be lower than the average of those reported for carbon steel and higher than narrow gap welds. For this investigation, the the fracture toughness difference between the head-parent rail (4 J), and the web-weld (6 J) for the weld gap of 50 mm was 2 J. The sample with the weld gap of 50 mm had a slighy higher toughness

when compared to the sample with the weld gap of 40 mm. Therefore, the findings from this investigation were aligned with findings by Mohassel et al. (2011).

High toughness on the sample with the weld gap of 50 mm was contributed by high average hardness values found on this weld, slightly fine pearlitic grain sizes, and narrow pearlitic interlamellar spacing when compared to the sample with the weld gap of 40 mm (Gomes et al., 1997).

The results further showed that the welded samples had a slightly higher impact energy than the parent and HAZ rail. The obtained impact energy results for the head – HAZ and head – weld tested rail sample pieces had an inversely proportional relationship to the UTS results. As the UTS in each rail sample piece increased, the energy required to break the sample decreased, and when the UTS decreased, the energy required increased as seen in Table 4-4.

The web – HAZ results showed that when the impact energy was 4.3 J, the UTS was 1080 MPa. The low impact energy on this sample was largely contributed by the presence of partially spheroidized pearlite structures and refined grains of pearlite on the ICHAZ which could have reduced the toughness of the region, whereas the high UTS could have been due to the narrow HAZ and fine pearlitic grains, which had a positive impact on the material tensile strength.

The web – weld results showed that when the impact energy was 6 J, the UTS was 900 MPa. High toughness on the sample was due to high average hardness values, slightly fine pearlitic grain sizes, and narrow pearlitic interlamellar spacing. The improvements on the average hardness value, pearlitic grain size, and pearlitic interlamellar spacing had a positive impact on the sample UTS, hence it was 900 MPa, which can be comparable to the parent head UTS of 956 MPa (Gomes et al., 1997).

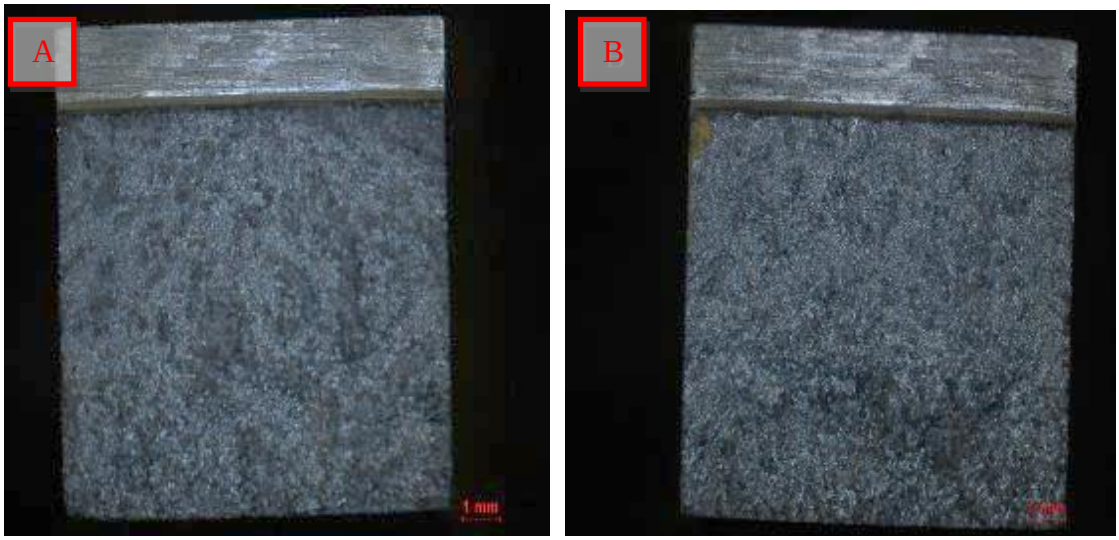


Figure 4-32: Fracture surface stereo image of the impact toughness testing samples showing a flat and shiny appearance, which indicate a brittle fracture mode.

Figure 4-32 showed fracture surface stereo image of the impact toughness test of the TW R260-60E1 pearlitic rail steel HAZ head region sample. The sample showed a flat shiny surface indicating brittle fracture mode. A similar facture surface was observed on the weld and parent rail of the web and head region samples.

4.1.7 Wear testing

The wear testing results of the TW R260-60E1 did not present a significant variance between samples with the weld gap of 40 mm and 50 mm. For the purpose of this investigation, the sample with the weld gap of 50 mm was therefore used to conduct wear testing because the wear response was better.

The abrasive wear tests were perfomed in dry condition at room temperature in order to investigate the tribological properties of TW R260-60E1 pearlitic rail steel. The tests were carried out on the head – parent rail, head – HAZ, web - HAZ, and web – weld pieces. No piece was taken on the foot region as it showed to have closely related properties as those in the head region.

The counter body or ball-on-disc for this test was between the four-pieces of TW 260-60E1 rail steel samples and the 6 mm diameter alumina (L203) ball. Archard equation was used to calculate the specific wear rate (k, mm^3/Nm).

Table 4-5: Specific wear rate on a sliding speed of 0.025m/s.

Rail sample	Sliding distance (m)	Wear volume (mm^3)	COF	Average Hardness (HV_{10})	Specific wear rate (mm^3/Nm) $x10^{-2}$
Head-Parent rail	1.33	0.36	0.36	323	5.4
Head-HAZ	0.96	0.43	0.40	315	8.9
Web-HAZ	1.88	0.29	0.27	325	3.1
Web-Weld	2.10	0.20	0.24	347	1.9

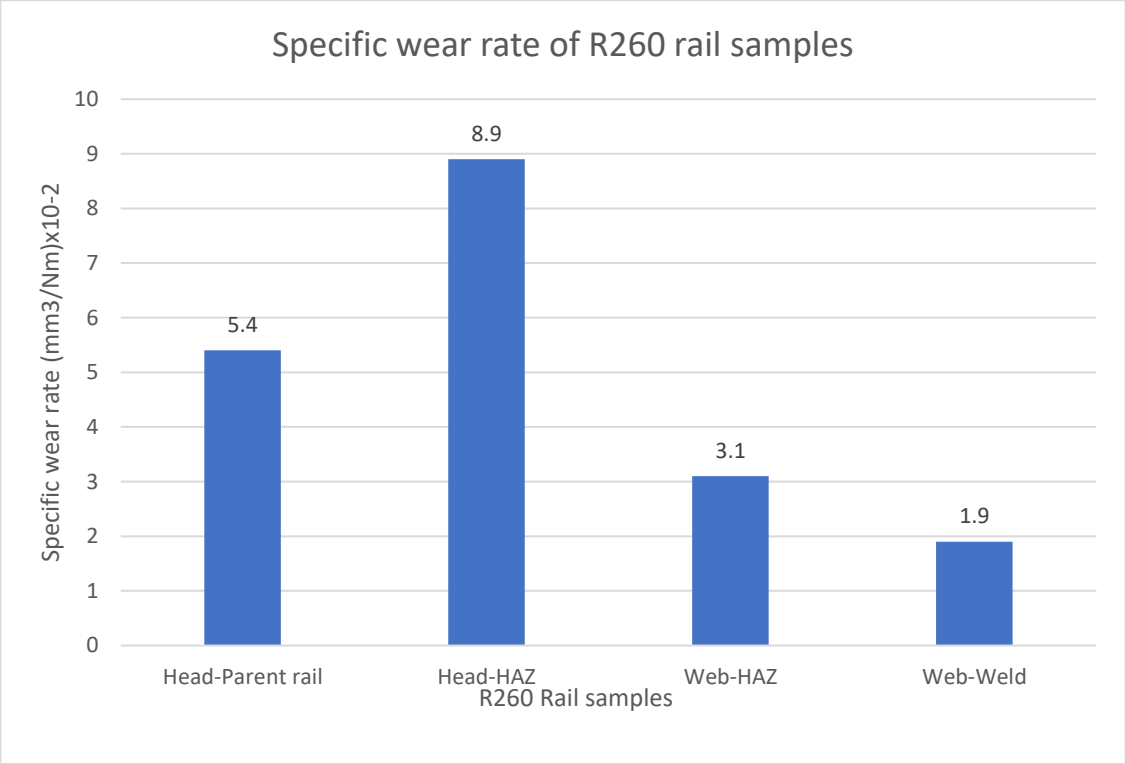


Figure 4-33: Specific wear rate of R260 rail steel samples.

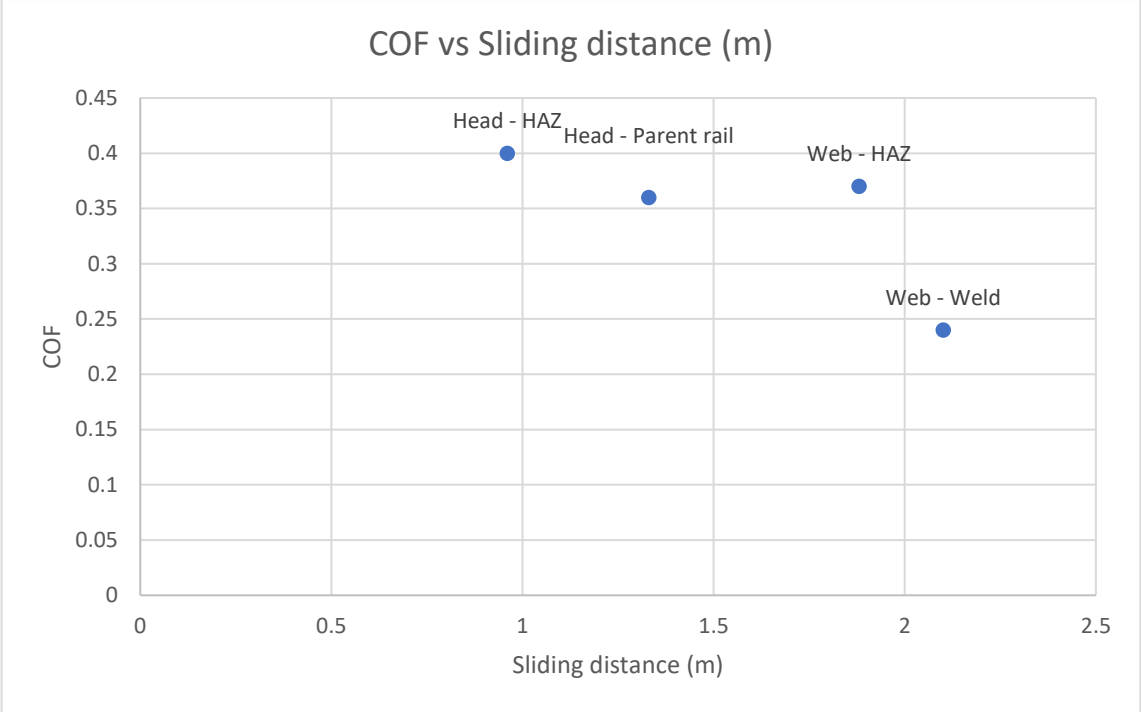


Figure 4-34: COF vs sliding distance plot of the R260 rail samples.

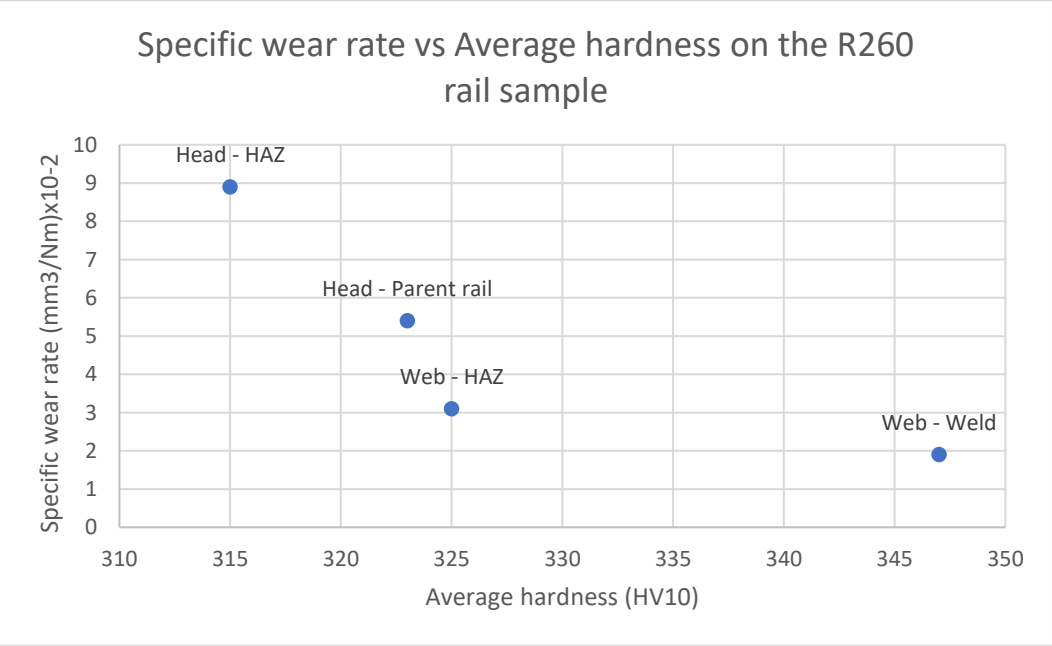


Figure 4-35: Specific wear rate vs average hardness of the R260 rail samples.

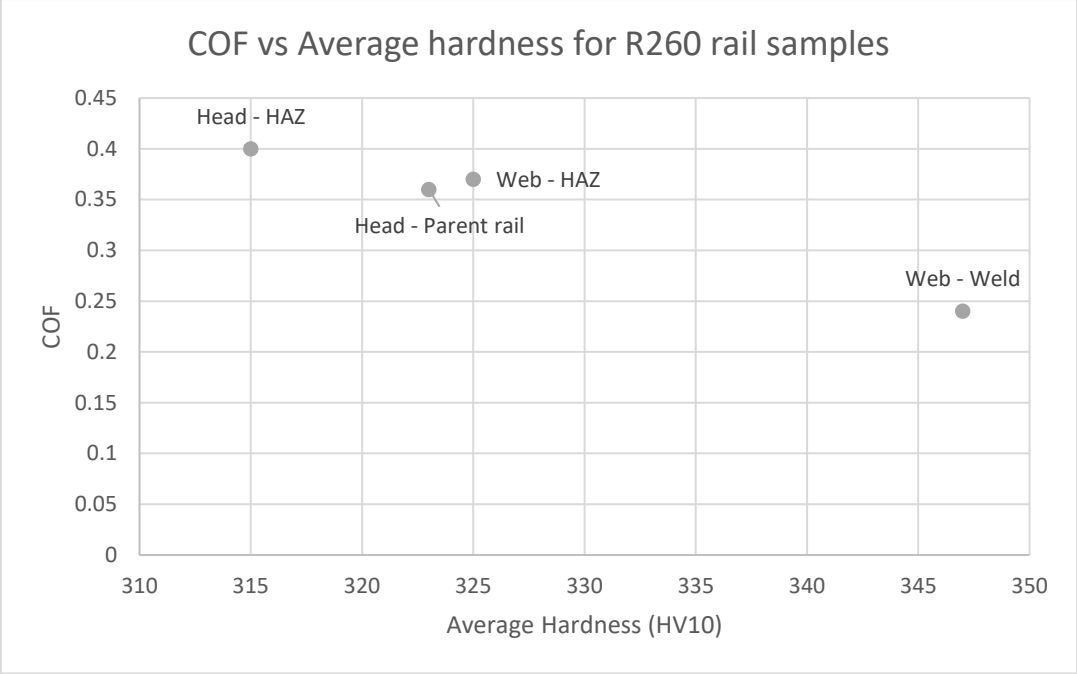


Figure 4-36: COF vs Average hardness (HV_{10}) plot for R260 rail samples.

The results in Figures 4-33 to 4-36 showed the relationship between the specific wear rate of the rail sample. The high average hardness results of the web-weld had a positive impact on the wear volume loss, COF and specific wear rate as they were better than those found on the other tested samples.

The high average hardness on the web-weld interface, fast cooling rate, and finer pearlite grain sizes and narrow pearlitic interlamellar spacing influenced wear rate. The head-HAZ sample exhibited the most inferior wear volume loss, COF, and specific wear rate. This was attributed to the low average hardness results obtained on this sample compared to the other tested samples. Coarse pearlite grain sizes and wide pearlite interlamellar spacing supported the low average hardness results (Gomes et al., 1997).

Based on the average hardness distribution, surface area to volume ratio, cooling rate, pearlitic grain size, and pearlitic interlamellar spacing, the sample with the weld gap of 50 mm showed better wear resistance when compared to the sample with the weld gap of 40 mm. The results from this investigation were in agreement with the results by Gomes et al. (1997) where the findings reported that improving the mechanical properties and microstructure characterisation, improves the wear resistance.

Perez and Beynon (1993) reported that softer ferrite matrix will be significantly deformed, leading to a reduction in the interlamellar spacing close to contact surface. The findings by Daymond and Priesmeyer (2002) on the investigation of elastoplastic deformation of ferritic

steel and cementite studied by neutron diffraction and self consistent modelling, reported that plastic deformation of pearlite was as a result of the soft ferrite lamellae deformation only, at least at low plastic strains. The findings obtained from this research investigation were aligned with studies by Perez and Beynon (1993), and Daymond and Priesmeyer (2002). Sample with high hardness and good wear resistance will not easily failure due to plastic deformation.

The tribological experiment was conducted under dry conditions for this research investigation, and the COF for the head – parent rail, head – HAZ, web – HAZ, and web – weld were 0.36, 0.40, 0.27, and 0.24, respectively. The obtained COF values on all the 4-piece rail samples were below the range 0.5 and 0.7. These results indicate that for all 4 pieces of samples, there was a stable friction until the end of the wear test.

The tribological results obtained in this investigation were aligned with the results obtained by Cakir and Celik (2017) who investigated the effect of isothermal bainitic quenching on rail steel impact strength and wear resistance. Cakir and Celik (2017) investigations reported that COF value fluctuated between 0.5 and 0.7 under dry conditions and varies between 0.05 and 0.3 under lubricated/wet conditions (Ay and Celik, 2014 and Bozkurt and Er, 2020).

The web – weld sample showed the smoothest characteristic with the lowest COF value of 0.24. These results were expected since the sample had the highest average hardness compared to the other samples. The head – HAZ sample had the highest COF value of 0.40, amongst the other samples. This difference was attributed to the lower average hardness values observed on the sample.

The web – weld sample was observed to have a superior sliding wear resistance than the head – parent rail, head – HAZ, and web – HAZ samples. These findings were aligned with findings by Chaves et al. (2009). Chaves et al. (2009) investigated the effect of AISI1080 pearlitic steel microstructureon the wear resistance behaviour using the pin-on-disc sliding wear test.

Chaves et al. (2009) reported that the wear resistance of the sample with pearlitic structures was inversely proportional to interlamellar spacing. The results further showed that fine pearlite had 30% lower mass loss and superior sliding wear resistance than coarse pearlite. Fine pearlitic alloys exhibited better wear performance when compared to bainitic or martensitic alloys.

Figure 4-33 showed that the lowest specific wear of 1.9×10^{-2} under normal load of 5 N was obtained on the web – weld sample piece. This sample piece had the highest average hardness

value and the lowest wear volume loss. The head – HAZ sample piece had the highest specific wear of 8.9 x 10^{-2} under normal load of 5 N; this was expected since the sample had the highest wear volume loss, lowest average hardness, and coarser pearlite grain sizes and interlamellar spacing.

4.2 Chapter Summary

The weld and the parent rail of TW R260-60E1 pearlitic rail steel acceptable in accordance with the NDT acceptance criteria specifications as they had had no relevant recordable defects for both sample with 40 mm and 50 mm weld gaps.

The HAZ width measurement results showed that the samples with a weld gap size of 50 mm had a slightly narrower HAZ width compared to the sample with weld gap size of 40 mm.

Microstructure evaluation characterisation by optical microscope (OM) and the scanning electron microscope (SEM) showed that the welds for both samples were fully pearlitic structures with no intergranular Widmanstätten ferrite, bainite and martensite structures. The XRD analyses showed (110) ferrite and (200) ferrite peaks which were BCC-ferrite phases as a matrix of pearlite structure with a small amount of cementite phases.

Slightly finer pearlitic grain sizes and the interlamellar spacing were measured on the sample with 50 mm weld gap, whereas for sample with 40 mm weld gap had relatively slightly coaser pearlitic grain sizes and the interlamellar spacing. The difference in the pearlitic grain sizes and the interlamellar spacing between the two were influenced by heat input and the cooling rate. Fast cooling rate yielded narrow pearlitic grain sizes and the interlamellar spacing, whereas slow cooling rate yielded wide pearlitic grain sizes and the interlamellar spacing.

Pearlitic grain sizes and interlamellar spacing had an influence on hardness distribution across the weld of each sample. Narrow pearlitic grain sizes and the interlamellar spacing yielded an increasing hardness doistribution profile, when compared to the hardness distribution profile that was yielded by the sample with coarser pearlitic grain sizes and the interlamellar spacing. The sample with 50 mm weld gap had slightly better hardness distribution profile than the sample with 40 mm weld gap.

An good mechanical properties, and wear resistance results were noted for both samples. Although, the sample with 50 mm weld gap showed slightly better mechanical properties and wear resistance results than those found on sample with 40 mm weld gap. Good mechanical properties and wear resistance results on the sample with 50 mm weld gap were influenced by

narrow HAZ width, better microstructure characterisation and hardness distribution profile. These results indicated that as the weld gap on the TW R260-60E1 pearlitic rail steel was increased, the mechanical properties, microstructural characterisation, and wear resistance get improved.

5. CHAPTER 5

5.1 Conclusion and Recommendations

5.1.1 Conclusion

This research study was focusing on assessing the influence on the microstructural characterisation, heat-affected zone (HAZ) dimensions, mechanical properties, and wear resistance behaviour of TW R260-60E1 pearlitic rail steel when the weld gap was set to 40 mm and 50 mm. The findings on this research study showed good and improvement on microstructure characterisation, mechanical properties and wear resistance behaviour for both the 40 mm and 50 mm weld gap samples. Amongst the two sample, the sample with the 50 mm weld gap showed slightly better properties than the sample with 40 mm weld gap. The better properties on the sample with 50 mm weld gap over 40 mm weld gap sample were quantified based on the following drawn conclusions.

- HAZ width distribution profile was observed to be narrow on the sample with a weld gap size of 50 mm and wider on the sample with a weld gap size of 40 mm. The narrow HAZ width profile was contributed by a big surface area to volume ratio on the weld zone. As the weld gap was increased, the surface area to volume ratio got bigger, and faster-cooling rate was achieved. Fast cooling rate yields a HAZ width that is narrow, whereas slow cooling rate yields a HAZ with that is wide.
- Microstructural characterization showed that both samples were dominated by a fully pearlitic structure consisting of ferrite and cementite, with no unwanted phases such as martensitic, bainitic and intergranular Widmanstätten ferritic. The sample with a weld gap of 50 mm had fine pearlite grain sizes and interlamellar spacing when compared to the pearlite grain sizes and interlamellar spacing obtained on the sample with a weld gap of 40 mm. The difference in the pearlite grain size and interlamellar spacing was contributed by the surface area to volume ratio and cooling rate. As the surface area to volume ratio got bigger, the cooling rate became more faster. Fast cooling rate yields fine pearlite grain sizes and interlamellar spacing.
- The mechanical properties (hardness distribution, tensile strength and impact toughness) on both samples were observed to be improving with a decrease in HAZ width, pearlite grain sizes and interlamellar spacing. The sample with a weld gap size of 50 mm had better mechanical properties when compare to the sample with a weld gap of 40 mm. The fine pearlite grain sizes and interlamellar spacing and narrow HAZ

width on the sample with a weld gap of 50 mm were improved by fast cooling rate and a big surface area to volume ratio which were achieved by increasing the weld gap.

- Wear resistance behaviour was obsevered to be improving on the sample with a weld gap size of 50 mm when compared to the sample with a weld gap size of 40 mm. The improvements were contributed by good microstructure characterisation and mechanical properties.

5.1.2 Recommendations for further work

- For both the TW R260-60E1 pearlitic rail steel with a weld gap of 40 mm and 50 mm, residual stresses should be measured using a non-destructive method and a finite element model.
- Investigate the effect of post weld heat treatment on TW R260-60E1 pearlitic rail steel with a weld gap of 40 mm and 50 mm.

6. REFERENCES

ASTM: A370 - 97a, (1997), `Standard test and Definitions for Mechanical Testing of Steel Products`.

ASTM: E23 - 12c, (2016), `Standard Test for Notched Bar Impact Testing of Metallic Materials`.

Ay G. M., and Celik O. N., (2013), `Investigation of Tribological Properties of Rail and Wheel Steel`, Engineering Science and Technology, an International Journal, Vol 16 (2), pp 89-95.

Bramfitt B. L. (2001), `Steels: Near Eutectoid in The Encyclopaedia of Materials`: Science and Technology. Pergamon Press.

Bozkurt F., and Er U. (2020), `Investigation of Tribological Properties of Rail and Wheel Steels`. Metal Science and Heat Treatment. Vol 62, pp 405-414.

British standard EN 150 6507 - 1 (2005), `Metallic Material - Vickers Hardness Test - Test Method`.

British standard EN 13674 - 1 (2017), `Railway Applications - Track - Aluminothermic Welding of Rails Part 1: Approval of Welding Process`.

British standard ISO EN 6507 - 1 (2018), `Metallic Material, Vickers Hardness test - Test Method`.

Brown, R., Byme, M., & Maxwell, G. (1976). `Method Of Laying Railroad Rail.` Material Science and Engineering. pp 115-122

Chaves A. P. G., Centeno D. M. A., Masoumi M., and Goldenstein H. (2020) `Effect of the Microstructure on the Wear Resistance of a Pearlite Steel`. Materials Research. Vol 23 (2), pp 1-8.

Cia, W., Wen, Z., & Jin, X. A. (2007). 'Dynamics Stress Analysis of Rail Joint with Height Difference Defect using Finite Element Method'. *Engineering failure analysis. Vol* 14(8), pp 1488-1499.

Corus Rail Products (2008), `Technical Guide-Innovation in Rail`, http://www.scribd.com/doc/41058353/Final-Technical-Signed-Off.

Farhangi, H., & Mousavizadeh, S. (2007). 'Horizontal Split-Web fracture of Flash Butt welded rails'. *Proceedings of the 8th international fracture conference*, pp 509.

Girsch G., Hyder, R. (2006). ` Advance Pearlitic and Bainitic High Strength Rails Promised To Improve Rolling Contact Fatigue. Material Science Engineering. pp 112-126.

Gladman T., Mclvor I. D., and Pickering F. B. (1972), `Some Aspect of the Structure - Property Relationship in High Carbon Ferrite - Pearlite Steels`. JISI Vol 210, pp 916-930.

Gomes M. D. G. M. D. F., De Almeida L. H., Gomes L. C. F. C., and Le May I. (1997), `Effect of microstructural Parameters on the Mechanical Properties of Eutectoid Rail Steels`, Material Characterization. Vol 39(1), pp 1-14.

Hyzak J. M., and Bernstein I. M. (1976), `The Role of Microstructure on the Strength and Toughness of Fully Pearlitic Steel`. Metallurgy Transaction A. Vol 7, pp 1217-1224.

IIic, N., Jovanovic, M., Todorovic, M., Trtanj, M., & Saponjic, P. (1999). 'Microstructural and Mechanical Characterization of Postweld Heat-Treated Thermite Weld in Rails'. *Materials Characterization. Vol* 43(4), pp 243-250.

International Organisation for Standardization 22825 (2017), `Non-Destructive Testing of Welds - Ultrasonic testing - testing and Nickel Based Alloys`.

Kalousek J., Fegredo D. M., Laufer E. E. (1985b), `The Wear Resistance and Worn Metallograph of Pearlite, Bainite and Tempered Martensite Rail Steel Microstructures of High Hardness`. Wear of K. C. Ludema ed, Amer. Soc of Mechanical Engineers, New York, pp 212-231.

Kerr, J., & Cox, A. (1999). 'Analysis and Tests of Bonded Insulated Rail Joints Subjected to Vertical Wheel Loads'. *International Journal of Mechanical Science.* Vol 41(10), pp 1253-1272.

Lim, N., Park, Y., & Kang, N. (2003). 'Stability of continuous welded track'. *Computers and Structures.* Vol 81(22-23), pp 2219-2236.

Liberty OneSteel, (2017) `Rail Track Material` Steel Rails and Trak-Lok. www.libertyonesteel.com, pp 1-7.

Liveleak (2013), `Rail Thermite Welding Reaction Railroad Siberia`, http://www.liveleak.com/view?=ee0_1379794699.

Lonsdale, C. (1999). 'Thermite Rail Welding: History, Process Developments, Current Practices and Outlook for the 21st Century'. *AREMA, Annual Conferences*. Vol 2, pp 51-68.

Mansouri H. and Monshi A. (2004). `Microstructure and residual stress variations in weld zone of flash-butt welded railroads, Science and Technology of Welding and Joining. Vol 9(3), pp 237 - 245

McQueen H. J. (2009), `Failure at Elevated Temperatures Influence of Dynamic Restoration`, Material Science Forum. Vol 604-605, pp 285-329.

Meade, B. (1999). 'Welding for the Railroad Industry'. *AREMA.Annual Conference. pp* 13-21.

Meric C., Atik E., and Sahin S. (2002), `Mechanical and Metallurgical Properties of Welding Zone in Rail Welding vai Thermite Process`, Science and Technology of Welding & Joining. Vol 7(3), pp 172-176.

Micenko p., Muruganant, Li H., and Xu X. (2013), `Double Dip Hardness Profiles in Rails Weld Heat-affected Zone. ` Literature and Research Review Report. CRC for Rail Innovation.

Mittemeijer E. J. (2010), `Fundamentals of Materials Science`, Max Planck Institute for Metals Research, Institute for Material Science, University of Stuttgart, Germany.

Mohassel, A., Kokabi, A., Davami, P., Ranjbarnodeh, E., & Movahedi, M. (2013). 'Heat transfer modelling in wide gap rail thermite welding'. Engineering, Material Science, Jornal of Advance Materials and Processing. Vol 1(2), pp 29-37.

Myers J., Geiger G. H. and Poirier D.R (1982), `Structure and Properties of Thermite Welds in Rails`, WELDING J. Vol 61(8), pp 258-268.

Nikas D., Meyer K. A., and Ahlstrom J. (2017), `Characterization of Deformed Pearlite Rail Steel`. 8th Riso International Symposium on Materials Science. Materials Science and Engineering. Vol 219, pp 12-35.

O'Brisen, P. (2014). 'The New Economic History Of The Railway'. London: Routledge.

Profillidis V. A. (2006), `Railway Management and Engineering`, Ashgate, 3rd edition.

Rajanna, S., Shivanand, H.K., Akash Deep, B.N. (2009). ` Improvement in Mechanical Behaviour of Expulsion with Heat Treament Thermite Welded Rail Steel.` World Academy of Science, Engineering and Technology. Vol 60, pp 210-216.

Saita, K., Ueda, M., Yamamoto, T., Karimine, K., Iwano, K., & Hiroguchi, H. (2013). Nippon Steel and Sumitomo Metal Technology.China.*Trend in R`ail Welding Technology and our Future Approach. pp 10-18.*

Saarna M., and Laansoo A. (2004), `Rail and Rail Weld Testing`, 4th International DAAAM Conference, Estonia.

Schroeder L. C., and Poirier D. R. (1984), `The Mechanical Properties of Thermite Welds in Premium Alloy Rails`, Materials Science and Engineering. Vol 63, pp 1-21.

Skyttebol, A., Josefson, B., & Ringsberg, J. (2005). 'Fatigue Crack Growth in a Welded Rail Under the Influence of Residual Stresses'. *Engineering Fracture Mechanics.* Vol 72(2), pp 271-285.

Sonon D.E., Pellegrino J. V., Wandrisco J. M. (1978), `A Metallurgical Examination of Control - Cooled, Carbon - Steel Rails with Service Developed Defects`. Rail Steels - Development, Processing, and Rail ASTM Specification. Vol 644, pp 99-117.

South African Railway History (2008) ` A Brief History`. https://web.archve.org/web/20080305183603/http://orangemarmtrading.com/SA_Railway_History.html.

Struers Ensuring Certainty (2015), `Vickers Test Methods`, http://www.struers.co.uk/default.asp?doc_id=916.

Steenbergen, M. (2006). 'Modelling of Wheels and Rail Discountinuities in Dynamic Wheel-Rail Contact Analysis'. *Vehicle System Dynamics.* Vol 72(2), pp 763-787.

SubsTech-substances and Technologies (2012), `Metals-Steels and cast irons- Iron-carbon phase diagram`, http://www.substech.com/dokuwiki/doku.php?id=iron carbon_phase_diagram.

Tawfik, D., Mutton, P., & Chiu, W. (2008). 'Experimental and numerical investigations: Alleviating tensile residual stresses in flash-butt welds by localized rapid post weld heat treatment'. *Journal of Material processing technology.* Vol 2(2-3), pp 279-291.

Transnet Soc Ltd. (2017). `Rail Development Plan: Long Term Planning Framework 2017. South Africa. Transnet Soc Ltd.

Webster P. J., Mills G., Wang X. D., Kang W.P. and Holden T.M. (1997), `Residual Stress in Alumino-Thermic Welded Rail`, the Journal of Strain Analysis for Engineering Design. Vol 32(6), pp 389-400.

Wu, T., & Thompson, D. (2003). 'On The Impact Noise Generation Due to a Wheel Passing Over Rail Joints'. *Journal of Sound and Vibration.* Vol 267(3), pp 485-496.